

INVESTIGATING PROTON PAIRING IN ^{76}SE WITH TWO-PROTON
TRANSFER ONTO ^{74}GE

A Dissertation

Submitted to the Graduate School
of the University of Notre Dame
in Partial Fulfillment of the Requirements
for the Degree of

Doctor of Philosophy

in

Physics

by

Amy Roberts,

James Kolata, Director

Graduate Program in Physics

Notre Dame, Indiana

February 2013

© Copyright by

Amy Roberts

2013

All Rights Reserved

INVESTIGATING PROTON PAIRING IN ^{76}SE WITH TWO-PROTON TRANSFER ONTO ^{74}GE

Abstract

by

Amy Roberts

Currently, significant experimental effort is going toward detecting neutrino-less double beta decay ($0\nu\beta\beta$), which, if observed, would give information about the origin of neutrino mass as well as the absolute mass scale of the neutrino. However, any interpretation of $0\nu\beta\beta$ lifetimes requires knowledge of the nucleus in which it is observed. Currently, the nuclear contribution to the lifetime is poorly constrained. This work is part of a larger effort to obtain experimental transfer-reaction data to help constrain these calculations for the candidate nucleus ^{76}Ge . Single-nucleon transfer experiments have been very successful in determining the occupancies of the valence shells in the parent and daughter nuclei ^{76}Ge and ^{76}Se . Understanding the ground-state pairing of neutrons in ^{76}Ge and protons in ^{76}Se is also crucial, however. Neutron pairing in ^{76}Ge has already been investigated and has been found to be concentrated almost exclusively in the ground state. Studies of other candidate isotopes show that neutron and proton pairing behavior can be dramatically different. This work investigates proton-pairing strength distribution in ^{76}Se with $^{74,76}\text{Ge}(^{3}\text{He},n)^{76,78}\text{Se}$ and finds that there is no evidence that excited 0^{+} states share the pairing strength with the ground state.

CONTENTS

FIGURES	iv
TABLES	vii
ACKNOWLEDGMENTS	viii
CHAPTER 1: NEUTRINO PHYSICS AND ITS DEPENDENCE ON NUCLEAR PHYSICS	1
1.0.1 Neutrino Oscillation	2
1.1 Massive Neutrinos in the SM	7
1.2 $0\nu\beta\beta$ searches	11
CHAPTER 2: TRANSFER REACTIONS AND NUCLEAR MATRIX ELEMENTS	17
2.1 Shell Model of the Nucleus	17
2.2 Calculation of $M^{0\nu}$ and Experimental Constraints	23
2.3 Valence Shells of the Initial and Final Nuclei	24
2.4 Nucleon-nucleon correlations and the impact they have on NME .	25
2.5 Modeling Two-Proton Transfers	27
CHAPTER 3: TWO PROTON TRANSFER AT NOTRE DAME	33
3.1 Beam Production at Notre Dame	33
3.1.1 Beam Focusing and Selection	35
3.1.2 Beam Bunching	36
3.2 The Target Chamber	41
3.3 The Neutron Detector	43
3.3.1 Electronics	46
CHAPTER 4: MUON VETO DEVELOPMENT	54
4.1 Testing with $^{26}\text{Mg}(^3\text{He},\text{n})^{28}\text{Si}$	54
4.2 Light Collection with Wavelength-Shifting Fiber	56

4.3	Paddle Design	58
4.4	Paddle Performance	65
4.4.1	On-Detector Efficiency	70
4.5	Electronics	75
4.6	Beam Tests	76
4.6.1	Rejected Signal	79
CHAPTER 5: DATA ANALYSIS		81
5.1	Detector Efficiency	82
5.2	Experimental Parameters Related to the Cross Section	86
5.3	Data Sets	90
5.4	Cuts	91
5.5	Ground State Cross-Section	101
5.5.1	Pulse-Selected Data	102
5.6	Placing a Limit on Excited 0^+ States	106
5.7	Fitting the 0^+ ground state	109
CHAPTER 6: CONCLUSION		119
6.1	Future Work	120
APPENDIX A: Cross-Section Values		122
BIBLIOGRAPHY		123

FIGURES

1.1	Neutrino mass heierarchies.	6
1.2	Lepton mass via the Higgs interaction.	8
1.3	A depiction of massless, Dirac, and Majorana models of the neutrino.	9
1.4	Feynman diagrams describing $2\nu\beta\beta$ and $0\nu\beta\beta$	10
1.5	The effective Majorana mass as a function of the smallest neutrino mass.	12
1.6	Uncertainty in current calculated values of $M^{0\nu}$	13
2.1	Alpha separation energy as an illustration of shell structure.	18
2.2	Level diagrams for different models of the nuclear Hamiltonian.	20
2.3	The Woods-Saxon nuclear potential.	21
2.4	Occupancies of the neutron and proton valence shells of ^{76}Ge and ^{76}Se	26
2.5	The $^{74}\text{Ge}(^3\text{He},\text{n})\ 0^+$ cross section at zero degrees as a function of beam energy.	30
2.6	Level diagram of ^{78}Se and ^{76}Se	31
3.1	Beam production at Notre Dame.	37
3.2	Beam bunching.	39
3.3	Timing spectra due to pulse-selected and non-pulse-selected beam.	40
3.4	The target chamber and beam monitors.	42
3.5	A schematic of the neutron detector and its supporting structure.	45
3.6	Simplified sketch of the detector electronics.	48
3.7	DAQ event trigger.	49
3.8	Full diagram of the detector electronics.	51
3.9	Detector scalers.	53
4.1	Timing spectrum for $^{26}\text{Mg}(^3\text{He},\text{n})^{28}\text{Si}$	55
4.2	A view of the channel cut into the scintillator for the WLS fiber.	60
4.3	A view of the endcap used to terminate the WLS fiber.	61
4.4	A view of the cable that connects the scintillator to the PMT.	63
4.5	Schematic of the testing arrangement for the veto paddles.	66
4.6	Electronics used for testing of the veto paddles.	67

4.7	Typical muon signals in the veto paddles.	68
4.8	Position sensitivity of the veto paddles.	69
4.9	Dependence of the veto efficiency on the lower-energy cut.	70
4.10	Improvement in background rejection due to initial veto setup. . .	71
4.11	Initial veto setup.	72
4.12	Final veto setup.	73
4.13	Improvement in background rejection due to final veto setup. . .	74
4.14	Diagram of the detector electronics with the veto signals included.	77
4.15	Effect of the veto on the timing spectrum due to $^{26}\text{Mg}({}^3\text{He},\text{n})^{28}\text{Si}$.	78
4.16	Placing a limit on real events rejected by the veto.	80
5.1	Timing spectrum due to $^{74}\text{Ge}({}^3\text{He},\text{n})^{76}\text{Se}$	82
5.2	Total light deposited 28-MeV neutrons.	84
5.3	Matching the detector efficiency with $d(d,n)$	85
5.4	Checking consistency of efficiency calculation with $^{26}\text{Mg}({}^3\text{He},\text{n})^{28}\text{Si}$ by comparing to nearby measured cross sections.	87
5.5	Interpreting RBS data and constraining the target thickness. . . .	89
5.6	Cuts used to determine event validity include timing correlation and a light signal above the noise threshold.	93
5.7	Determining appropriate groups of detectors for vetoing by examining the vetoed energy spectrum.	94
5.8	Position dependence of the geometric mean of the light signal of rejected events.	96
5.9	Characteristic peak in energy spectrum due to muons.	97
5.10	Determining the position-dependent lower-energy cut using the energy spectrum due to muons.	98
5.11	Optimizing the scale of the low-energy position cut for minimum fractional error.	99
5.12	Testing the validity of the scaled low-energy position cut with position spectra from $^{26}\text{Mg}({}^3\text{He},\text{n})^{28}\text{Si}$	100
5.13	Comparison of pulse-selected and non-pulse-selected timing spectra from $^{74}\text{Mg}({}^3\text{He},\text{n})$	102
5.14	The Gamma distribution.	104
5.15	Functional fit to the pulse-selected timing spectrum.	107
5.16	The angular distributions of the ground-state first excited state $^{74}\text{Ge}({}^3\text{He},\text{n})^{76}\text{Se}$ and $^{76}\text{Ge}({}^3\text{He},\text{n})^{78}\text{Se}$	108
5.17	The Q-value dependence of the zero-degree cross section of $^{74}\text{Ge}({}^3\text{He},\text{n})$ and $^{76}\text{Ge}({}^3\text{He},\text{n})$	110
5.18	Limit on excited 0^+ states as a percentage of the ground-state cross section for ^{74}Ge and ^{76}Ge	111
5.19	The angular distributions of $^{74}\text{Ge}({}^3\text{He},\text{n})^{76}\text{Se}$ and $^{76}\text{Ge}({}^3\text{He},\text{n})^{78}\text{Se}$	112

5.20 Sensitivity of angular distributions and zero-degree cross sections to bound-state and neutron optical model parameters.	115
5.21 Sensitivity of trends in zero-degree cross sections to ${}^3\text{He}$ optical model parameters.	116
5.22 Deviation from the best DWBA fit for other $f - p - g$ isotopes. .	117

TABLES

1.1	Neutrino oscillation parameters.	6
1.2	Summary of $0\nu\beta\beta$ experiments.	15
3.1	Properties of the plastic scintillator used as the neutron detector.	44
4.1	Properties of the WLS and clear optical fiber used in construction of the veto paddles.	57
5.1	Composition and thickness of the ^{26}Mg , ^{74}Ge , and ^{76}Ge targets.	90
5.2	Summary of data sets used in the analysis.	91
5.3	Optical and bound-state potentials used in the DWBA analysis.	113

ACKNOWLEDGMENTS

I would like to thank the Notre Dame physics department and my advisor, Dr. James Kolata, for making their time and talents available to me. This is a debt I am grateful to have and **can never repay.** I would also like to thank the Counseling Center, who worked with impressive dedication to keep me well.

CHAPTER 1

NEUTRINO PHYSICS AND ITS DEPENDENCE ON NUCLEAR PHYSICS

The neutrino was first proposed by Pauli to be a chargeless, nearly massless fermion [1]. This particle was a means to preserve energy, momentum, and angular momentum conservation in nuclear beta decay. The hypothesized process was

$$n \rightarrow p + e^- + \bar{\nu}_e, \quad (1.1)$$

where a neutron n decays into a proton p , an electron e^- , and also an electron anti-neutrino $\bar{\nu}_e$, allowing the continuous electron energy spectrum that was observed. The existence of this difficult-to-detect particle was not confirmed until 26 years later, when Reines and Cowan used a nuclear reactor as a source of anti-neutrinos and observed inverse beta decay of proton targets [2]. Since the first detection of electron anti-neutrinos, an impressive amount has been learned about these elusive particles. This chapter will begin by discussing what is currently known about neutrinos, in particular that there are three, unique flavors and that while they are very light, they do have mass. The remainder of the chapter discusses how neutrinos get their mass in the Standard Model (SM) framework and the experiments currently underway to help determine the origin of its small mass.

1.0.1 Neutrino Oscillation

Neutrinos interact very weakly with matter, and while this makes their detection difficult, it also makes them a potentially valuable source of information. Studying the interior of systems that produce neutrinos becomes possible with a neutrino detector, while other forms of radiation would be absorbed by the surrounding matter. Raymond Davis and John Bahcall recognized the neutrino could be used to test the theory that nuclear fusion was the Sun's energy source. The neutrino detector built by Davis consisted of 100,000 gallons of ^{37}Cl [3], which was readily available as dry cleaning fluid. Solar neutrinos interacting with ^{37}Cl initiate inverse beta-decay, leaving the radioactive ^{37}Ar as a detectable signal. Years of careful data taking yielded a count of ~ 7 neutrinos per two weeks [3], only $\frac{1}{3}$ the rate predicted by Bahcall [4]. Further refinements to the experiment and to the calculations confirmed the discrepancy [5].

While the Davis experiment continued to collect data, other experiments were begun to explore other properties of the neutrino. Originally imagined as a single particle, it was found that there are three distinct flavors of neutrinos, each associated with a lepton partner. It is important to note that the inverse beta-decay which transforms nucleus A to A' ,

$$A(Z, N) \rightarrow A'(Z - 1, N + 1) + \bar{l} + v_l, \quad (1.2)$$

where l is an electron, muon, or tau, requires the proton to have enough momentum relative to the target neutron to create the lepton l . While electrons have a mass of only 0.51 MeV, muons are considerably heavier, having a mass of 105.7 MeV. Tau leptons have a mass of 1776.8 MeV, comparable to a light nucleus. Even the highest-energy nuclear reactions in the Sun provide only ~ 11 MeV, so that the Sun

can produce only electron neutrinos. Energetic pion beams at Brookhaven National Laboratory (BNL) were used to make the first direct measurement of muon neutrinos [6]. Later, more than five years after the discovery of the tau lepton [7] in 1975, tau neutrinos were successfully detected at Fermilab [8]. The inclusion of the neutrino into the SM as a participant in weak interactions mediated by the W^\pm and Z^0 bosons suggested that experiments determining the lifetime of the Z^0 boson could determine the number of interacting neutrinos. Since the Z^0 can decay, among other things, to a neutrino-antineutrino pair of any flavor, more flavors of neutrinos should reduce its lifetime while fewer should increase its lifetime. An electron-positron collider experiment at CERN measured the lifetime of the Z^0 and determined the number of neutrino flavors to be 2.92 ± 0.05 [9].

That there are three flavors of neutrinos, each associated with a different-mass lepton, is significant because the Davis experiment was sensitive only to electron neutrinos. Other radiochemical neutrino experiments, also only sensitive to electron neutrinos, confirmed Davis' results [10, 11, 9]. An idea suggested by Pontecorvo, that neutrinos have mass [12], showed a way forward. Neutrinos had been incorporated into the SM as massless, making it impossible for their flavor to vary with time. If neutrinos were massive, neutrinos could change flavor. The hypothesis was that the radiochemical experiments, sensitive only to electron neutrinos, were measuring a deficit because $\frac{2}{3}$ of the electron neutrinos from the Sun had changed flavor and could not be detected. SNO, an experiment designed to be sensitive to all three neutrino flavors, measured the predicted number of solar neutrinos [10], confirming that neutrino flavors change with time and therefore that they must be massive.

That neutrino flavor oscillation implies a massive neutrino is a general prop-

erty of combining states with different energy eigenvalues. This can be seen by imagining some two states, ψ_α and ψ_β , neither of which are energy eigenstates. These states can be written in terms of the energy eigenstates:

$$|\psi_\alpha\rangle = U_{\alpha 1}|\psi_1\rangle + U_{\alpha 2}|\psi_2\rangle \quad (1.3)$$

$$|\psi_\beta\rangle = U_{\beta 1}|\psi_1\rangle + U_{\beta 2}|\psi_2\rangle, \quad (1.4)$$

where $\hat{H}|\psi_1\rangle = E_1|\psi_1\rangle$ and $\hat{H}|\psi_2\rangle = E_2|\psi_2\rangle$. Then for an initial states $|\psi_\alpha\rangle$, the probability of measuring $|\psi_\beta\rangle$ some time t later is

$$\begin{aligned} P(\alpha \rightarrow \beta) &= |\langle \psi_\beta | \hat{T} | \psi_\alpha \rangle|^2 \\ &= |\langle \psi_\beta | e^{i\hat{H}t/\hbar} | \psi_\alpha \rangle|^2 \\ &= U_{\alpha 1} U_{\alpha 2} U_{\beta 1} U_{\beta 2} \times \frac{\cos((E_1 - E_2)t/\hbar)}{2} \end{aligned} \quad (1.5)$$

This calculation, while not exactly analogous to neutrino mixing, illustrates that the modulation of the probability of detecting a different flavor state depends on the energy difference. In the case of the neutrino, the energy eigenstates are also its mass eigenstates, and it can be shown that the neutrino oscillation phase between components ν_i and ν_j is [9, 13]

$$\phi = (m_i^2 - m_j^2) \frac{L}{2E}, \quad (1.6)$$

where m_i and m_j are the masses of ν_i and ν_j , respectively, E is the energy of both, and L is the distance between the neutrino source and the detector. Neutrino oscillation experiments are therefore sensitive to the differences between neutrino masses but not to the absolute mass scale. Other types of experiments constrain

the absolute mass scale to less than ~ 2 eV. Cosmological limits are sensitive to $m_1 + m_2 + m_3$ and constrain this quantity to be less than $0.3 - 1.3$ eV at the 95% confidence level [14]. Experiments designed to measure the endpoint of beta decay are sensitive to the quantity $\sqrt{|U_{e1}|^2 m_1^2 + |U_{e2}|^2 m_2^2 + |U_{e3}|^2 m_3^2}$ currently limit this value to less than 2.05 eV [15].

The neutrino mixing matrix U can be written with three angles,

$$\begin{bmatrix} c_{12}c_{13} & s_{12}c_{13} & s_{13}e^{-i\delta} \\ -s_{12}c_{23} - c_{12}s_{23}s_{13}e^{i\delta} & c_{12}c_{23} - s_{12}s_{23}s_{13}e^{i\delta} & s_{23}c_{13} \\ s_{12}s_{23} - c_{12}c_{23}s_{13}e^{i\delta} & -c_{12}s_{23} - s_{12}c_{23}s_{13}e^{i\delta} & c_{23}c_{13} \end{bmatrix} \times \begin{bmatrix} 1 & 0 & 0 \\ 0 & e^{\frac{i}{2}\alpha_{21}} & 0 \\ 0 & 0 & e^{\frac{i}{2}\alpha_{31}} \end{bmatrix}, \quad (1.7)$$

where $c_{ij} = \cos \theta_{ij}$ and $s_{ij} = \sin \theta_{ij}$, δ is the Dirac CP-violating phase, and the Majorana CP-violating phases α_{ij} are only relevant if the neutrino is a Majorana fermion as discussed in Section 1.1. Several generations of long-baseline neutrino experiments using solar, atmospheric, and reactor neutrinos have impressively constrained the mixing parameters and mass differences. A summary of the parameters is given in Table 1.1. It is significant that the absolute values of the mass differences are measured; the ordering of the mass eigenstates is unknown. Three different “mass heierarchies” are possible: the normal heierarchy (NH) where $m_1 < m_2 < m_3$, the inverted heierarchy (IH) where $m_3 < m_1 < m_2$, and the quasi-degenerate heierarchy (QD) where the mass scale is close to the current limit so that $m_1 \approx m_2 \approx m_3$. A diagram of the three mass heierarchies is shown in Figure 1.1.

Parameter	Best Fit ($\pm 1\sigma$)	3σ
Δm_{12}^2 [10 $^{-5}$ eV 2]	$7.58^{+0.22}_{-0.26}$	6.99 - 8.18
$ \Delta m_{31}^2 $ [10 $^{-3}$ eV 2]	$2.35^{+0.12}_{-0.09}$	2.06 - 2.67
$\sin^2 \theta_{12}$	$0.312^{+0.018}_{-0.015}$	0.265 - 0.364
$\sin^2 \theta_{23}$	$0.42^{+0.08}_{-0.03}$	0.34 - 0.64
$\sin^2 \theta_{13}$	$0.025^{+0.007}_{-0.008}$	0.005 - 0.050

TABLE 1.1: Three-neutrino oscillation parameters, determined by a global fit to relevant neutrino data. The mixing angles $\sin^2 \theta_{12}$ and $\sin^2 \theta_{13}$ were determined using reactor $\bar{\nu}_e$ spectra calculated in Reference [16]. Note that while it is known that $m_1 < m_2$, the sign of Δm_{31}^2 is not known. The table is from Reference [9].

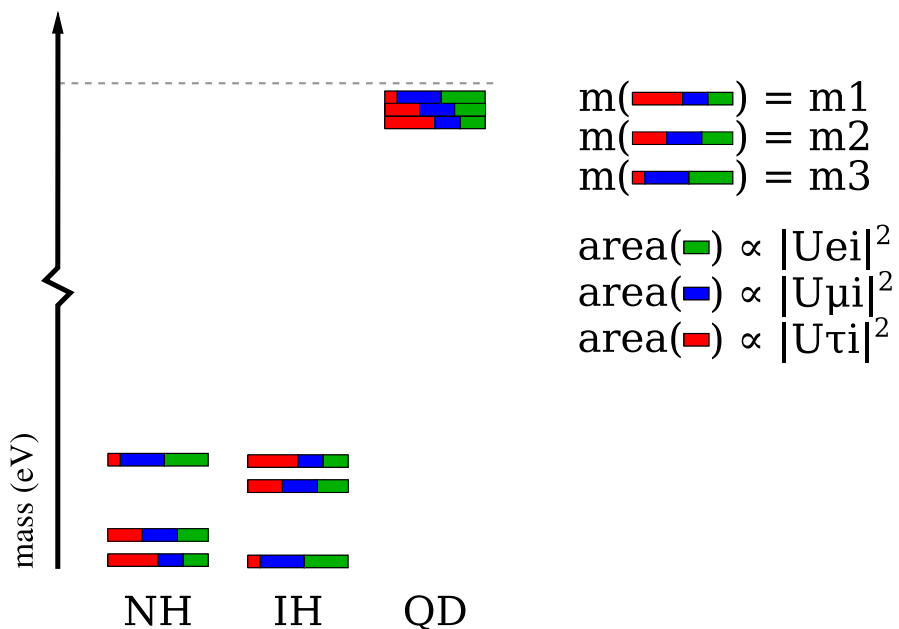


Figure 1.1: The three possible mass hierarchies. The dashed line indicates one-third the current limit for the absolute mass scale, $\sim \frac{2}{3}$ eV.

Long-baseline neutrino experiments have provided a comprehensive picture of neutrino mixing, but they cannot provide access to important information about the neutrino such as the absolute mass scale, CP-violating phases, or the origin of its small mass. These will be discussed in the next section.

1.1 Massive Neutrinos in the SM

In the standard model, fermions are four-component spinors that can be written in a chiral basis so that there is a “left-handed” component of the fermion ψ_L and a “right-handed” component ψ_R . This is a particularly useful basis because the weak bosons W^\pm and Z^0 have been experimentally observed to only interact with the left-handed component of the fermion field. The chiral basis is also helpful in understanding two possible ways to give neutrinos mass in the standard model. Leptons acquire their mass by interacting with the Higgs field; the electron is the lightest because its coupling to the Higgs field is weaker than that of the muon. The tau is strongly coupled to the Higgs field, making it the most massive of the leptons. The diagram in Figure 1.2 gives a heuristic picture of the lepton fields’ interaction with the Higgs background. When neutrinos were thought to be massless, they were introduced into the SM as spinor fields with no right-handed component. The Higgs, which changes the chirality of the particle it interacts with, could not interact with the neutrino because it had no right-handed state to convert to. The ansatz of a solely left-handed neutrino, then, created a massless neutrino in the SM. As experimental evidence has overwhelmingly favored a massive neutrino, it became necessary to modify the theoretical treatment of the neutrino. One approach is to assume that the neutrino, like the SM leptons, is a Dirac fermion and has a left-handed component as well as a right-handed

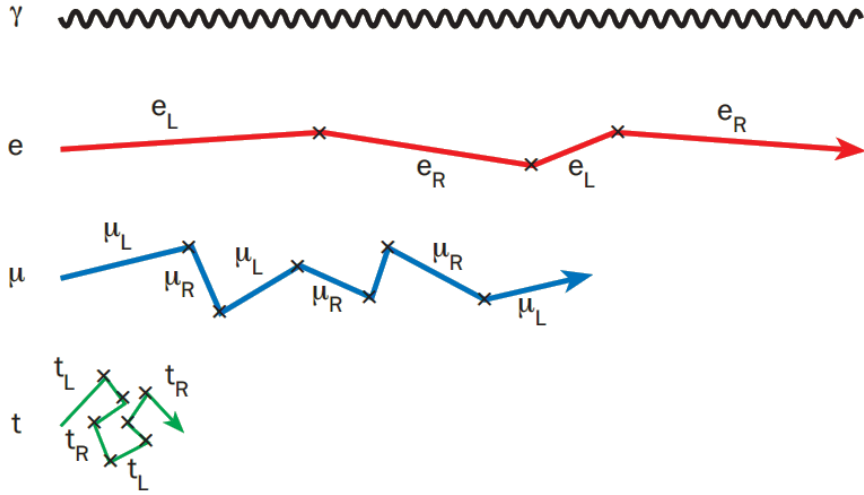


Figure 1.2: Leptons acquire mass by interacting with the Higgs field. Vertices marked with \times indicate an interaction with the background Higgs field. The electron has a smaller coupling to the Higgs field than the tau and therefore interacts less. In a Feynman diagram, lepton lines indicate already-massive leptons. The lines here represent the massless lepton fields and the entire diagram is analogous to a solid lepton line in a typical Feynman diagram. Figure from Reference [17].

component, allowing the Higgs field to interact with the neutrino as it does for the leptons. There is another approach to generate massive neutrinos that is not solely dependent on the Higgs field. If neutrinos are Majorana fermions, that is, unlike Dirac fermions they are their own antiparticles, then the right-handed component of the neutrino field introduces a mass term independent of the Higgs interaction. When left-handed neutrinos interact with the background Higgs field, the heavy right-handed neutrino with mass M can only exist for a short time without violating the Pauli principle. It quickly interacts with the Higgs background, transforming back into a left-handed neutrino. The mass scale of the neutrino is then m/M , where m is the mass due to interaction with the Higgs field. See Figure 1.3 for a picture of these different neutrino theories. The advantage of the Majorana neutrino is that the scale of its interaction with the Higgs field can be comparable to that of other leptons; its small mass can be achieved by assuming

a large M . Majorana neutrinos are also attractive because they could provide an explanation for the observed baryon asymmetry [18].

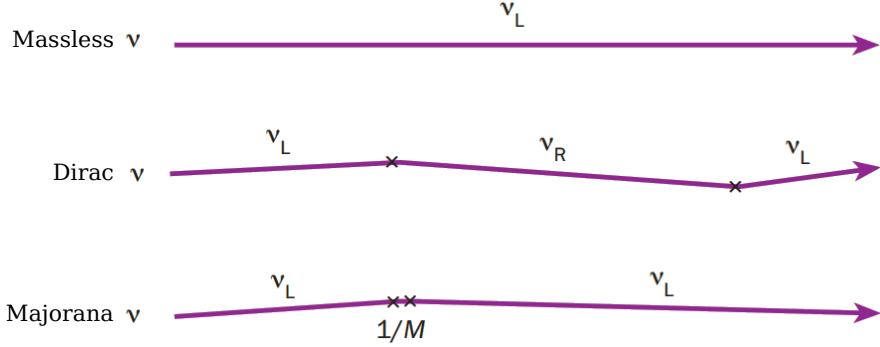


Figure 1.3: A representation of a massless neutrino, a Dirac neutrino, and a Majorana neutrino. Vertices marked with \times indicate an interaction with the background Higgs field. Figure from Reference [17].

Long-baseline experiments have determined that neutrinos are massive and have measured their mass differences and mixing angles to impressive accuracy, but much of their fundamental nature is still not understood. That they could potentially play a significant role in many areas of physics provides significant motivation to build experiments that are sensitive to these neutrino “parameters.” One type of experiment that is sensitive to the Dirac or Majorana nature of the neutrino is a search for a process called neutrino-less double-beta decay ($0\nu\beta\beta$). Two-neutrino double-beta decay ($2\nu\beta\beta$) is a process that has been observed for a number of nuclei and is the simultaneous beta-decay of two protons into two neutrons. If the neutrino is a Majorana fermion, it would be possible for the neutrino to become an internal line as shown in Figure 1.4. This process would be impossible if the neutrino were not its own antiparticle; observation of $0\nu\beta\beta$

would confirm the Majorana nature of the neutrino. It should be noted that

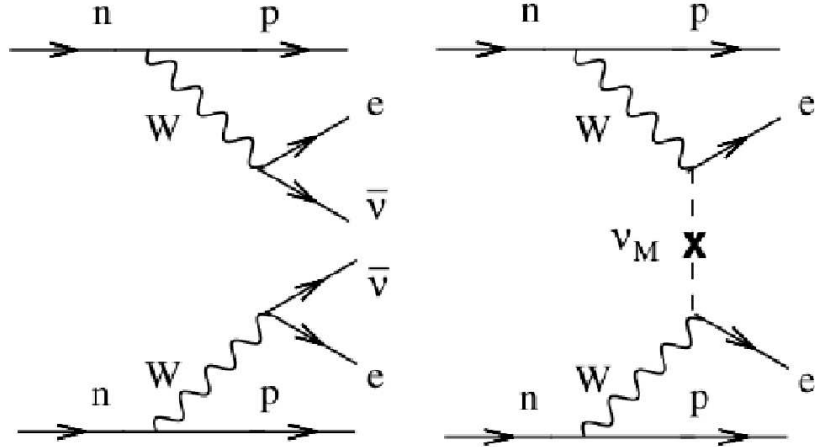


Figure 1.4: Both the observed $2\nu\beta\beta$ (left) and the hypothesized $0\nu\beta\beta$ (right) modes are shown. Nuclear matter is an ideal environment for spatially-close neutrons. Figure from Reference [19].

measured lifetimes for $2\nu\beta\beta$ are extremely long, on the order of 10^{20} yr. The expected lifetime for $0\nu\beta\beta$, if it exists, will be even larger due to the suppression of the right-handed component of the neutrino; the IGEX experiment places the current limit at $> 1.57 \times 10^{25}$ yr [20]. This long lifetime makes $0\nu\beta\beta$ searches an impressive experimental challenge. However, they are currently the only way to explore crucial properties of the neutrino. Aspects of these experiments are discussed in the next section.

1.2 $0\nu\beta\beta$ searches

Searches for $0\nu\beta\beta$ are of interest not only because an observation would conclusively demonstrate that neutrinos are Majorana, but also because an observed rate gives information on the absolute mass scale of the neutrino. The lifetime of $0\nu\beta\beta$, assuming it results from the exchange of light Majorana neutrinos, is

$$(T_{1/2}^{0\nu})^{-1} = G_{0\nu}(Q_{\beta\beta}, Z) |M^{0\nu}|^2 \langle m_{\beta\beta} \rangle^2, \quad (1.8)$$

where $G_{0\nu}(Q_{\beta\beta}, Z)$ is a phase space factor, $|M^{0\nu}| = |\langle f | O | i \rangle|$ is the nuclear matrix element, and $\langle m_{\beta\beta} \rangle \equiv |\sum_i m_i U_{ei}^2|$ is the effective Majorana mass. The phase space factor can be readily calculated [21] and is typically on the order of 10^{-14} yr $^{-1}$. The mass term is the effective mass of the electron neutrino and, unlike long-baseline experiments, is sensitive to the mass scale of the lightest neutrino particle. This dependence is shown in Figure 1.5 for the three possible hierarchy schemes.

The hadronic dependence of the lifetime, $M^{0\nu}$, is sensitive to the initial and final nuclear wavefunctions. Details of these calculations are discussed in Chapter 2, but it should be noted that calculated $M^{0\nu}$ values for most candidate nuclei vary by as much as a factor of 5. This uncertainty in $M^{0\nu}$ directly affects the limits that can be placed on the neutrino mass scale if $0\nu\beta\beta$ is observed. Transfer reactions, discussed in Chapter 2, offer valuable experimental data that can be used to understand which models are most appropriate for these nuclei and improve the accuracy of the calculations. The topic of this thesis is the two-proton transfer reaction, which is also discussed in Chapter 2.

Nuclei that are suitable for $0\nu\beta\beta$ experiments are those that are stable against single beta decay but energetically allowed to double-beta decay. This is the same

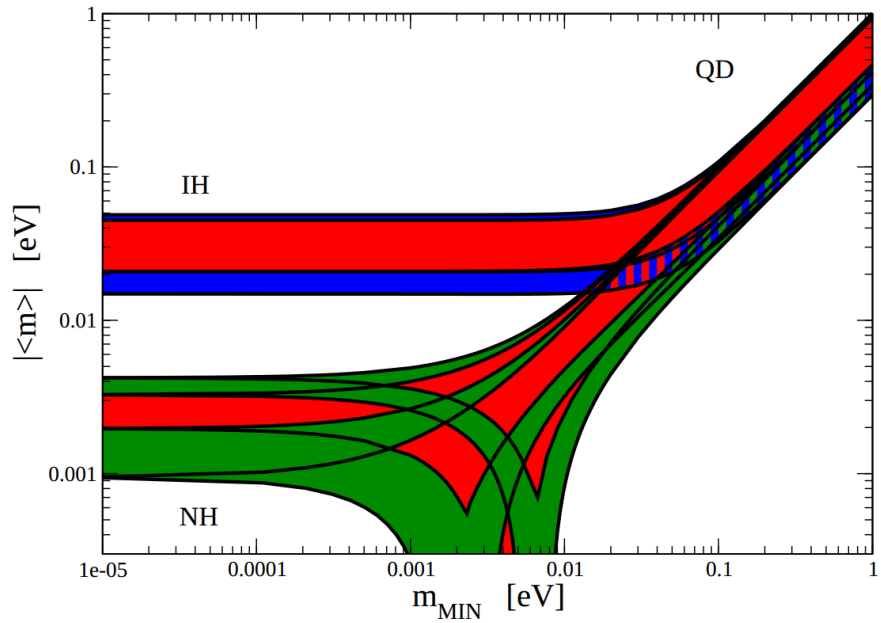


Figure 1.5: The effective Majorana mass as a function of the smallest neutrino mass m_{min} for the inverse hierarchy (IH), normal hierarchy (NH), and quasi-degenerate (QD) scheme. The values are shown in bands indicating the 2σ uncertainty. For all values, it is assumed that $\sin^2 \theta_{13} = 0.0236$ and $\delta = 0$. Colors distinguish between different CP-violating scenarios of the Majorana phases. Red bands require that $\alpha_{31} - \alpha_{21}$ as well as either α_{21} or α_{31} have a CP-violating phases. Blue and green bands require that both α_{21} and α_{31} have CP-conserving phases. Figure from Reference [9].

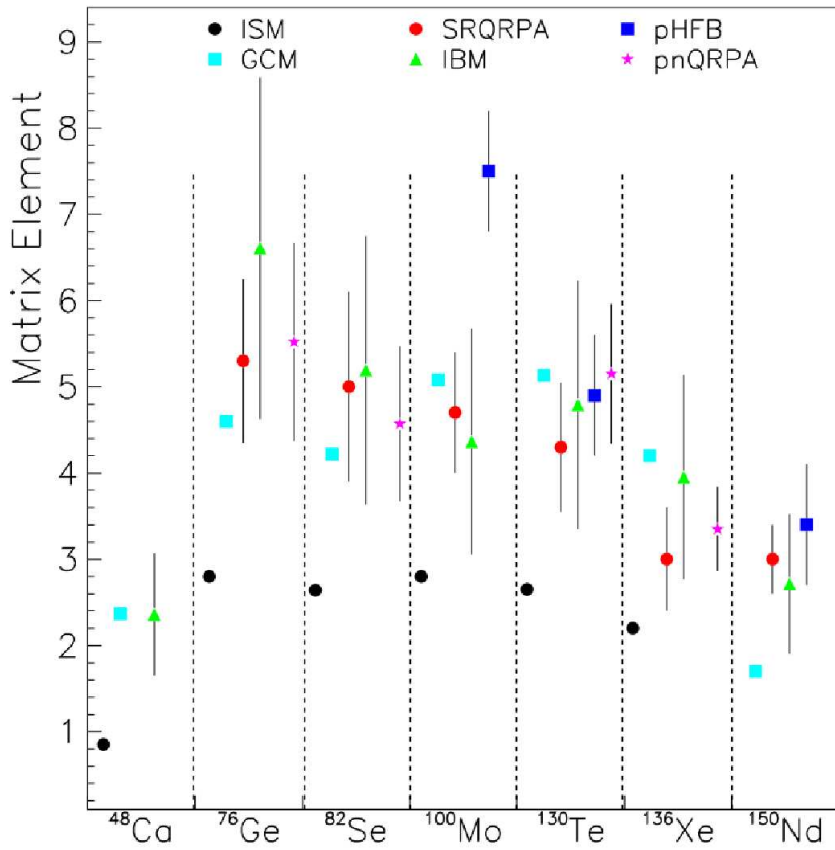


Figure 1.6: Calculated $M^{0\nu}$ for candidate $0\nu\beta\beta$ nuclei. The models used are the Interacting Shell Model (ISM) [22], self-consistent renormalized quasi-particle random phase approximation (SRQRPA) [23], proton-neutron quasi-particle random phase approximation (PNQRPA) [24], generating coordinate method (GCM) [25], the interacting boson model (IBM) [26], and the projected Hartree-Fock-Bogoliubov (pHFB) [27]. Figure taken from [28].

group of nuclei in which $2\nu\beta\beta$ has been observed, and in fact the $2\nu\beta\beta$ process is a significant background to $0\nu\beta\beta$. The nuclei ^{48}Ca , ^{76}Ge , ^{82}Se , ^{100}Mo , ^{130}Te , ^{136}Xe , and ^{150}Nd have been used to search for the process in past and present experiments. See Table 1.2 for a list of past and present experiments. Because of the uncertainties on $M^{0\nu}$ for these nuclei, it is not clear which, if any, would enjoy a shorter $T_{1/2}^{0\nu}$. So many different experiments have arisen because each candidate nucleus offers different advantages in experimental design. ^{76}Ge is an appealing candidate because the active volume also serves as the detector, and Ge crystals are well understood. Experiments using ^{76}Ge are also important because the Heidelberg-Moscow experiment, which claimed an observed $0\nu\beta\beta$ signal [29], used ^{76}Ge crystals. Other nuclei are appealing because they have high abundance or are easy to obtain. This is the case for ^{136}Xe , which is currently being used by the EXO-200 collaboration [30]. Experiments using ^{136}Xe are typically time projection chambers (TPC), which are able to strongly reduce background by reconstructing the momenta of particles in a decay. Using ^{136}Xe is particularly appealing because large quantities are readily available, reducing the cost of increasing the mass scale of the experiment. Another candidate nucleus, ^{130}Te , is frequently used in experiments using bolometry to detect $0\nu\beta\beta$. A summary of $0\nu\beta\beta$ searches is shown in Table 1.2.

Searches for $0\nu\beta\beta$ offer access to unique areas of neutrino physics. Confirmation of the process would demonstrate that neutrinos are Majorana in nature and would also provide a measurement of the absolute mass scale of the electron neutrino. The dependence of the lifetime on $M^{0\nu}$ poses a difficulty because the current uncertainty in calculations limits the sensitivity to the neutrino mass scale and also increases the difficulty of planning experiments that search for the pro-

Experiment	Isotope	Mass [kg]	Method	$T_{1/2}^{2\nu}$ [yr]	$T_{1/2}^{0\nu}$ [yr]	Start - End	Reference
Past Experiments							
Heidelberg-Moscow	^{76}Ge	11	ionization	$(1.74 \pm 0.18) \times 10^{21}$	$1.19_{-0.5}^{+2.99} \times 10^{25}$	1990 - 2003	[29]
Cuorcino	^{130}Te	11	bolometer		$> 2.8 \times 10^{24}$	2003 - 2008	[31]
NEMO-3	^{100}Mo	7	track + calorim.	$(0.716 \pm 0.055) \times 10^{19}$	$> 1.0 \times 10^{24}$	2003 - 2009	[32]
NEMO-3	^{82}Se	1	track + calorim.	$(9.6 \pm 1.1) \times 10^{19}$	$> 3.2 \times 10^{23}$	2003 - 2009	[32]
Current Experiments							
EXO-200	^{136}Xe	175	liquid TPC	$(2.1 \pm 0.2) \times 10^{21}$	$> 1.6 \times 10^{25}$	2011 -	[30]
Kamland-Zen	^{136}Xe	330	liquid scint.	$(2.38 \pm 0.14) \times 10^{21}$	$> 5.7 \times 10^{24}$	2011 -	[33]
GERDA-I/GERDA-II	^{76}Ge	15/35	ionization	$(1.88 \pm 0.1) \times 10^{21}$		2011/2013 -	[34]
CANDLES	^{48}Ca	0.35	scint. crystal			2011 -	[35]
Funded Experiments							
NEXT	^{136}Xe	100	gas TPC			2015 -	[36]
Cuore0/Cuore	^{130}Te	10/200	bolometer			2012/2015 -	[37]
Majorana Demo	^{76}Ge	30	ionization			2013 -	[38]
SuperNEMO Demo	^{82}Se	7	track + calorim.			2014 -	[39]
SNO+	^{150}Nd	44	liquid scint.			2013 -	[40]

TABLE 1.2: Past, present, and future $0\nu\beta\beta$ experiments. Detecting a signal in several different isotopes would greatly improve the likelihood of a Majorana process. From [28].

cess. Nuclear transfer experiments provide information that can help reduce the uncertainty of $M^{0\nu}$ calculations, and this thesis focuses on two-proton transfers in the Ge nuclei. The impact of such a transfer experiment is discussed in Chapter 2.

CHAPTER 2

TRANSFER REACTIONS AND NUCLEAR MATRIX ELEMENTS

The nuclear matrix elements for the $2\nu\beta\beta$ process are well-understood, but calculation of $M^{0\nu}$ for the $0\nu\beta\beta$ process is significantly different [41]. This chapter discusses the calculation of $M^{0\nu}$ for the $0\nu\beta\beta$ process and the constraints that can be placed on these calculations with experimental data, including the two-proton transfer data that is the topic of this thesis. The model of the nucleus as a collection of independent particles underlies all further discussions of $M^{0\nu}$ and interpretation of experimental results and is discussed first.

2.1 Shell Model of the Nucleus

Trends in systematic nuclear data such as nuclear mass, proton and neutron separation energies, and the energy of the first excited state give clear evidence of “magic numbers” of protons and neutrons in nuclei. Figure 2.1 shows the alpha separation energy with increasing neutron number N , which also shows this systematic behavior. Such a structure is suggestive of that seen in atomic electrons, which experience a central potential primarily due to the Coulomb interaction. Such a potential is not an appropriate model for nucleus, where the potential is known to be short range [43]. One model that has promising beginnings is the harmonic oscillator potential. To determine the magic numbers predicted by

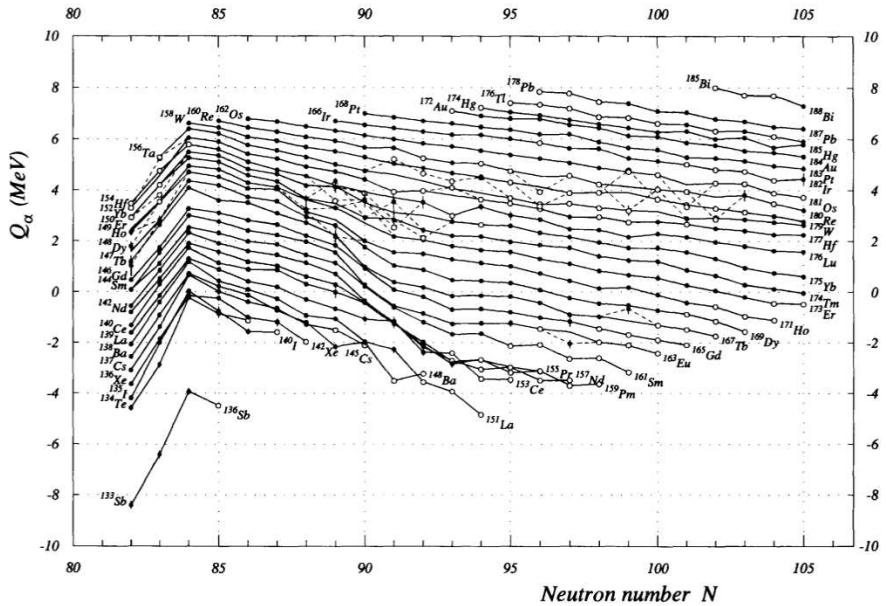


Figure 2.1: Alpha separation energy as a function of neutron number. The behavior around $N = 84$ is indicative of shell structure. From Reference [42].

this potential, consider the quantum numbers that describe an eigenstate of this potential. The principal quantum number, n , indicates the number of nodes of the state. In this work, the node at infinity is included rather than the node at zero, so that n ranges from 1 to inf. The orbital angular momentum is denoted l , with $l = 0, 1, 2, 3, \dots$ typically called the s, p, d, f, \dots orbitals as in atomic electron structure. The eigenvalue associated with the projection of the orbital angular momentum operator along the z -axis is m , which varies between $-l$ and l and is called the magnetic quantum number. The eigenvalues of any eigenstate of a spherically symmetric potential cannot depend on the magnetic quantum number, so that for the harmonic oscillator potential, any state associated with l has a multiplicity of $2(2l+1)$, where the additional factor of two is due to nucleons being spin-1/2 fermions. The eigenvalues of the three-dimensional harmonic oscillator are $E_{nl} = (2n+l-\frac{1}{2})\hbar\omega$, so that the energies proceed in uniform steps as $2n+l$ increases by one unit. Figure 2.2 shows the level spacing for this potential; note that

the energy levels are multiplets. For example, the states $nl = 2s$ and $1d$ both have energy $\frac{3}{2}\hbar\omega$. The harmonic oscillator potential predicts magic numbers at 2, 8, 20, 40, 70, and 112. This matches the observed pattern for low numbers but begins to deviate for heavier nuclei. A reasonable correction to make to the potential is to make it more uniform to more accurately reflect the fact that the density of nuclei is quite uniform [43]. Introducing a potential term proportional to l^2 does this by reducing the potential near the center of the well (where the orbital angular momentum is smaller) and increasing the potential further from the center, where the orbital angular momentum is larger. Adjusting the potential in this way splits the l -degeneracy of the states but does not fundamentally change the predicted magic numbers. It was not until Maria Goeppert-Mayer added a spin-orbit term to the potential [44] that these magic numbers were correctly reproduced.

Although the harmonic oscillator potential is useful in understanding many aspects of nuclear structure with the benefit of having well-understood quantum numbers, it has a number of shortcomings. One has already been discussed - the bottom of the potential should be flatter to better describe the uniformity of nuclear matter. This can be corrected by adding an l^2 term to the harmonic oscillator, but another approach is to define a new potential. The Woods-Saxon potential [45] is a potential that reflects many of the known physical features of the nuclear potential and has the same quantum numbers as the modified harmonic oscillator potential described above. The functional form of the Woods-Saxon potential is

$$V(r) = \frac{V}{1 + e^{(r-r_0)/a}}, \quad (2.1)$$

where r is the distance from the center and the constants V , r_0 , and a represent the depth of the potential, the characteristic radius, and the surface diffusivity.

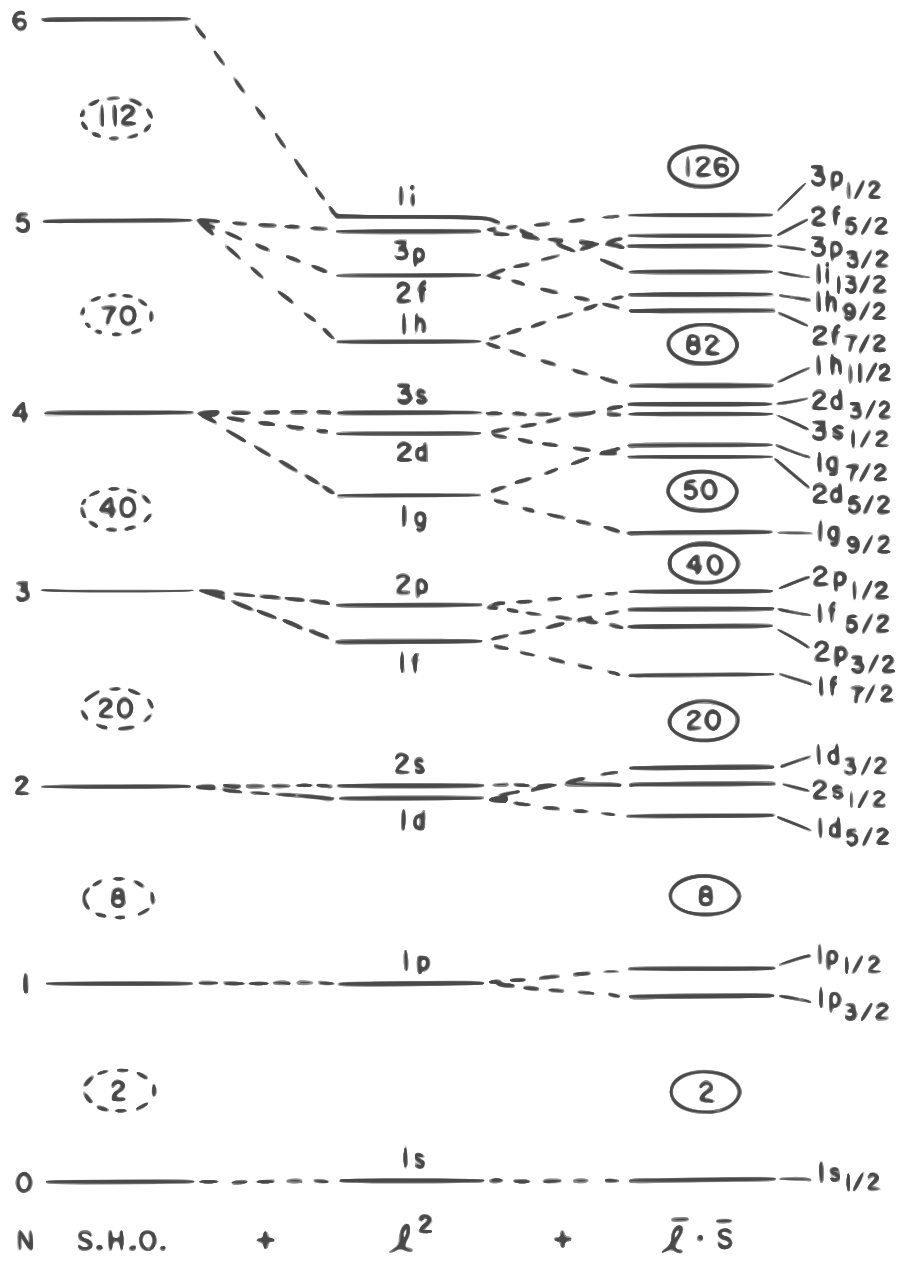


Figure 2.2: Level diagrams for different models of the nuclear potential and their predicted magic numbers. From left to right are the simple harmonic oscillator, a more flat-bottomed potential resulting from adding an l^2 term, and finally the addition of the spin-orbit coupling. From Reference [43].

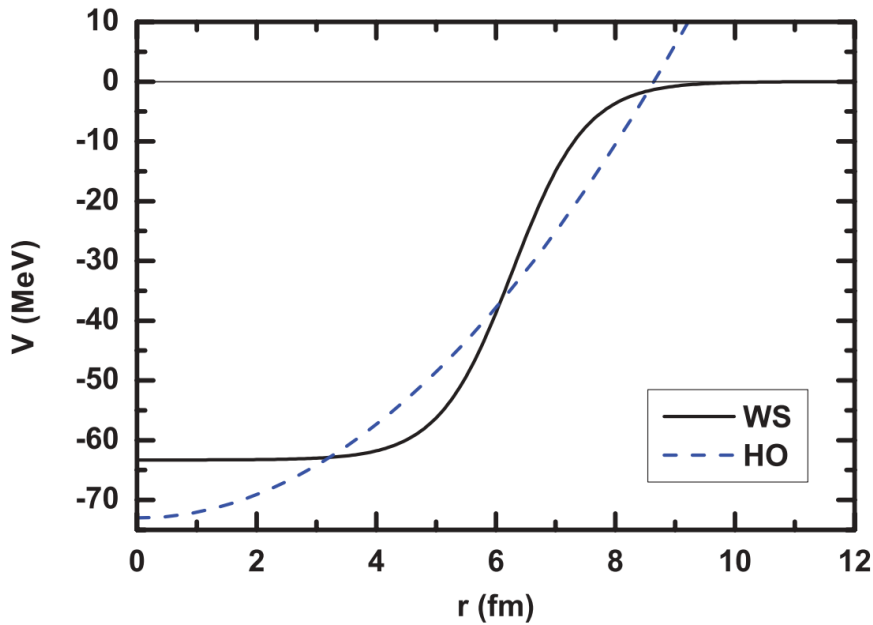


Figure 2.3: A Woods-Saxon potential (solid line) compared to a pure harmonic-oscillator potential (dashed line). Three parameters describe the Woods-Saxon potential: the well depth V , the radius r_0 , and the surface diffusivity a . Note that the Woods-Saxon potential drops to zero while the harmonic-oscillator potential increases without bound. From Reference [46].

All further calculations discussed in this use this potential.

Understanding the nuclear potential is necessary but not sufficient to begin making predictions about nuclear behavior. A nucleus consists of many nucleons, all moving within the nuclear potential and interacting with each other; one must describe this many-particle system. A useful concept in nuclear structure is that of the valence shell of a nucleus. Nucleons in a filled shell form a $J = 0$ core that can be considered largely inert, while the remaining nucleons occupy the valence shell. The picture is even further simplified due to the strong tendency for nucleons to couple into $J = 0$ pairs, so that the ground state of a nucleus can be described simply by describing its unpaired nucleons. The nucleus of primary interest in this work, ^{76}Se , has 34 protons and 42 neutrons. Like all even-even nuclei, its ground state is 0^+ , evidencing the strong coupling of nucleons into $J = 0$ pairs. The pairs studied by $(^3\text{He}, \text{n})$ transfer are proton-pair holes, whose valence shells are predicted to be $2f_{5/2}$. While the phenomenological potentials discussed above reproduce trends in nuclear data with some accuracy, the exact wavefunctions of $^{76,78}\text{Se}$ are not known and it can at best be said that the f , p , and g orbitals are expected to be the primary components of the ground-state wavefunction. Because the $M^{0\nu}$ depends on the overlap between the initial and final nuclei, it is desirable to understand these nuclei, and particularly the differences between their ground states, as accurately as possible. A series of experiments were undertaken to understand these wavefunctions more accurately and will be discussed in Section 2.3.

2.2 Calculation of $M^{0\nu}$ and Experimental Constraints

One approach to calculating $M^{0\nu} = \langle f || O || i \rangle$ is with the shell-model formalism described above. The difficulty with this approach is that the $0\nu\beta\beta$ process is spatially confined to \sim 2-3 fm, which means that intermediate states with excitation energies up to \sim 100 MeV [47] are relevant to the calculation. Even though expressing these states with a shell-model basis set can require a space as large as $O(10^{10})$, several groups have still undertaken this method of calculating $M^{0\nu}$ [48]. Regardless of the method of calculation, the wavefunctions of the initial and final nuclei must impact $M^{0\nu}$. Extensive single-nucleon transfer experiments have been performed to better understand the valence shells and are discussed further in Section 2.3.

A more common approach to the calculation of $M^{0\nu}$ is the Quasi-Particle Random-Phase Approximation (QRPA). The QRPA is a density functional theory that provides a framework particularly suited for describing collective excitations [43]. QRPA assumes that the ground state of the nucleus is in a fully-paired state [49] similar to that in descriptions of superconductivity described by Bardeen, Cooper, and Schreiffer (BCS) [50]. The BCS ground state for even-even nuclei was first suggested by Bohr and Mottelson [51] and is still considered a good approximation for many nuclei [52]. It is known, however, that BCS symmetry is not always a good approximation [53]. In these cases, QRPA calculations can be inaccurate. Two-nucleon transfer experiments can be helpful in determining the distribution of pairing strength in a nucleus [54] and therefore support the QRPA assumption of a BCS-like ground state. See Section 2.4 for more details on the effect of nuclear correlations on the calculation of $M^{0\nu}$.

2.3 Valence Shells of the Initial and Final Nuclei

As discussed in Chapter 1, the half-life of the $0\nu\beta\beta$ process depends on the participating nuclei as well as the neutrino mass scale. While a direct measurement of $M^{0\nu} = \langle f || O || i \rangle$ is difficult because it is only accessible by observation of $0\nu\beta\beta$, it is possible to study the initial and final nuclear states separately in an attempt to improve the accuracy of the calculations.

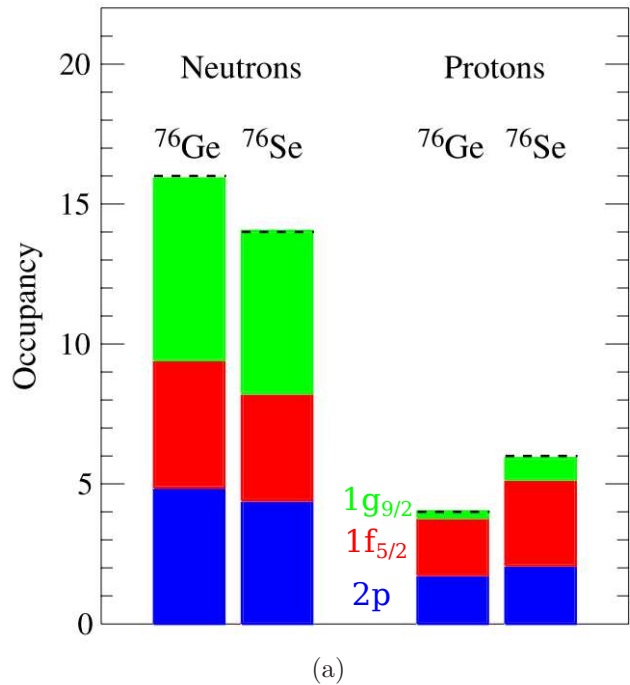
The initial and final nuclear states could inhibit $0\nu\beta\beta$ if there were significant rearrangement in the neutron or proton shell occupancies. Single-nucleon transfer is sensitive to the occupancies and vacancies of valence nucleons and therefore an important tool in determining the extent to which the occupancies change between two nuclei. Very generally, the cross section for transferring a nucleon to a specific shell in a target nucleus will be high if that nucleus has many holes available in that shell but low if that shell is filled. The Macfarlane and French [55] sum rules state that the sum of occupancies and vacancies for an orbital with angular momentum j must be $(2j + 1)$. This allows determination of valence shell occupancies and vacancies from experimental transfer data. The validity of the sum rules was recently checked [56] for Ni isotopes, whose valence orbitals are $f - p - g$ like $^{74,76}\text{Ge}$.

It should be noted that while there is extensive transfer-reaction data, it is not all suitable for determining valence shell occupancies because of uncorrelated systematic errors in the absolute cross-sections of complementary reactions. Comprehensive single-nucleon transfer experiments that are specifically designed to limit these relative systematic errors have been performed on several of the candidate nuclei; see [57] for an overview of current progress. In particular, the nuclei $^{74,76}\text{Ge}$ have been studied with the neutron-adding reactions (d,p) and $(\alpha,^3\text{He})$ as well as

neutron-removing reactions (p,d) and ($^3He,\alpha$) [58]. The valence protons of these same nuclei have been studied with the ($d,^3He$) and (3He,d) reaction [59]. These studies were done on the ^{74}Ge and ^{74}Se nuclei as a consistency check. It was found that the Fermi surface of both the protons and neutrons in $^{74,76}\text{Ge}$ and $^{76,78}\text{Se}$ are quite diffuse, with the relevant neutron and proton orbits being $2p_{3/2}$, $1f_{5/2}$, $2p_{1/2}$, and $1g_{9/2}$. The quantities most important to the $M^{0\nu}$ calculations are the differences in occupancies between the mother and daughter nucleus; these differences are shown in Figure 2.4 along with the theoretical predictions. The single-particle energy levels were adjusted in the QRPA calculation [60] to provide better agreement with the data. These changes reduced the QRPA calculation of $M^{0\nu}$ by approximately a factor of two, bringing it into agreement with the shell-model calculation of $M^{0\nu}$. This reduction in the spread of calculated $M^{0\nu}$ is particularly valuable to reducing the uncertainty of mass limits or estimates from $0\nu\beta\beta$ searches.

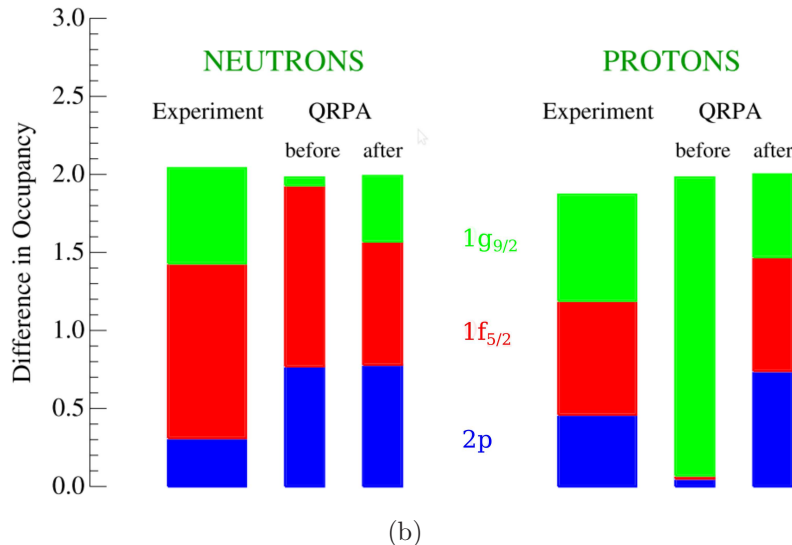
2.4 Nucleon-nucleon correlations and the impact they have on NME

In addition to studying the single-nucleon states in $^{74,76}\text{Ge}$ and $^{76,78}\text{Se}$, understanding correlated neutron pairs in ^{76}Ge and correlated proton pair holes in ^{76}Se is relevant to $M^{0\nu}$. Calculations suggest that significant contributions to $M^{0\nu}$ come from inter-nucleon distances of less than 3 fm [47]. The distribution of highly-spatially-correlated 0^+ strength, therefore, may strongly influence $M^{0\nu}$. QRPA calculations can be particularly sensitive to 0^+ strength that is not exclusively in the ground state as these models assume a BCS approximation where the ground state contains all the 0^+ strength [49]. transferred protons strongly populate pairing vibrationsticularly useful probes of pairing in nuclei as the trans-



(a)

Orbitals Participating in the Decay $^{76}\text{Ge} \rightarrow ^{76}\text{Se}$



(b)

Figure 2.4: (a) Occupancies of the neutron and proton valence shells of ^{76}Ge and ^{76}Se determined by single-nucleon transfer reactions. From [57]. (b) The differences between occupancies in the final and initial states are determined from (a) and are more immediately relevant to $M^{0\nu}$ calculations. The theoretical predictions, before and after adjusting level energies to better match the data, are shown next to the experimental values. Modified from Reference [57].

ferred protons strongly populate pairing vibrations [54]. The cross section of a two-nucleon-transfer reaction on a nucleus that is well described by BCS should show strong population of the 0^+ ground-state with little, if any, population of 0^+ excited states. A system that demonstrates the motivation for studying pairing in ^{76}Se particularly well is ^{130}Te , another candidate nucleus for $0\nu\beta\beta$. The neutron-pair (p,t) transfer reaction was used to show that the cross section for excited 0^+ states is less than 4% of the ground-state yield [61], suggesting that BCS symmetry is a reasonable approximation for the neutrons in $^{128,130}\text{Te}$. The same is not true for the proton states; the ($^3\text{He},n$) reaction populates an excited 0^+ state with a cross section that is $\sim 30\%$ of the ground-state cross section for both ^{128}Te and ^{130}Te [62]. Studies of ^{76}Ge (p,t) and ^{76}Se (p,t) show that the 0^+ strength is distributed overwhelmingly to the ground state, with excited- 0^+ states being populated at less than a few percent [63]. As can be seen in $^{128,130}\text{Te}$, however, 0^+ strength distribution of the neutrons in a nucleus does not necessarily resemble that of the protons. The aim of this work is to study the distribution of the proton-pair strength using the two-proton transfer reaction $^{74,76}\text{Ge}(^3\text{He},n)^{76,78}\text{Se}$. The ^{76}Ge target serve as a check on the results obtained for ^{74}Ge , which are the most relevant for $0\nu\beta\beta$ of ^{76}Ge .

2.5 Modeling Two-Proton Transfers

Measuring differential cross sections can give information about underlying characteristics of nuclei. For example, population of excited 0^+ states in two-nucleon transfer reactions gives information about pairing in a nucleus. However, the calculated cross sections are also influenced by factors not related to nuclear pairing such as kinematics. These contributions are not as relevant to the calcu-

lations of $M^{0\nu}$ as those that are sensitive to the pairing force. The distorted-wave Born approximation (DWBA) is used to calculate cross sections of transfer reactions by assuming that nuclear elastic scattering is the largest contribution to the nuclear reaction and that the transfer operator can be constructed from the bound-state wavefunctions of the initial and final states using first-order perturbation theory. This assumption is particularly accurate for the forward angles which are of interest in this experiment.

In general, four potentials are needed to perform a DWBA calculation in the case of a transfer reaction $(A = C + x) + B \rightarrow C + (D = B + x)$ where x is transferred onto the nucleus B . The potential felt by the incoming nucleus A due to nucleus B and the potential felt by the outgoing nucleus C due to the product nucleus D are both necessary. The optical-model potentials are of the form

$$U(r) = V_C - Vf(x_0) + \left(\frac{\hbar}{m_\pi c}\right)^2 V_{SO}(\sigma \cdot l) \frac{1}{r} \frac{d}{dr} f(x_{SO}) - i[Wf(x_W) - 4W_D \frac{d}{dx_D} f(x_D)], \quad (2.2)$$

where V_C is the coulomb potential and $f(x) = (1 + e^x)^{-1}$ is the Woods-Saxon potential [64]. The variable x is defined as $(r - r_i A^{1/3})/a_i$, where r is the distance from the center of the nucleus, r_i is the reduced radius of a particular interaction, and a_i describes the diffuseness. The constants \hbar , m_π , and c are the Planck constant, the rest mass of the pion, and the speed of light, respectively. Note that the functional form of the spin-orbit term $V_{SO}(\sigma \cdot l)$ is the derivative of the Woods-Saxon potential, making it predominantly a surface effect. The imaginary component of the potential allows for absorption and, like the real part, has a volume term W and, in addition, a surface term W_D . The parameters of the optical-model potentials are determined by fits to elastic scattering data. Parameter sets that

are in common use, such as the Becchetti-Greenlees neutron potential [65], are global fits to large sets of data [64]. Potentials to bind the transfer nucleons to its original nucleus C and final nucleus B are also needed. When calculating proton-pair transfer cross sections, this method can be complicated considerably when treating each proton in the pair separately. This approach is that of Bayman and Kallio [66], which can accurately predict the absolute differential cross section but also introduces additional parameters such as phases between multi-step transitions. The many parameters needed to make this calculation are poorly constrained unless the wavefunction is well-understood beforehand. A simpler method, the cluster model, treats the protons as a single, bound cluster. While this method does not typically reproduce absolute cross sections well, it reproduces the angular distribution of the more-complicated Bayman-Kallio approach, as well as the experimental data. It should be noted that, when using the either model to predict cross sections, their magnitudes are quite sensitive to the parameters in the Woods-Saxon potential, r and a , which describe the radius of the well and the diffuseness of the surface, respectively. However, the trend of the cross section relative to the energy of the incoming ${}^3\text{He}$ or changing neutron number of the target is well-reproduced.

One can use DWBA calculations to understand the kinematic dependence of the expected cross section, as shown in Figure 2.5; this helps determine an appropriate beam energy. It can be seen from this plot that the ideal beam energy for maximizing the ${}^{74,76}\text{Ge}({}^3\text{He},\text{n}){}^{76,78}\text{Se}$ cross section is slightly more than 18 MeV. However, detector resolution decreases with increasing beam energy as discussed in Section 3.3. Because the product nuclei ${}^{76,78}\text{Se}$ have low-lying excited 2^+ states that could be populated with similar cross section to the ground state,

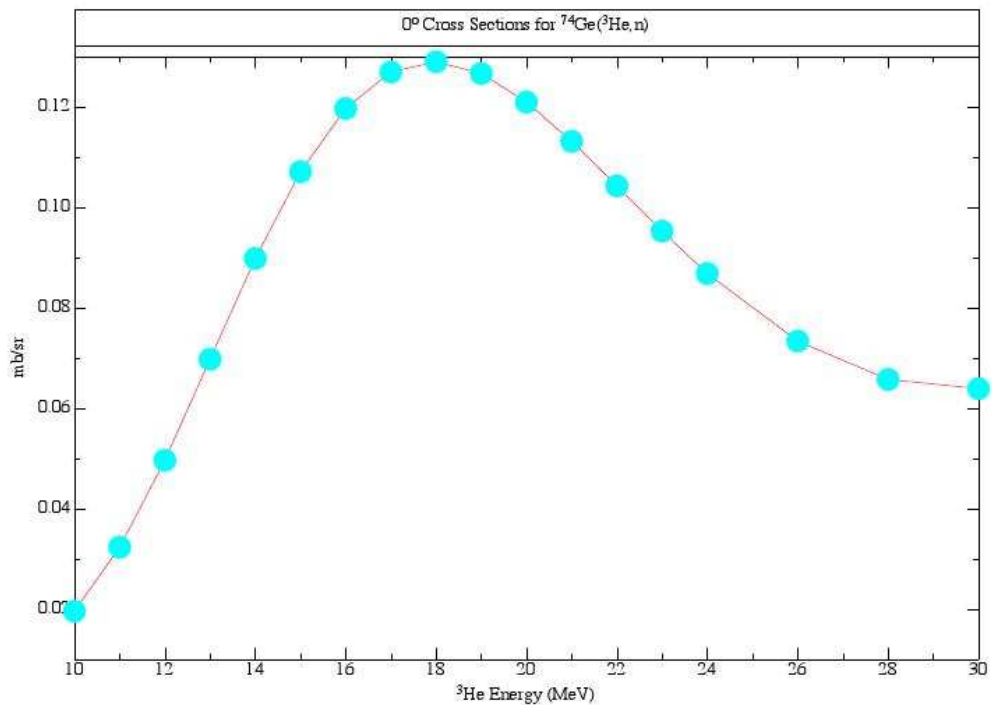


Figure 2.5: A plot showing the $^{74}\text{Ge}(^3\text{He},\text{n})$ 0^+ cross section at zero degrees as a function of beam energy. From [67].

the lower beam energy of 16 MeV was chosen to provide sufficient resolution for resolving these states. See Figure 2.6 for level diagrams of the product nuclei. As can be seen in Figure 2.6, there are known 0^+ states in $^{76,78}\text{Se}$. However,

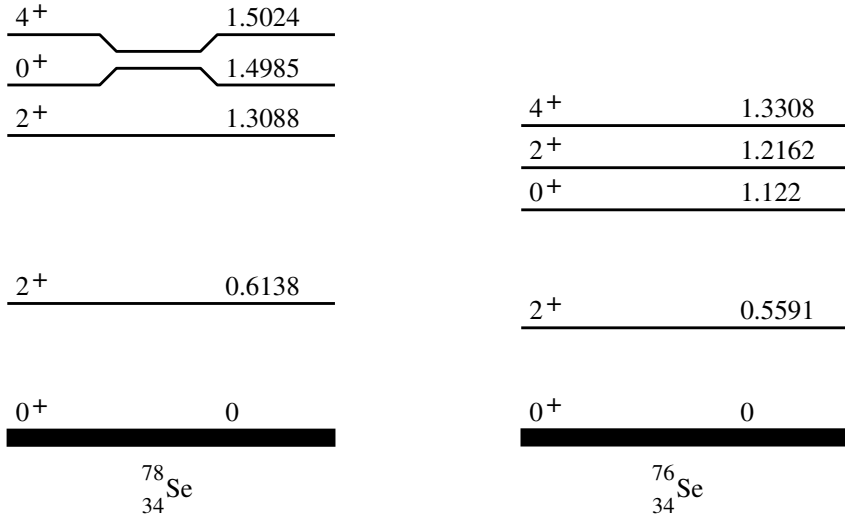


Figure 2.6: The level diagrams of the product nuclei, ^{78}Se and ^{76}Se . Note the low-lying 2^+ state. Notice also that both nuclei have known 0^+ levels. These levels have been measured through γ -ray experiments. Such experiments are not sensitive to the pairing in ground-state nuclei, which is why two-nucleon transfer reactions on $0\nu\beta\beta$ candidate nuclei are of such interest.

these states were discovered through beta decay and excitation due to single-nucleon scattering [68], neither of which gives information on the distribution of the paired 0^+ strength between these excited states and the ground state of $^{74,76}\text{Ge}$. That the leading method of calculating $M^{0\nu}$ relies on the assumption that the 0^+ strength is concentrated entirely in the ground state provides strong motivation to experimentally determine this distribution using two-proton transfer. Particulars

of the beam and neutron detector are discussed in Chapter 3 and an analysis of the results in Chapter 5.

CHAPTER 3

TWO PROTON TRANSFER AT NOTRE DAME

The previous chapter demonstrated the interest in studying $^{74,76}\text{Ge}(^3\text{He},n)^{76,78}\text{Se}$ reactions. The detected reaction product is a neutron and its time of flight (TOF) must be measured. The beam must therefore be bunched and the neutron detector must be optimized to provide excellent timing information. The bunching of the beam and the timing properties of the neutron detector will be discussed in detail in this chapter.

Not only must the beam be bunched, its energy must also be carefully chosen. As discussed in the previous chapter, the purpose of this experiment is to measure the distribution of 0^+ strength. According to DWBA calculations, achieving the maximum 0^+ cross-section for $^{74,76}\text{Ge}(^3\text{He},n)^{76,78}\text{Se}$ requires a beam energy near 18 MeV, but the resolution of the neutron detector decreases with increasing neutron energy. The energy chosen for the ^3He is 16 MeV, and the effect of this energy on the resolution of the neutron detector is discussed in Section 3.3.

3.1 Beam Production at Notre Dame

The beam delivered to the target is 16 MeV bunched ^3He . In this section, we will follow the beam through its production and acceleration.

The Helium Ion Source (HIS) provides negative ^3He ions to the accelerator. A duoplasmatron ion source filled with ^3He gas uses a discharge across high voltage

to convert some of the gas into plasma. Electrostatic elements extract positive ${}^3\text{He}$ ions from the plasma and accelerate them into a canal filled with lithium vapor. Lithium is crucial for creating negatively charged beam because it donates electrons generously, and a small fraction of the ${}^3\text{He}$ becomes negatively ionized after passing through the canal. A dipole magnet after the ion source removes the carbon, oxygen, and other impurities that contaminate the ${}^3\text{He}$ beam. Movable, thick tungsten slits stop these contaminants and allow beam within a small range of magnetic rigidity (see Equation 3.2 below) to pass through to the accelerator. Typically, the maximum output of the HIS is $\sim 1 \mu\text{A}$.

The accelerator at Notre Dame is a tandem Van de Graaff accelerator made by High Voltage Engineering Corporation. Its maximum terminal potential is 10 MV. Negatively charged beam enters and accelerates toward the positive terminal, located in the center of the machine. A thin carbon foil ($\sim 3 \mu\text{g}/\text{cm}^2$) in the center of the machine strips electrons from the beam. The now-positive beam accelerates again, away from the positive terminal. In general, the final energy of a particular beam is then

$$E_{\text{beam}} = E_{\text{HIS}} + (1 + q)eV_{\text{T}}, \quad (3.1)$$

where V_{T} is the terminal voltage, E_{HIS} is the energy of the beam exiting the HIS, q is the charge state of the beam after passing through the carbon foil, and e is the charge on the electron. ${}^3\text{He}$ beam is fully stripped of its electrons by the carbon foil, and so the terminal voltage required to produce 16 MeV ${}^3\text{He}$ is 5.33 MV, well within the operating voltage range of the accelerator.

A dipole magnet with a magnetic field strength B will bend a particle with momentum p and charge qe in a circle of radius R . The product of the field

strength and the radius of the path, BR , is called the magnetic rigidity, and is proportional to the ratio of the momentum and the charge of a particle:

$$BR = \frac{p}{qe} = \frac{\sqrt{2mE}}{qe}. \quad (3.2)$$

A large 90° bend dipole magnet at the exit of the tandem can work in a feed-back circuit to regulate the terminal voltage. Since the mass and charge of the desired beam are fixed, selecting beam at a fixed radius exiting a dipole defines its energy. Horizontal slits at the dipole entrance and exit are approximately one millimeter apart. Both sets of slits serve to narrowly define the beam, but the slits after the analyzing magnet each read the current from incident beam. This slit current is a sensitive measure of the terminal voltage and is used in a feed-back circuit to maintain a constant beam energy. Since the radius of the dipole magnet is one meter, the momentum is defined to one part in 1000 and the energy to two parts in 1000 for a fixed magnetic field. If the terminal voltage drifts up or down, the beam energy will change with it and the beam trajectory will travel a larger or smaller radius through the dipole. For ${}^3\text{He}$, $E_{\text{beam}} \sim 3V_T$, and so a change in the terminal voltage of even one part in 1000 will alter the balance of the slit current. Because this regulation is limited by the stability of the magnetic field of the dipole, the analyzing magnet is calibrated against the nuclear magnetic resonance (NMR) of hydrogen. Using it to regulate the terminal voltage reduces the ripple in the voltage to approximately 10 kV.

3.1.1 Beam Focusing and Selection

Beam exiting the analyzing magnet is narrowly defined by horizontal and vertical slits. Additionally, both pole faces of the analyzing magnet are shaped to

provide a focusing field in both the horizontal and vertical planes. Although the beam has a limited angular divergence at the analyzing magnet, the flight path to the target is ~ 60 m and many focusing and steering elements along the way are necessary to obtain a reasonable transmission rate and ensure that the beam is well-focused at the target. Two Einzel lenses [69] focus the beam before it enters the accelerator, and a set of electrostatic steerers before and after the accelerator are enough to position the beam before it enters the analyzing magnet. Quadrupole doublet magnets focus the beam as it travels through the target rooms, and another set of steerers allows correction of the beam position and angle. The final focusing elements before the target are two large-bore, variable-strength solenoid magnets [70] that focus the beam to a spot approximately 2 mm in diameter.

3.1.2 Beam Bunching

Continuous beam would make it impossible for our detector to determine the neutron TOF. It is possible to bunch the beam so that “bunches” of ${}^3\text{He}$ arrive at the target, each bunch having a time spread of approximately one ns. There are three components to the bunching system at Notre Dame. The first is the buncher itself, which pushes about 40% of the beam into discrete bunches. The remaining 60% is a continuous background and must be removed with the “sweeper”. Together, the buncher and sweeper provide bunches of beam that are 1 ns wide at the target and separated by 101 ns, with no beam in between. With the detector approximately 15 m away from the target, some of the slow neutrons coming from the reaction have a TOF in excess of 300 ns. A pulse-selector is used to eliminate three out of every four bunches to avoid overlapping energetic neutrons from the

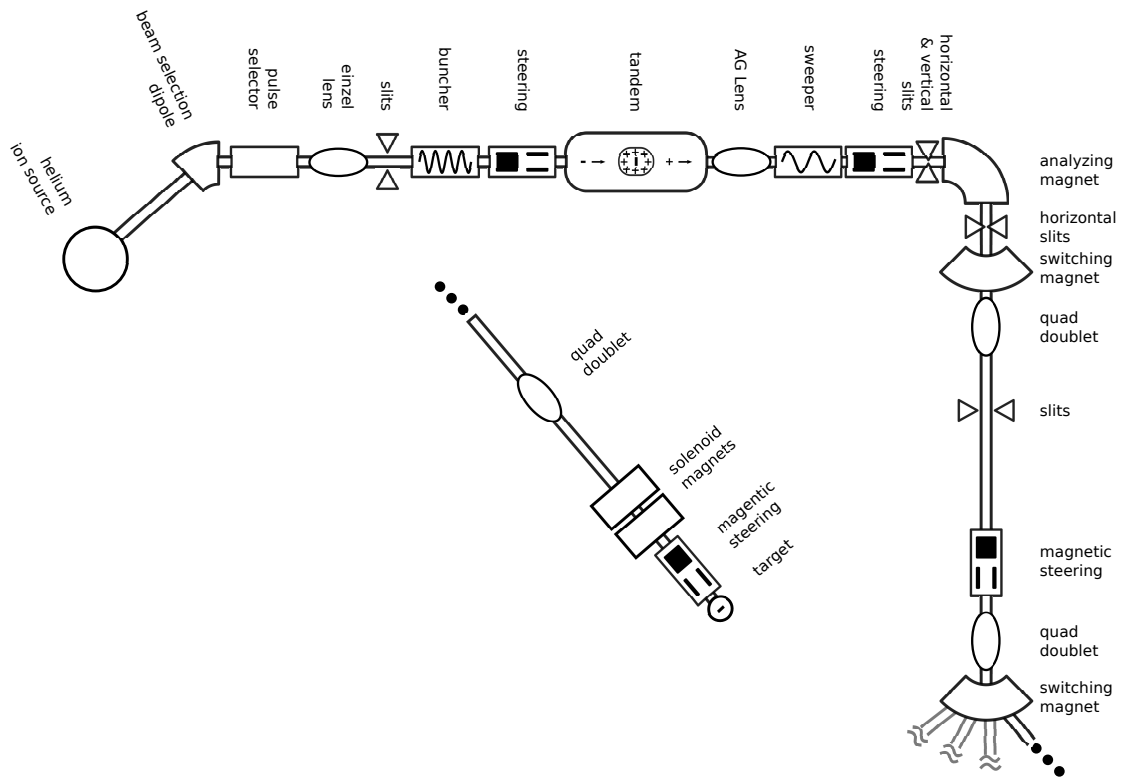


Figure 3.1: Beam production at Notre Dame. The center inset shows the 15° beamline that was used in the experiments.

current beam bunch with slow neutrons from the previous bunch. The buncher, sweeper, and pulse-selector together provide clean bunches of beam separated by 400 ns. The rest of this section describes how each of these components works.

The beam buncher operates by slowing down particles that would arrive too early at the target and speeding up particles that would be arriving too late. To achieve this, two grids perpendicular to the beam connect to a radio-frequency (RF) power supply to create a time-varying electric field. If the electric field were a sawtooth wave in time, the beam bunches would contain all the beam [71]. As illustrated in Figure 3.2, the buncher decelerates the early portion of the beam and accelerates the late portion of the beam. The strength of the field determines the distance at which the bunch will be narrowest, with a stronger field bringing the bunch into time focus earlier than a weaker field. The pure sawtooth field is able to bunch 100% of the incoming beam because it immediately resets after its linear portion. Commercially available RF power supplies, however, generally vary sinusoidally in time. At Notre Dame, a single frequency buncher that operates at 9.85 MHz is used. While the RF signal is increasing approximately linearly with time, beam is bunched exactly as if the field were a pure sawtooth wave. When the electric field approaches a maximum or minimum, little bunching occurs, and when the electric field is decreasing, de-bunching occurs. The sinusoidal RF supply results in nanosecond wide bunches containing \sim 40% of the beam arriving at the target every 101 ns, superimposed on a continuous background of the remaining beam. This continuous beam would render our time signal useless and must somehow be removed.

The “sweeper” provides a sinusoidal electric field that is timed to deflect the continuous beam between the bunches. A set of vertical slits immediately after

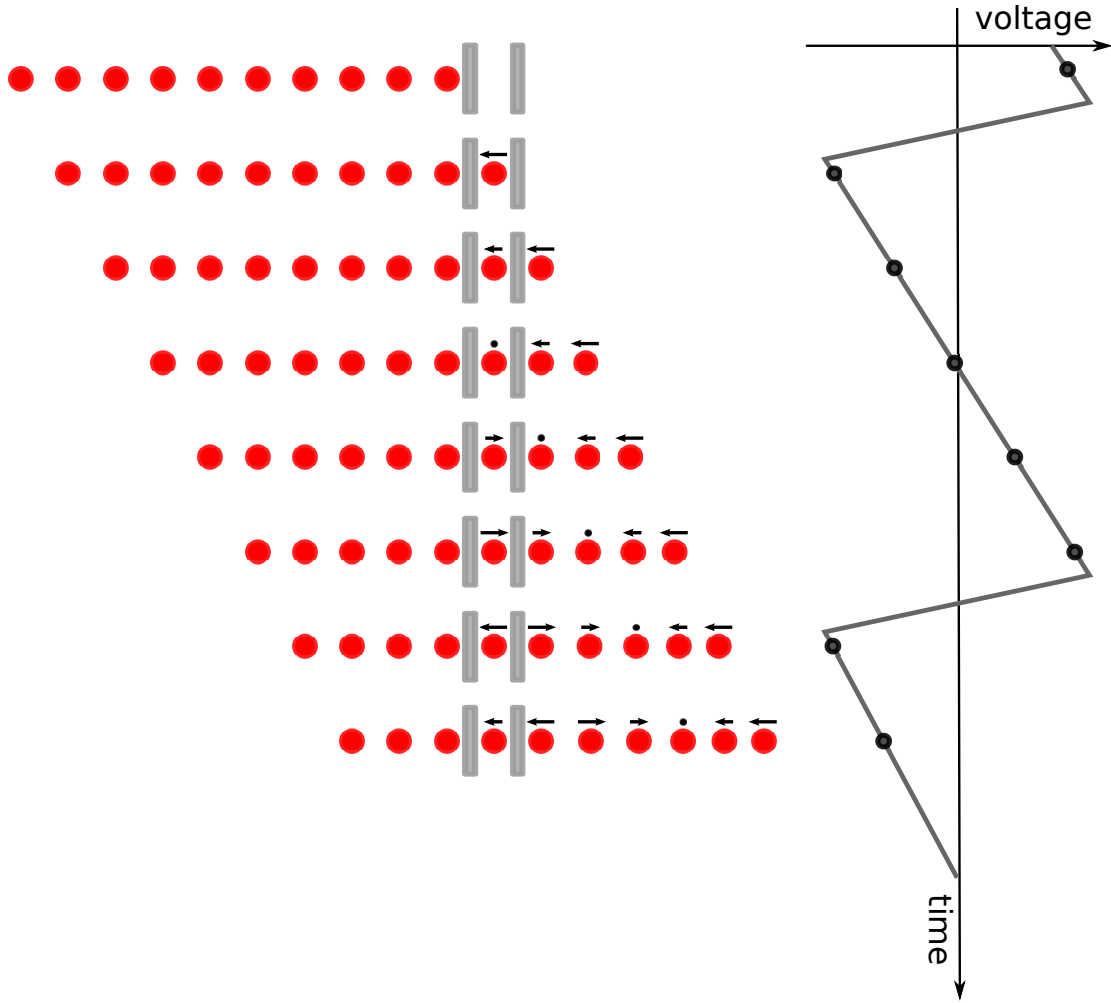


Figure 3.2: Beam bunching using a time-varying electric field. Each dot represents a beam particle, and the vertical gray bars represent the bunching electrodes. To bunch one section of beam, particles arriving first must be slowed down, while particles arriving last must be sped up. A linearly increasing field does exactly this. If the wave is a perfect sawtooth, there is no time during which beam is not being bunched - that is, all the beam is bunched. Notice also that beam does not exit the buncher in a tight bunch; as time passes, beam drifts together. The time until the bunch is at its narrowest depends on the amplitude of the electric field applied by the buncher.

the sweeper removes the deflected beam. Variable delays allow adjustment of the timing between the buncher and the sweeper and must be optimized for a particular beam. Even a few-nanosecond change in the timing can affect which portion of the beam is swept away.

It is possible to take data without pulse selection. However, the spread in TOF of the neutron spectrum is in excess of 300 ns, which complicates the TOF spectrum considerably. With bunches arriving at the target every 101 ns, it will be impossible to tell if a neutron is very fast and associated with the current bunch or very slow and associated with the previous bunch. The resulting spectrum is shown in Figure 3.3.

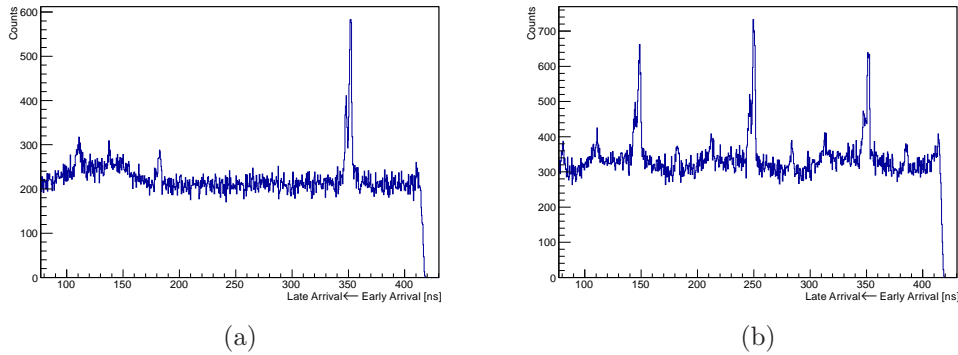


Figure 3.3: The timing spectrum from a pulse-selected beam is shown in (a). The timing spectrum in (b) is from beam with no pulse selection. Both timing spectra are from a ${}^3\text{He}$ beam on a ${}^{76}\text{Ge}$ target. The constant background present in both images is due to random background radiation, not the beam.

To give all the neutrons resulting from one beam bunch time to reach the detector before the next bunch strikes, a “pulse selector” eliminates three of every four

bunches, resulting in 404 ns between each bunch at the cost of beam intensity. The pulse selector is located before the accelerator and consists of two parallel plates, one held at ground and the other at +400 V. A fast switch (SCR) connects the high-voltage plate to ground, letting the selected bunch through without deflection. Vertical slits immediately after the pulse selector remove deflected beam, while undeflected beam passes through to the accelerator. While the beam width is only one ns at the target, at the sweeper the bunch is approximately 80 ns wide, so the SCR must hold the plate at ground for 80 ns to let the entire bunch through.

Beam bunching and pulse selection reduce available beam current - the swept beam current is only $40\% \times \frac{1}{4} = 10\%$ of the non-bunched current. However, without bunched beam it would not be possible to distinguish the neutrons of interest in the $(^3\text{He},n)$ transfer reaction. Increased beam current would improve statistics on $^{74,76}\text{Ge}(^3\text{He},n)^{76,78}\text{Se}$, but the HIS was already operating at its full output for these experiments.

3.2 The Target Chamber

The 16 MeV ^3He beam has been bunched, swept, pulse-selected, and steered and focused onto the target. The bunches that were 80 ns wide before the accelerator have converged into 1-ns wide bunches at the target. The target is at the center of a 2-mm thick stainless steel chamber that has a small gold-lined Faraday cup as shown in Figure 3.4.

To measure the absolute scale of the cross-section, it is necessary to know the number of particles incident on the target. The charge measured by the Faraday cup is directly proportional to this number. Additional detectors sensitive

to the product of the beam current and the target thickness monitor the beam and provide relative normalization. One of these is a Si detector placed inside the target chamber, which monitors ${}^3\text{He}$ beam scattered from the target. The other monitor detector is a BaF_2 detector located just outside the chamber. It is sensitive to γ radiation produced by beam interactions in the target.

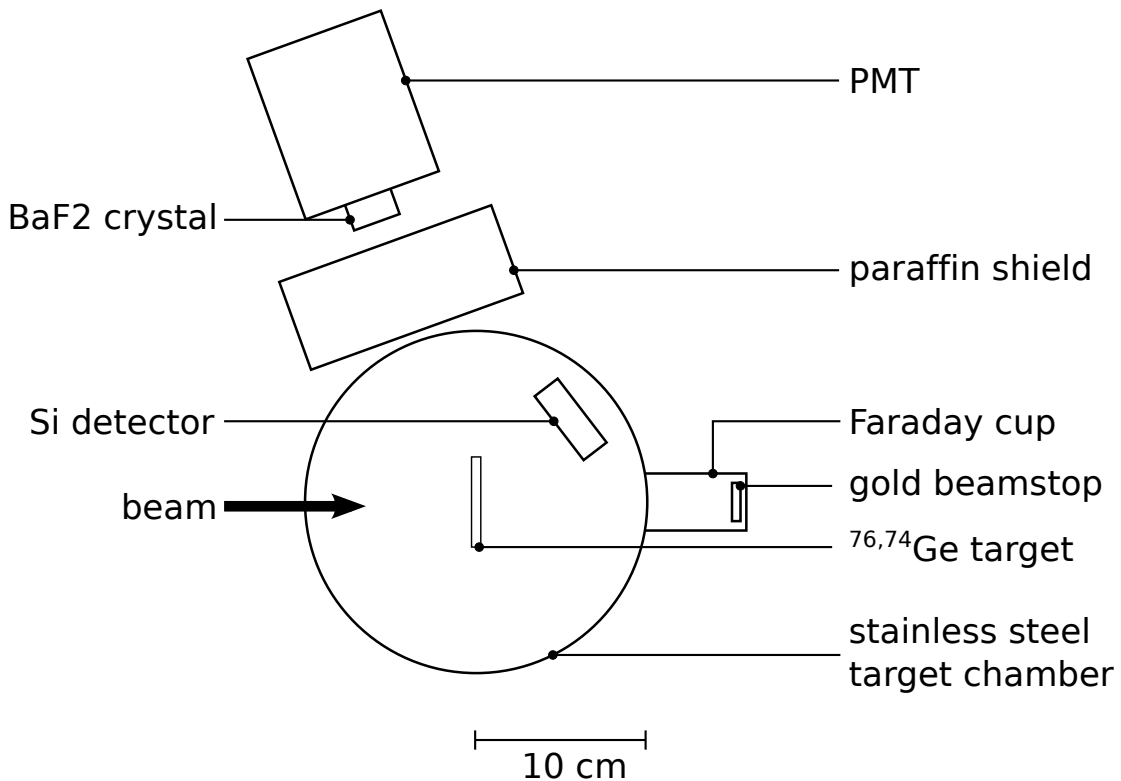


Figure 3.4: The target chamber and beam monitors. The Si detector detects scattered ${}^3\text{He}$ ions while the BaF_2 crystal primarily detects γ radiation from the target. Note that a paraffin block shields the BaF_2 detector from neutron radiation, which also escapes the target chamber.

3.3 The Neutron Detector

The products of two-proton transfer onto $^{74,76}\text{Ge}$ are a neutron and a $^{76,78}\text{Se}$ nucleus. The neutron, lacking charge, is not likely to interact with remaining material in the target and has only a $\sim 5\%$ chance of scattering from the stainless steel target chamber. This low rate of interaction, however, poses a challenge when the goal is to detect the neutron. The neutron detector at Notre Dame maximizes the chance of a neutron interaction by providing protons with which the neutrons can strongly interact. Unlike charged particles, neutrons rarely deposit their full energy in a detector. Neutrons can only deposit all their energy when they collide head-on with a proton. Much more likely is a glancing interaction, where the neutron imparts only some of its energy to the proton. The measured energy spectrum of monoenergetic neutrons ranges from the detector threshold up to the neutron's full energy, making it impossible to determine the energy of the neutron from its deposited energy. Instead, the time of flight (TOF) between the target and the detector is used to distinguish neutrons of differing energies. The neutron detector is optimized to provide precise timing information.

The neutron detector [72] consists of 16 large ($1.5 \text{ m} \times 0.15 \text{ m} \times 0.05 \text{ m}$) bars of commercially available scintillator with excellent timing response [73]. Each plastic scintillator bar is equipped with two fast-risetime photomultiplier tubes (PMT's) at opposite ends. The signal risetimes are approximately 5 ns, and by processing the signal with constant fraction discriminators (CFD's) the timing resolution of the PMT's is sub-nanosecond. Additionally, PMT's on opposite ends of the bars allows construction of an average time signal, removing the timing spread due to the interaction location. Neutron detector signal processing is discussed further in Section 3.3.1.

Properties	BC408
Light Output, % Anthracene	64
Rise Time, ns	0.9
Decay Time, ns	2.1
Pulse Width, FWHM, ns	~ 2.5
Light Attenuation Length, cm	210
Wavelength of Max. Emission, nm	425
No. of H Atoms per cm^3	5.23×10^{22}
No. of C Atoms per cm^3	4.74×10^{22}
Ratio H:C Atoms	1.104
No. of Electrons per cm^3	3.37×10^{22}

TABLE 3.1: Properties of the plastic scintillator used as the neutron detector. Values are taken from [73].

The bars of scintillating plastic are positioned on an arc of radius 14.6 m centered around the target. At this distance, the solid angle subtended by each bar is only $0.15 \text{ m}/15 \text{ m} \times 1.5 \text{ m}/15 \text{ m} = 1 \text{ msr}$. The forwardmost angle relative to the beam is 6° and the largest angle is 22° . As discussed in the previous chapter, the angular distribution of the 0^+ states peaks at 0° and drops to its first minimum at 20° , so that ideally the detector would extend to 0° . A concrete support beam makes 6° the forwardmost instrumentable angle.

The 14.6 m flight path was not arbitrarily chosen; the distance between the target and detector must be as long as possible to ensure reasonable resolution. The longest available path in the room was ~ 15 m. Together with the neutron energy, this distance determines the resolution of the detector. Conservation of energy and momentum determines the relativistic energy $E = \gamma mc^2$ of the outgoing neutron, where $\gamma = (1 - v^2/c^2)^{-1/2}$ and m and v are the rest mass and velocity of the neutron, respectively. The time t it takes for this neutron to travel the distance d between the target and the detector is fixed for a given d and v . Deriving this time as a function of the relativistic energy is simple using the relation

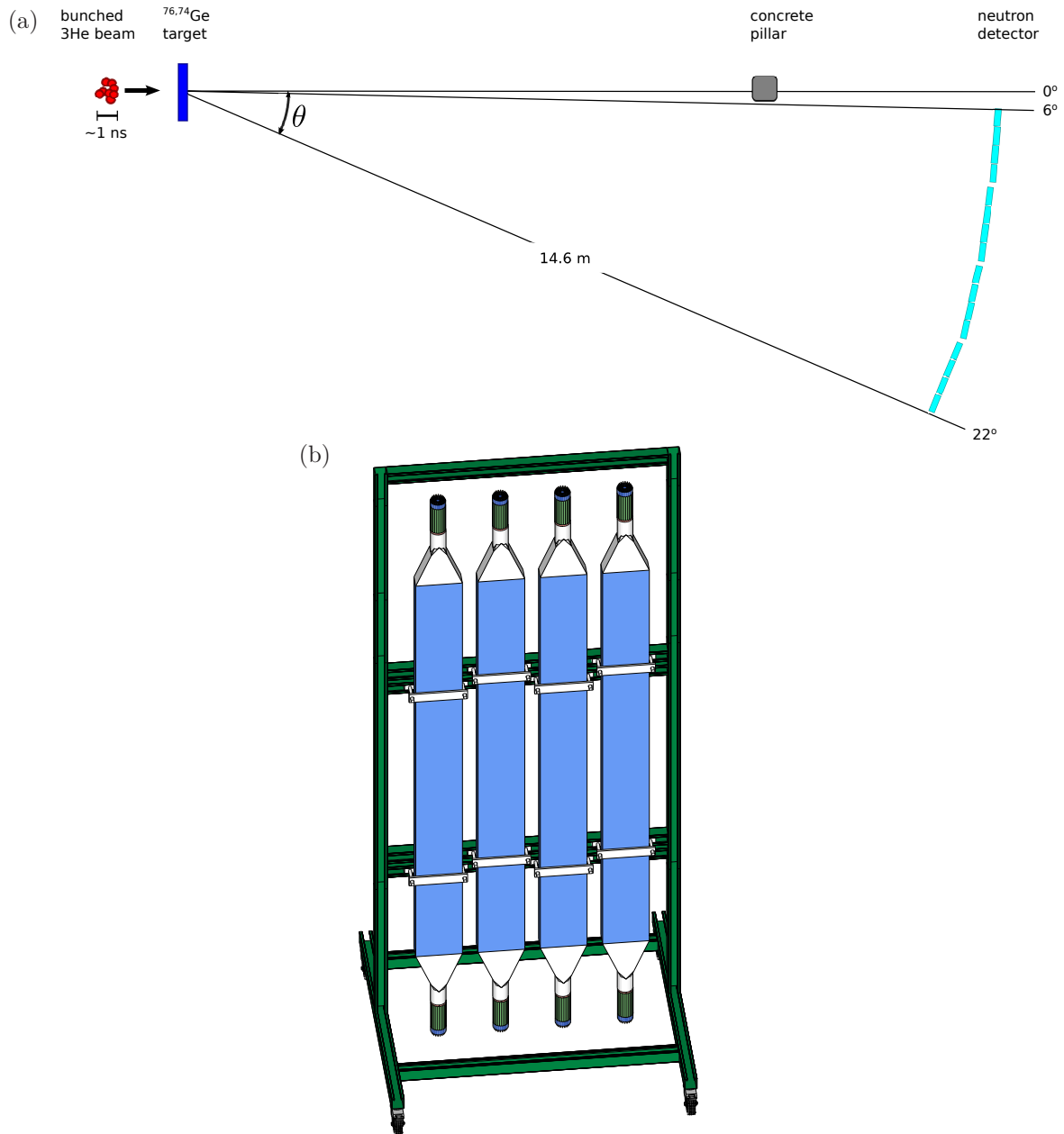


Figure 3.5: A schematic of the neutron detector is shown in (a). The figure is not to scale. The detector is comprised of 16 independent scintillating bars, grouped in fours on separate support structures. One of the supports is shown in (b). Each individual bar of scintillator has a PMT fastened to its top and bottom surface.

$E = \gamma mc^2$, where c is the speed of light:

$$t(E) = \frac{d}{v} = dc \times \sqrt{\frac{(E/mc^2)^2}{(E/mc^2)^2 - 1}} \quad (3.3)$$

Neutrons from $^{76}\text{Ge}(^{3}\text{He},\text{n})^{78}\text{Se}$ have a relativistic energy of ~ 966 MeV if the product nucleus, ^{78}Se , is populated in its ground state. Using Equation 3.3, this gives a TOF of

$$\begin{aligned} t(966 \text{ MeV}) &= (14.6 \text{ m})(0.3 \text{ m/ns}) \times \sqrt{\frac{(966/940)^2 - 1}{(966/940)^2}} \\ &= (14.6 \text{ m})(0.3 \text{ m/ns}) \times \frac{1}{0.23} = 212 \text{ ns}. \end{aligned}$$

Neutrons from a reaction that populates the first excited state of ^{78}Se , which is only 0.6 MeV above the ground state, trail the ground-state neutrons by 1.9 ns. Since the beam bunch itself has a width of 1 ns, this flight path provides not quite enough resolution to separate the ground and first excited state of $^{74,76}\text{Ge}$. However, the differing angular distributions of the two states allowed for a determination of their respective intensities. This is discussed in Chapter 5.

3.3.1 Electronics

In principle, the timing information is all the data acquisition (DAQ) needs to record if there were no background radiation. However, concrete in the room emits low-energy γ radiation that leaves signals in the detector at a high rate. Measuring the energy deposition is necessary because it allows us to eliminate this low-energy background radiation as well as high-energy cosmic rays.

When a particle deposits energy in some bar of the neutron detector, the DAQ must record both the total energy and timing of the signals from the top and

bottom PMT's. A charge to digital converter (QDC) can integrate the PMT signal and a time to digital converter (TDC) can measure the time between a logic pulse created by the PMT signal and the logic pulse from the beam buncher. Because time resolution is the only way to distinguish groups of neutrons with different energies, constant fraction discriminators (CFD's) and not leading edge discriminators create the logic pulse sent to the TDC. The 5-ns PMT signal rise-time, together with CFD's, give timing information with jitter that is about 1 ns. There are no stringent requirements on energy resolution as the detector itself has energy resolution on the order of 1 MeV near the thorium edge.

The lone signal provided by the PMT base is not adequate for pulse processing because the QDC and TDC require separate signals. The signal from the PMT base is also too small to trigger the CFD's. A $10\times$ amplifier makes the signal large enough to trigger the CFD's and provides two copies of the input signal, one which can be analyzed for timing information while the other is analyzed for energy information. A simplified diagram of the data acquisition is shown in Figure 3.6.

The fundamental components of the DAQ are the TDC, the QDC, and the event trigger that causes the DAQ to read each module. Triggering any time either a bar's top or bottom PMT fired would waste the DAQ with recording many noise events. A real event should create signals in both the top and bottom PMT's, and requiring a coincidence between the two results is a reasonable trigger. One way to define an event trigger for the entire neutron wall would be to trigger any time a coincidence between associated top and bottom PMT's occurs. But constructing this trigger with NIM logic units requires many separate logic gates and is unnecessarily complicated.

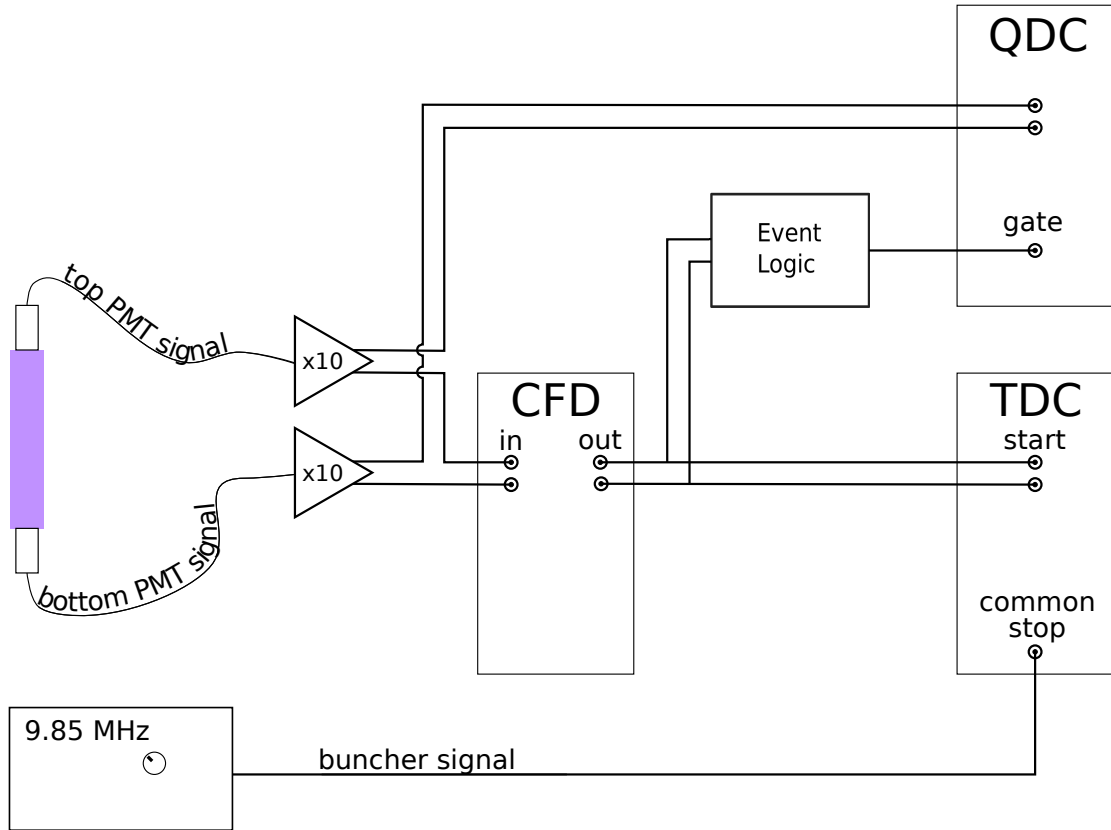


Figure 3.6: A simplified diagram of the neutron detector electronics showing the acquisition of timing and energy information from a single bar of the detector.

One solution is to use the built-in OR of the CFD. Each CFD is an eight-fold unit that provides an OR output. Instead of requiring a top and bottom signal in the same bar, each CFD unit processes a section of only top or only bottom bar signals and the condition is loosened to requiring a signal in a top PMT and a bottom PMT in the same eight-bar group as shown in 3.7. The presence of some top signal AND some bottom signal triggers the event signal. Such an event only requires that both a top and a bottom signal coincided but does not require that these signals belonged to the same bar. This simplified event trigger includes all events of interest, where the top and bottom signal belong to one bar, but also includes spurious events where no bar has a signal in both its top and bottom PMT. With a dead time of less than 30%, this event condition does not hinder data collection. Simple software cuts eliminate any spurious events where no bar has a signal in both its top and bottom PMT.

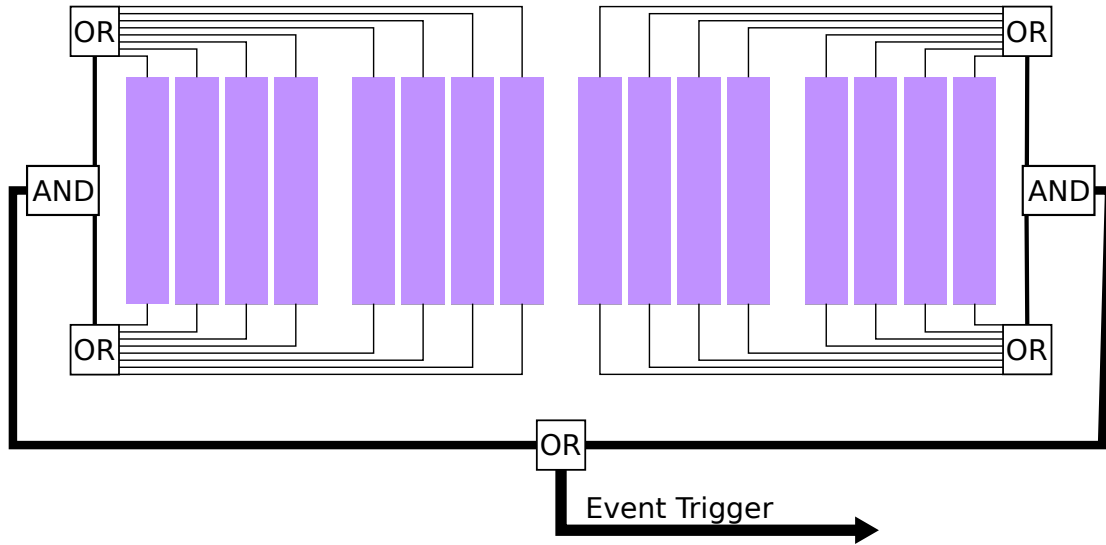


Figure 3.7: The event trigger for the DAQ requires a coincidence between a top PMT and a bottom PMT from the same group of eight bars.

The time information, energy information, and a signal to indicate that this information should be read from the modules and recorded, form the core of the neutron detector DAQ. However, the DAQ must also record information from the detectors near the target. The particles of interest for the Si detector are scattered ^3He beam, and because they are charged and deposit all their energy in the Si detector, the energy is a useful way to identify scattered ^3He and should be recorded. The BaF_2 detector sits outside the target chamber and monitors primarily beam-induced γ radiation. The timing of this detector's signal relative to the beam buncher, rather than the energy, is recorded by the DAQ. Finally, because these detectors have high detection efficiency and are placed close to the target, their event rate is much higher than that of the neutron detectors. While these detectors are essential to determining the relative particle flux through the target, the dead time they cause the DAQ should not prohibit events from the neutron detector itself from being recorded. Pre-scaling the signals from the Si and BaF_2 by factors of 100 and 50, respectively, before adding it to the event trigger limits the dead time of the total system to less than 20%.

The DAQ must also record some quantities that are independent of the event trigger, such as the charge on the Faraday cup, which is needed to normalize the number of particles incident on the target between runs. The DAQ records these as scalers. Figure 3.9 shows all the scalers that are recorded; many of these, such as the detector rates, are used only for monitoring during the run. However, the live time and the charge are both used in the analysis. The live scalers are important to record because the DAQ cannot collect new events while it is processing an event, and it is the live integrated beam current that is appropriate for cross-section calculations. Measuring the live version of any scaler is possible using the

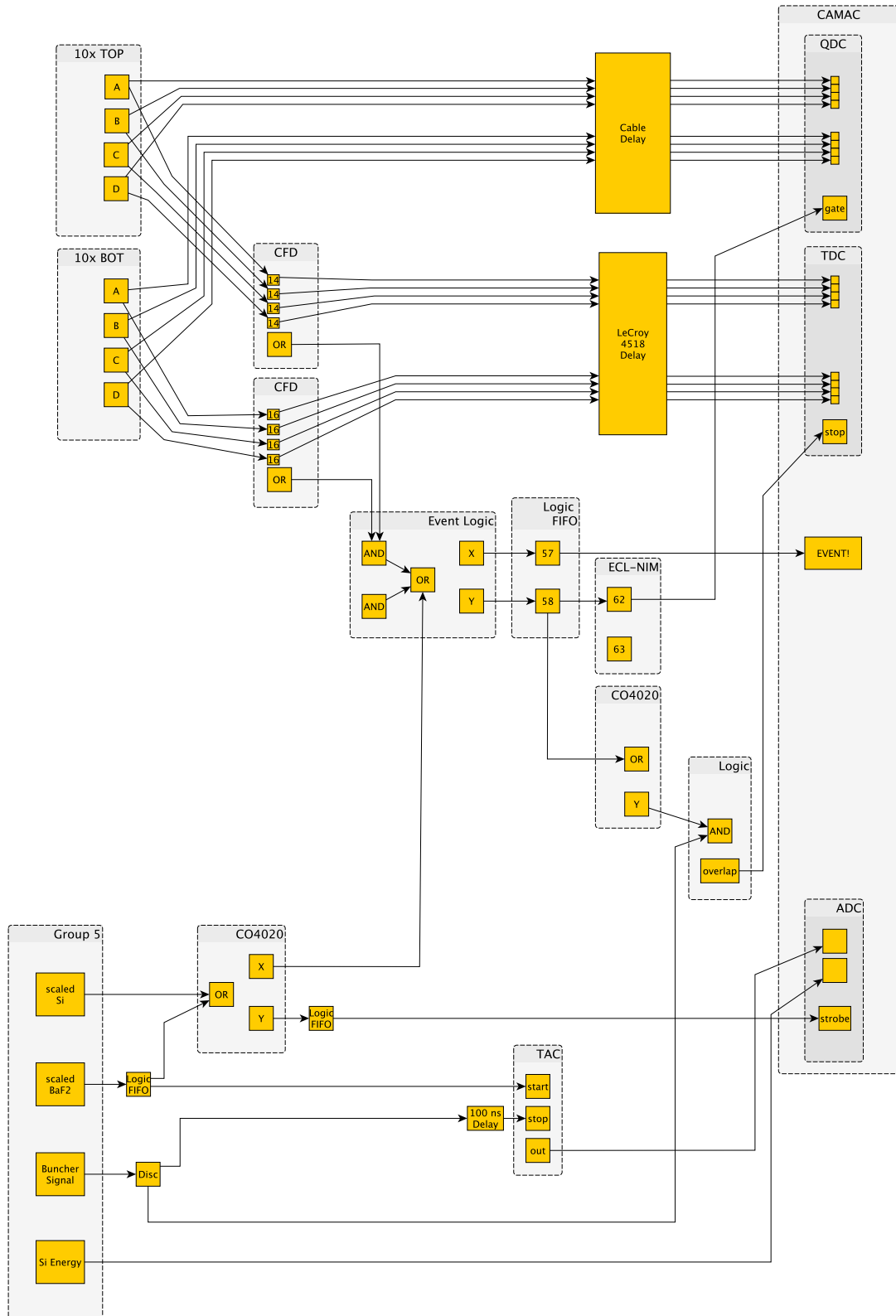


Figure 3.8: A diagram of the neutron detector electronics. The modules on the right are read by the DAQ.

busy signal the DAQ itself provides. The busy signal is a NIM logic pulse that is low when the DAQ is busy. Vetoing any scaler signal with this busy signal gives the live scaler, which is recorded in addition to the un-vetoed scaler. The schematic is shown in Figure 3.9. To turn the charge collected on the Faraday cup into a NIM signal that is compatible with the DAQ scaler, the Faraday cup is connected to a module that outputs a NIM logic pulse at a frequency that is proportional to the input charge. This signal, like all the others, is recorded in both its raw and vetoed form. A test of this electronics setup using a ^{26}Mg target verified the expected DAQ operation. This test is discussed in the next chapter.

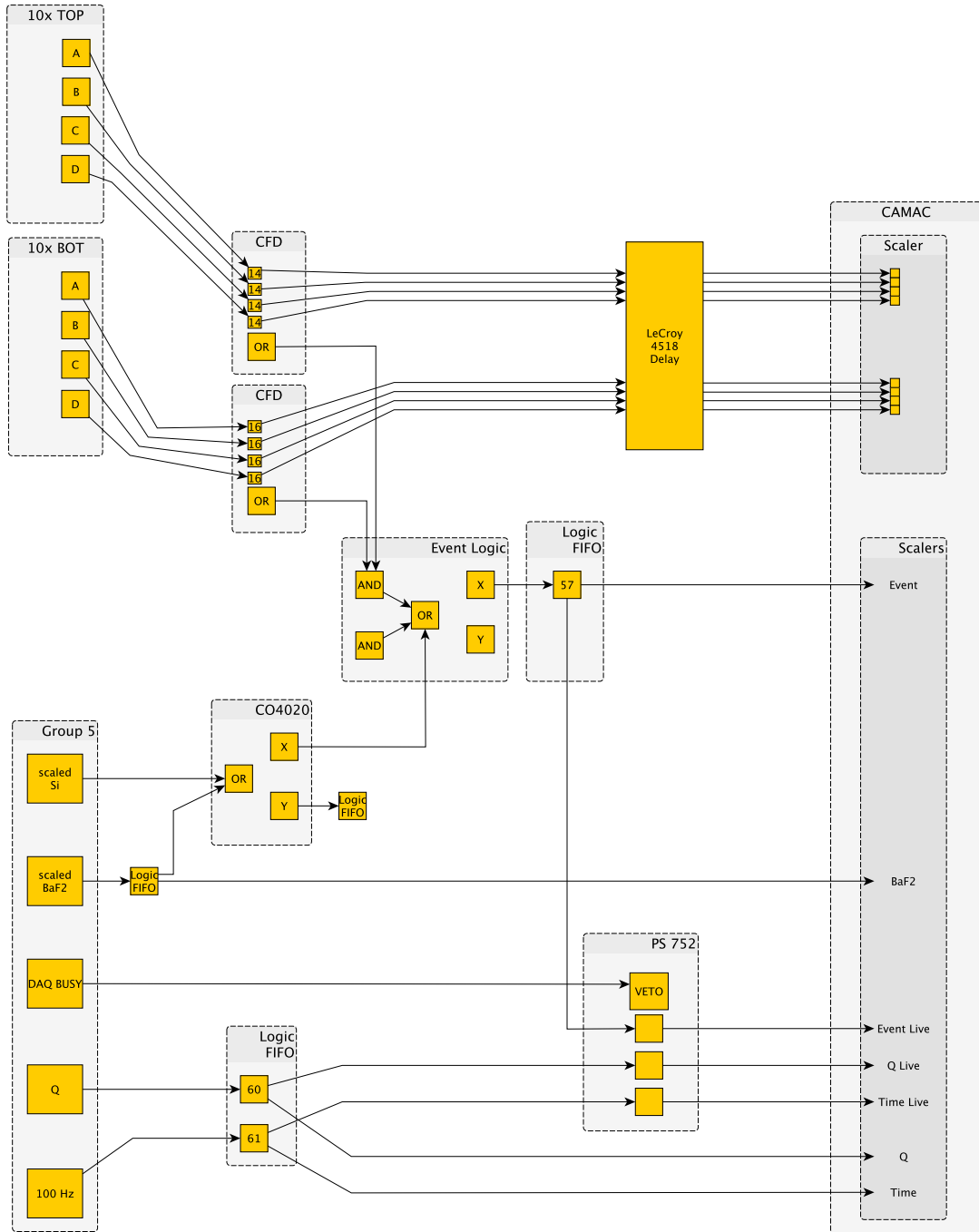


Figure 3.9: A diagram of the neutron detector scalers. The modules on the right are read by the DAQ independent of the event signal.

CHAPTER 4

MUON VETO DEVELOPMENT

4.1 Testing with $^{26}\text{Mg}(\text{He},\text{n})^{28}\text{Si}$

$^{74,76}\text{Ge}(\text{He},\text{n})^{76,78}\text{Se}$ cross-sections are predicted to be much lower than previous cross-sections measured with the neutron wall. A good candidate for testing the operation of the neutron wall is $^{26}\text{Mg}(\text{He},\text{n})^{28}\text{Si}$, which has a reasonably high cross section, on the order of 1 mb/sr, for 16 MeV ^3He beam and has neutron kinematics similar to $^{74,76}\text{Ge}(\text{He},\text{n})^{76,78}\text{Se}$. The differential cross-section of $^{26}\text{Mg}(\text{He},\text{n})^{28}\text{Si}$ has been measured at several energies bracketing 16 MeV [74, 75], which makes it an important check on the $^{74,76}\text{Ge}(\text{He},\text{n})^{76,78}\text{Se}$ absolute cross section.

Data on $^{26}\text{Mg}(\text{He},\text{n})^{28}\text{Si}$ were taken with the neutron detector setup as described in Chapter 3, with a beam energy of 16 MeV and a 1.94 mg/cm^2 thick ^{26}Mg target. The typical beam current was 20 nA. The TOF spectrum at the forwardmost angle, 6° , is shown in Figure 4.1. The neutron peak has a width of 1.2 ns and is clearly visible over the background.

The concerning thing about these data is that the high background rate severely limits sensitivity (see Section 5.6 for a discussion on setting limits with this data). This has serious implications for the $^{74,76}\text{Ge}$ experiment, where DWBA calculations predict the cross sections to be about a factor of three lower than those

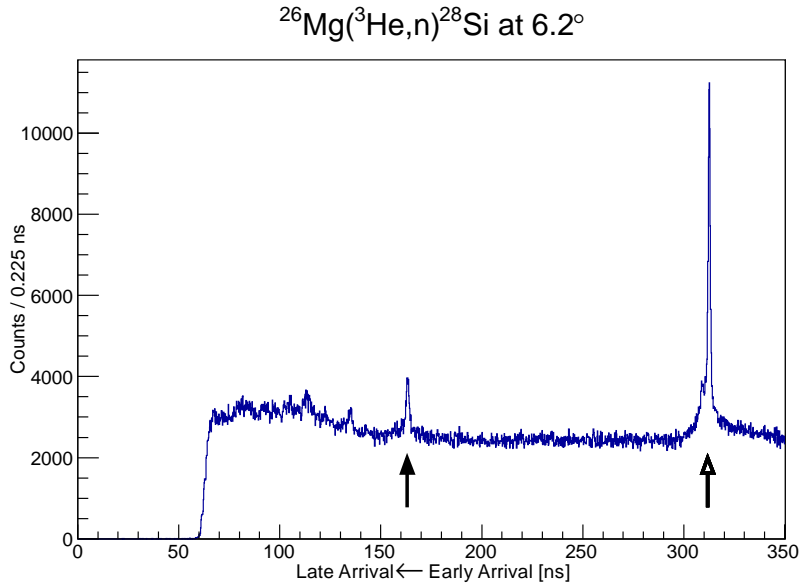


Figure 4.1: The 6° TOF spectrum for $^{26}\text{Mg}(^3\text{He},n)^{28}\text{Si}$. The light output threshold is set at 7.2 MeVee. A solid arrow indicates the ground state neutron peak and a hollow arrow the γ peak due to beam hitting the target.

for the ^{26}Mg target. Further lowering the event rate, the $^{74,76}\text{Ge}$ target must be thinner than the ^{26}Mg target to maintain the same energy resolution. Achieving sufficient precision on the ground-state cross section requires either reducing the background or increasing the beam current. The latter was not feasible because of ion source limitations (see Section 3.1 for details). The background comes primarily from low-energy γ radiation from the room and from muons produced by cosmic rays. Neither vetoing nor shielding against γ -radiation would be effective since materials with high γ interaction rates would not only scatter incoming neutrons but also be difficult to mount on the detector. Instead, software cuts on the energy are used to decrease this background and will be discussed in Chapter 5. The muons, however, are charged and can be readily identified with additional plastic scintillator. We therefore seek to reduce the muon component of the random background using a veto shield that registers the likely presence of a muon.

The events identified as muon events can then be discarded.

Identifying muons using additional scintillator material is possible because of the way that they deposit energy. The majority of muons traveling through the detector are Minimum Ionizing Particles (MIP's), which means that their energy loss is proportional to their path length in that material. An effective design for a muon veto, then, is to cover the neutron detector with independent plastic scintillator detectors. Signals in the neutron detector that are in coincidence with a signal in the "shielding" detector are likely to be muon events. While the charged muon will trigger both detectors every time its path through the scintillator is long enough to deposit energy above the detector threshold, the neutron is highly unlikely to interact in both detectors. The bars of the neutron detector are 5 cm thick; the chance of detecting a 20 MeV neutron with a typical threshold is 10%, making the chance of a neutron interacting in two such bars only 1%. The veto material available, donated from an inactive experiment by the University of Michigan, is only 1 cm thick, dropping the probability of a detectable neutron interaction in both to \sim 0.2%. By placing the available scintillator over the neutron detector bar, it is possible to identify muons to an accuracy of at least 99%. Note that such a veto does not identify γ radiation because its efficiency is similar to neutrons in the scintillating plastic.

4.2 Light Collection with Wavelength-Shifting Fiber

The scintillator bars of the neutron detector are outfitted with two PMT's, each coupled to one end via a non-scintillating light guide. Having two PMT's is essential both for good timing information and also to lessen the position sensitivity of the signal. Instrumenting the veto scintillators in this way was not feasible.

Fitting a top and bottom PMT to each veto bar would require 32 PMT's and lightguides, along with independent power supplies for each. Instead, wavelength-shifting (WLS) fiber was chosen to collect the light. The properties of the WLS fiber used in the veto paddles are shown in Table 4.1.

Properties	BCF-91A Multi-Clad WLS	Clear-PSMJ Multi-Clad Optical
Diameter, mm	1.0	1.2
Emission Color	green	n/a
Decay Time, ns	12	n/a
$1/e$ length, m	> 3.5	> 10
Core Material	Polystyrene	
Cladding Material	Acrylic	
Second Cladding Material	Flour-Acrylic	
Operating Temperature	-20° to 50°	

TABLE 4.1: Properties of Bicron BCF-91A WLS used in construction of the veto paddles. Values are taken from [76] and [77].

WLS fiber collects light by absorbing the blue and ultra-violet radiation produced by the scintillator and re-emitting that light in the green [78]. The fiber is coated with material having an index of refraction to maximize the spread of angles that experience total internal reflection, and so the light is contained in the fiber until it reaches a detector. WLS fiber minimizes position sensitivity when it is arranged on the detector so that no section of scintillator is more than 5 cm distant from the collecting fiber [79]. Because the fiber is fairly flexible, its pattern on the detector can be designed so that the fiber exits the plastic in a single bundle, allowing instrumentation with only one PMT. In the final veto paddle design, the area of the PMT face used by fibers from one veto paddle is small

enough that two veto paddles are instrumented with one PMT.

Possible disadvantages to WLS fiber are signal intensity and fragility of the fiber. Collecting sufficient light to boost the signal above the noise is a serious concern, and can be overcome by using many strands of WLS to collect light [80]. The fragility of the WLS fiber is more difficult to remedy. To maximize light collection, the fiber on the detector should be taken directly to the PMT, which should be as close to the plastic as possible to minimize signal attenuation. In some designs, this is achieved by enclosing the fiber run to the PMT in a stiff cast [81]. The design for the neutron wall needed flexibility in PMT placement, making a fixed support between the detector and PMT impractical. Several attempts were made to run the WLS collection fiber directly from the scintillator to the PMT, but the fiber quickly degraded and eventually snapped even with careful handling. Such degradation would have left no way to access the veto signals and was unacceptable. The decision was made to sever the WLS at the end of the plastic and make a robust optical cable to attach to the WLS fiber and carry the signal to the PMT. While severing the WLS fiber causes light loss [82], it ensures durability. The details of this design are discussed in the next section.

4.3 Paddle Design

The main components of a veto paddle are the scintillator, which generates light in response to energy deposition, the WLS, which collects the light, the endpiece that is epoxied onto the scintillator, which fixes the position of the WLS exiting the scintillator, and the optical cable, which connects to the WLS and carries the signal to the PMT. Each piece is discussed in this section. The epoxy used is an optical epoxy and is placed in vacuum after mixing to eliminate bubbles.

The scintillator material itself has a thickness of 1 cm, five times thinner than the bars of the neutron detector. Material of this thickness is desirable in order to minimize interaction of the neutrons with the veto paddles, but is thick enough to efficiently detect muons. The material is 17 cm wide and was cut to a length of 160 cm, making the veto paddle slightly wider and taller than a neutron detector bar. The scintillator had been stored in a warehouse with no temperature control for several years and was under mechanical strain during its storage. While some of the material readily responded to ultraviolet light and had a smooth, uncrazed surface, other material was badly damaged. Surface damage such as crazing was common, but some pieces had developed internal cracks, creating mirror-like surfaces within the scintillator. It was expected that the damaged bars would have poor efficiency, but instead they were found to function as well as paddles made of pristine material. The tests on efficiency are discussed later, in Section 4.4.

The design goal for the veto paddles was to maximize light collection while ensuring durability. One way to increase light collection is to use a fiber path that allows both ends of the fiber to terminate at the PMT. Light absorbed by the fiber propagates in both directions along the fiber axis; if one end of the fiber terminates, the light must reflect from that surface and travel back to the PMT. In this case, light loss occurs due to reflection at the terminating surface as well as attenuation along the path. Light loss at the terminating surface can be lessened somewhat with the application of reflective paint and more so by silvering the surface [83], but a simpler method of recovering the light is to loop the fiber on the scintillator as shown in Figure 4.2, which allows collection of light regardless of its travel direction. To further increase light collection, four fibers follow the fiber path, two on each side of the paddle. The arrangement is shown in

Figure 4.2. To ensure the durability of the veto paddle, the fibers are epoxied into channels machined into the scintillator to protect it from strain during handling. Coupling the fibers to the scintillator with epoxy also increases light collection [79]. Additionally, the bend radius chosen was 10 cm, which seemed to have no adverse effect on the WLS fiber. After construction, the veto paddle was wrapped in Tyvek, a diffuse reflector that is inexpensive and readily commercially available. Tyvek performs well at scattering light that has escaped the scintillator back into the active volume [84]. The paddle was also wrapped with two layers of thick, black plastic to shield the scintillator from light. This seemed effective, as room light did not affect the background rate in the assembled veto paddle.

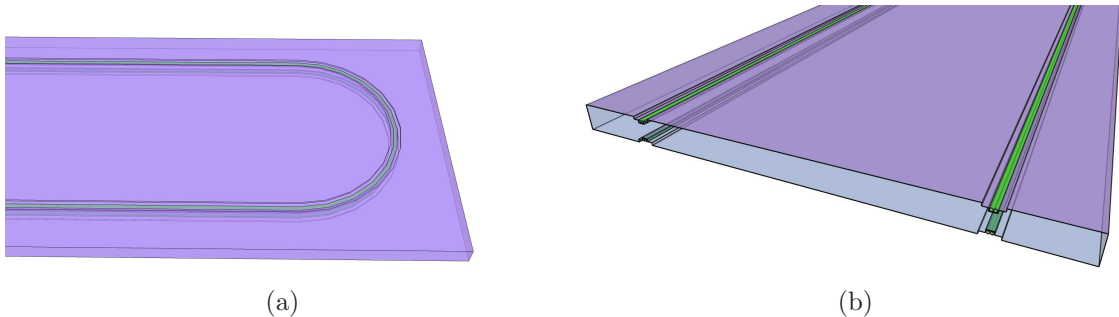


Figure 4.2: The WLS fiber is epoxied into a channel machined in the scintillator in a “U” shape to maximize light recovery (a). Two WLS fibers are embedded into each side of the plastic, as shown in the cutaway view in (b).

An endcap fitted to the scintillator helps protect the WLS and also fixes its location, allowing good alignment to the clear fibers in the optical cable. The endcap also minimizes possible flexing of the WLS fiber by connecting to machined indents in the scintillator with a press fit. Because the endcap extends

into the scintillator, bending of the WLS fiber perpendicular to its axis is essentially eliminated. Scintillator material is also machined away from the WLS fiber entrance to the endcap to avoid point pressure. This “ramping” can be seen in Figure 4.3. The wide acceptance funnels into small holes, one for each WLS fiber end, resulting in each fiber having a well-defined position on the surface of the endcap. This “clover” pattern on the surface of the endcap can be seen in Figure 4.3. It is important to note that the holes at the surface of the connector must have some clearance so that threading the WLS fiber through endcap does not strip the cladding from the WLS fiber or otherwise damage it. These fibers, slightly loose in their housing, are secured into place with optical epoxy to allow effective polishing of the surface. To optimize light transmission from the WLS fibers to the optical cable’s clear fiber, the surface is polished with a bull-nose, single-crystal diamond.

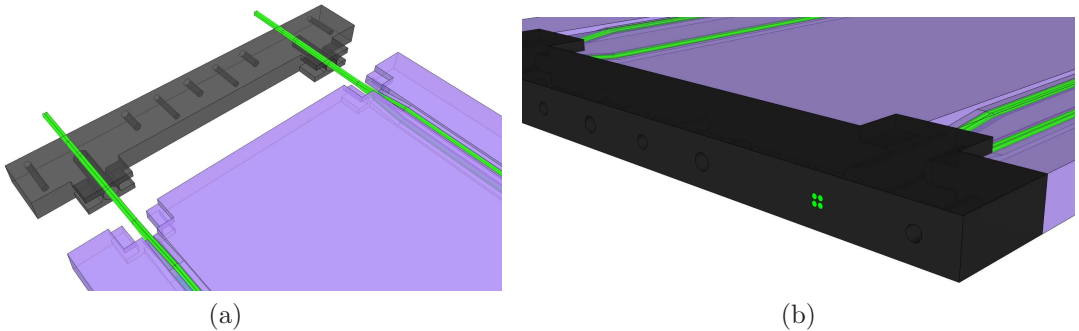


Figure 4.3: (a) The endcap is epoxied to the scintillator after it is slid into place to secure the WLS fibers. (b) The WLS fibers at the surface of the endcap form a “clover” pattern that aligns with the clear fibers in the optical cable.

The optical cable consists of two groups of four-clusters of clear fiber, one

group for each of the four-clusters of WLS fiber exiting the scintillator. Clear fiber, whose properties are shown in Table 4.1, is preferable to WLS fiber because it is optimized for transmission and is also more durable. The optical cable housing must ensure that each clear fiber completely overlaps its WLS fiber and also that the clear fiber is protected from damage en route to the PMT. To accomplish this, the optical cable consists of two types of connectors, one that mates with the endcap attached to the scintillator and another that connects to the PMT, each connected by slightly stiff tubing (durometer = Shore A80) that encases the 2 m long clear fibers. This tubing helps protect the clear fiber by limiting its bend radius and also acts as a light shield. At each interface between tubing and connector, the primary concern is that the stresses on the clear fiber be small enough to avoid damage. A hose barb attached to each connector allows the clear fiber through and also allows the tubing to firmly connect without straining the fiber. An optical cable is shown in Figure 4.4. Each optical cable has two groups of clear fiber that connect separately to a cap on the PMT. Each PMT cap can accept four independent cable connections, allowing two veto paddles to be instrumented by one PMT. The PMT cap, PMT connector, and endcap connector are machined from black delrin, an opaque plastic that contributes to the light-tightness of the optical cable and is stiff enough to be easily machined.

The primary design constraint for the portion of the optical cable that attaches to the endcap is that each clear fiber completely overlaps its WLS fiber. The diameter of the clear fiber is 1.2 mm, larger than the 1 mm-diameter WLS fiber, which allows misalignment up to 0.1 mm without greatly impacting light collection. Tight-fitting stainless steel dowels help align the fiber clusters. This is particularly important because the connectors are machined from plastic and

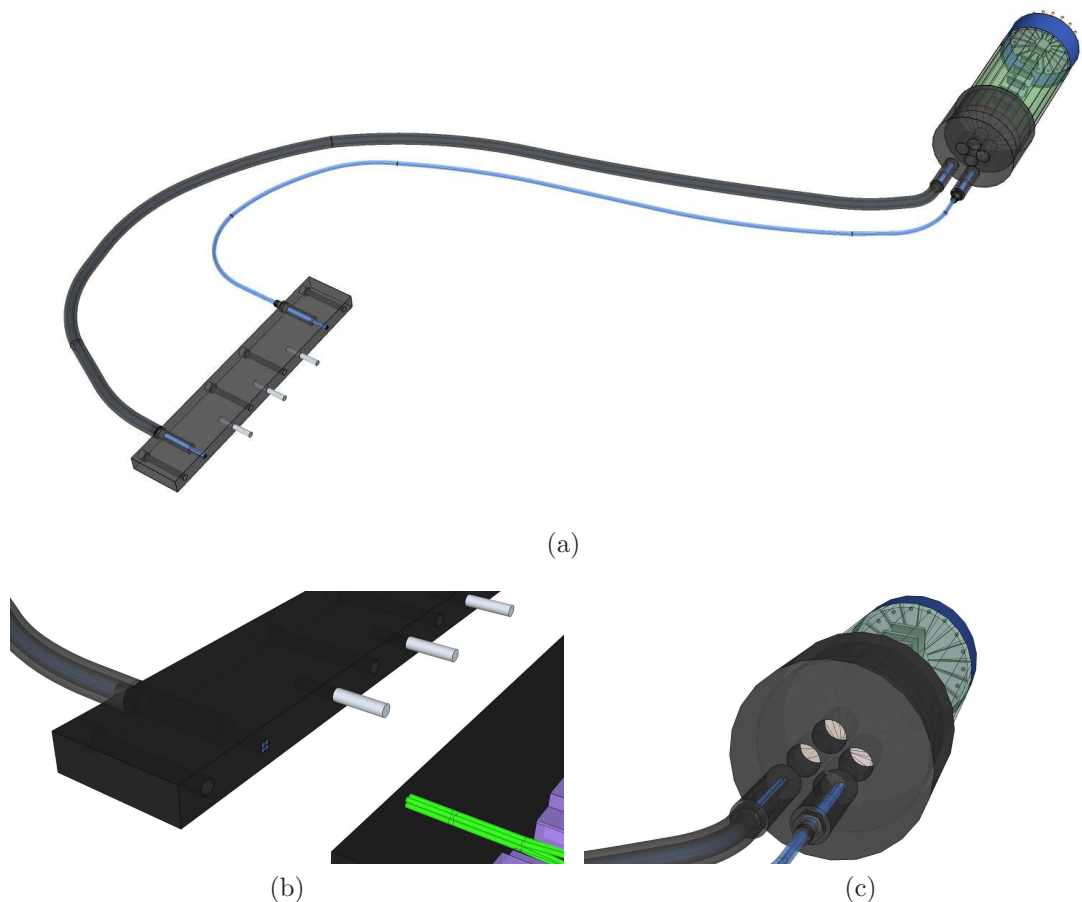


Figure 4.4: (a) Dowels help the clear fiber align with the WLS fiber on the endcap. The protective tubing covers both groups of clear fibers but is shown here on only one group. (b) The clear fibers align with the WLS fibers exiting the veto paddle. (c) The clear fibers are held in place on the PMT surface.

are not perfectly square - some connectors bow as much as 0.5 mm from normal. The only regions that must be carefully aligned, however, are those near the fiber clusters, and the dowels ensure accurate alignment. Like the WLS fibers in the endcap, the clear fibers must be epoxied in place so that the mating surface can be diamond-polished without damage.

The connector that terminates at the PMT is cylindrical to make machining of the PMT cap simple. In contrast to the endcap connector, the PMT connector has minimal constraints on the position of the clear fibers because the entire 5 cm-diameter PMT face is sensitive to light. The end of the PMT connector, like the endcap and the endcap connector, is diamond-polished to maximize optical coupling, and so the fiber is epoxied into place to protect it from damage during polishing. As with the endcap connector, strain relief is provided to the optical cable by attaching the protective tubing to the connector with hose barb, eliminating extreme bending of the optical cable. The cap fitted to the face of the PMT has four holes drilled with a diameter that provides a press-fit with the PMT connectors from the optical cable. The cap fits snugly onto the PMT so that the optical cables in the PMT connectors are held securely to the surface of the PMT. The diamond polishing results in a very uniform surface. It was found that applying optical grease to the connection did not result in noticeable improvement, and the coupling to the PMT was therefore left as an air coupling. One way to improve light collection by the PMT was to place the clear fibers closer to the center of the PMT face. This was done by machining PMT caps with the holes for the connectors drilled as closely as allowed by the plastic, \sim 2 mm.

4.4 Paddle Performance

The intrinsic efficiency of the paddles can be tested by requiring a coincidence with several paddles. The several-detector coincidence identifies signals as muons. If the coincidence paddles are arranged so that the path of any muon intersecting all the veto paddles must also intersect the volume of the veto paddle, the intrinsic efficiency of the veto paddle can be measured separate from its geometric coverage.

In practice, arranging the available scintillators to confine muon paths through the test volume was difficult because the available scintillator was instrumented with bulky lightguides and could not be laid directly on the test volume. A simple cosmic-ray simulation program helped determine an arrangement that guaranteed a geometrical efficiency of at least 99%. This arrangement is shown in Figure 4.5. Note that the coincidence paddles are slightly wider than the veto paddle, which requires the coincidence paddles to be aligned to each edge of the veto paddle.

The efficiency was measured by counting how often the veto paddle had a detectable signal when all the coincidence paddles registered a coincidence. Assuming that the muon is thereby constrained to travel through the veto paddle volume, the ratio gives the intrinsic efficiency. The DAQ event signal was a logic pulse resulting from the coincidence of the coincidence paddles. This logic pulse also acted as a start for a time-to-amplitude converter (TAC). The TAC stop signal was a delayed, discriminated veto paddle signal. The outgoing TAC signal was then sent to an analog to digital converter (ADC). Signals from the veto paddle coincident with the other scintillators appear in the timing spectrum as a peak at the time of the delay as in Figure 4.6. The integral of this timing peak divided by the number of event triggers gives the efficiency.

Testing the efficiency of the veto paddle with this setup was not ideal because

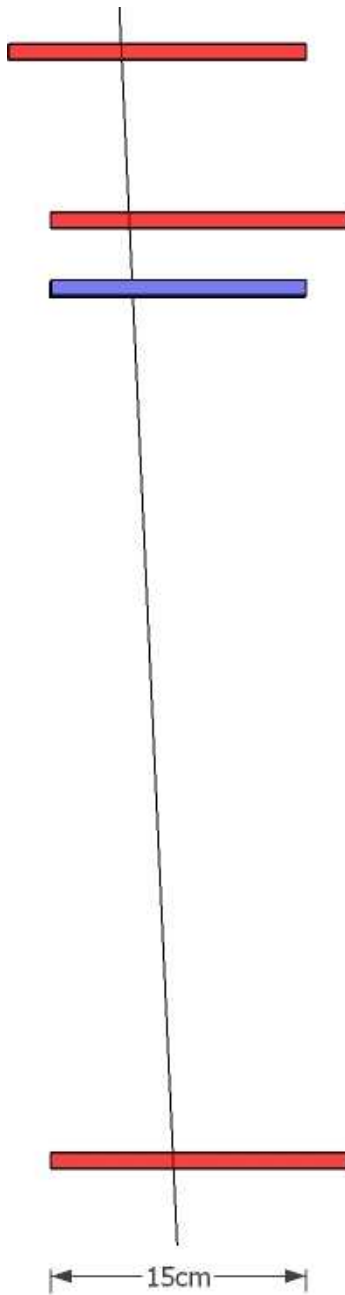


Figure 4.5: This arrangement of coincidence material ensures that muons triggering all coincidence detectors must also travel through the veto paddle. The coincidence material is drawn in red while the veto paddle is in blue.

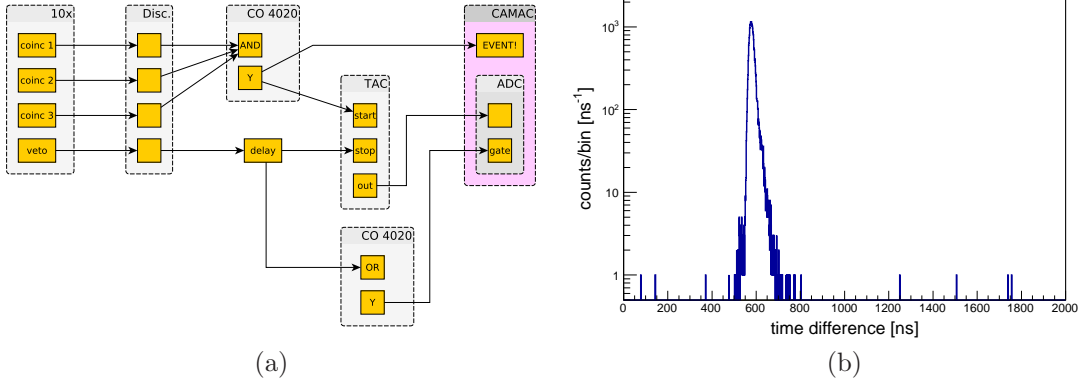


Figure 4.6: A diagram describing the veto paddle test electronics is shown in (a). The location of the timing peak in (b) is set by the delay introduced to the discriminated veto paddle signal. Integrating the timing peak gives the number of muons that generated an observable signal in the veto paddle.

the geometrical efficiency was very sensitive to the placement of the coincidence detectors. The measured efficiency of the same bar could change from 98% to 75% when the middle coincidence detector was shifted away from the edge of the veto paddle by as little as a few centimeters so that careful adjustment of this geometry was required. However, this setup was useful in testing the effect of the optical cable polishing, cable out-of-true-ness, and the condition of the plastic scintillator. In general, all efficiency measurements fell between 94% and 98%. Even the veto paddles made of plastic with deep internal cracks were as efficient as those made from the plastic in excellent condition. No statistically significant differences were seen between optical cables made with badly bowed connectors and nearly true connectors. Polishing the surface of the optical cables with the bull-nose single-crystal diamond rather than a commonly-available multi-crystal diamond bit increases detection efficiency by $\sim 2\%$, although it should be noted that the change may have been due to correlated noise in the system rather than to improved light transmission. The discriminator threshold, set to its lowest value

at -15 mV, gave an efficiency of 98% compared to 94% when set to its highest value at -1.023 V. These levels are indicated relative to a typical pulse from the veto paddle in Figure 4.7

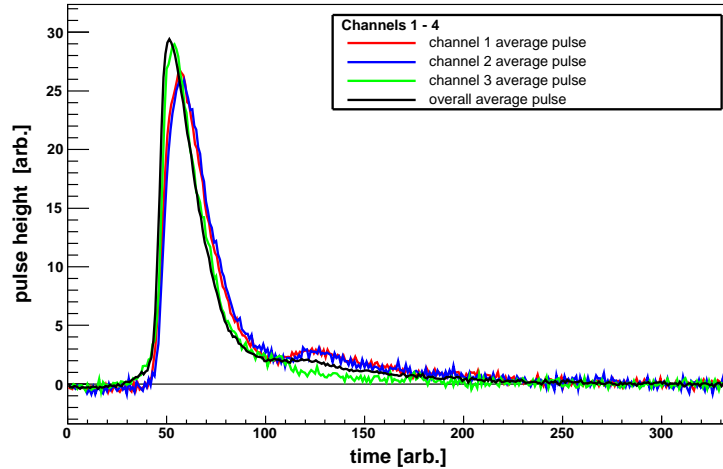


Figure 4.7: Pulses from muons in the veto paddles.

Testing the position dependence of the efficiency using the setup described above was not practical due to its sensitivity on alignment. Instead, the response of the veto paddles to a loosely collimated γ -ray source was tested. A ^{60}Co source was inserted into a lead ring and raised 2 cm within the ring by a small piece of plastic. The lead ring had a wall thickness of 3 cm and a hole diameter of 2.5 cm. This collimated source was then placed at three positions along the veto paddle: near the endcap, at the middle of the paddle, and near the end of the paddle. Several measurements were taken at different positions along the short axis of the veto paddle, all at the center of the paddle's long axis. The detected rate of γ

radiation showed a deviation of less than 10% over the veto paddle. While this is not a measurement of the position dependence of the muon efficiency, it does limit the efficiency change over the paddle since muons typically deposit at least twice the energy of the γ radiation from the ^{60}Co source. See Figure 4.8 for the variation of the efficiencies.

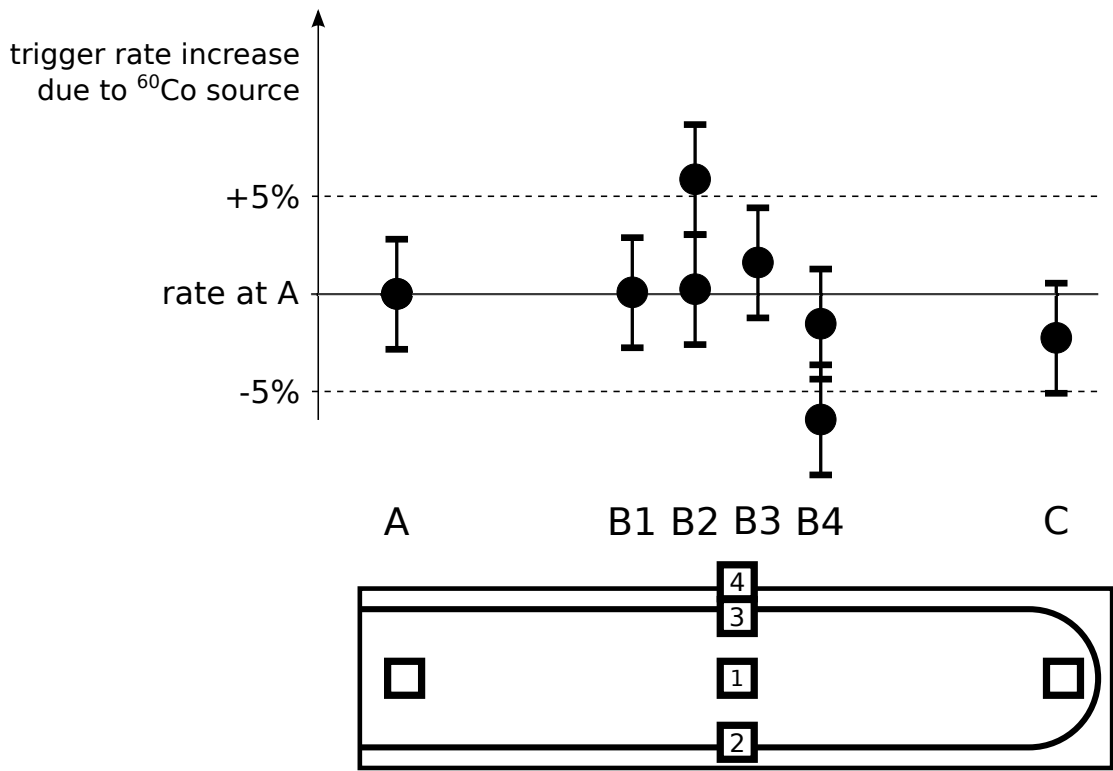


Figure 4.8: The dependence of the number of detected events on the position of a loosely-collimated ^{60}Co source. The image below the graph shows the positions of each measurement relative to the veto paddle. Data was taken in the center across the bar to test for horizontal position dependence. The position B1 is at the horizontal center and B4 is at the edge of the veto paddle. Two measurements were taken at B2 and B3, the points nearest the WLS fiber channel to verify the reproducibility of the measurement. The spread is approximately 10%.

4.4.1 On-Detector Efficiency

Sixteen veto paddles were initially mounted ~ 2 cm in front of the neutron detector bars to avoid removing them and potentially causing damage. See Figure 4.11 for a detailed view. The veto rejection is strongly dependent on the energy of the lower energy cut applied to the dataset, as shown in Figure 4.9. All efficien-

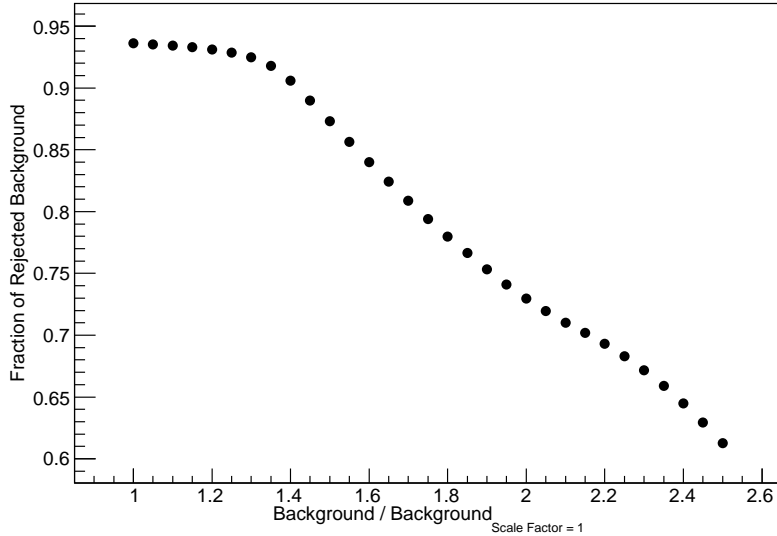


Figure 4.9: The fraction of background rejected by the veto as a function of the lower-energy cut. The energy cut is shown as a ratio between the background due to the cut and the background due to a reference cut; increasing numbers on this scale implies a lower-energy cut. This cut is discussed in detail in Chapter 5, Section 5.4.

cies cited are based on datasets where the lower energy cut applied to the data was that used in the final data analysis, 7.2 MeVee. A test with $^{26}\text{Mg}(^{3}\text{He},\text{n})^{28}\text{Si}$ showed the background was reduced to $\sim 12\%$ the original background in the two

innermost bars of each four-bar unit but only to $\sim 18\%$ in the outer two bars. The outer bars act as additional veto material for the inner bars, have no such additional information themselves to aid in muon identification. It should be noted that adjacent veto paddles were instrumented by a single PMT, making it impossible to distinguish veto signals from distinct veto paddles.

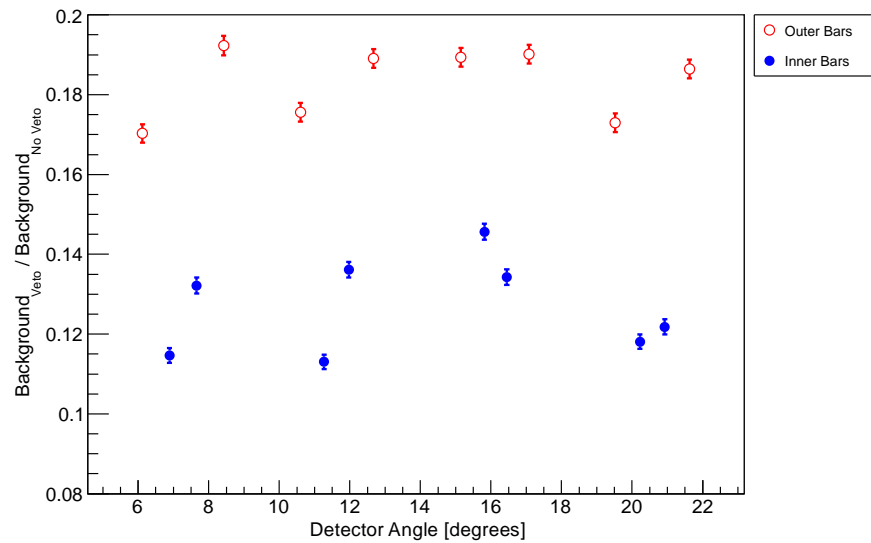


Figure 4.10: Ratio of room background with and without veto rejection with the initial placement of the veto paddles. Note that the rejection is worse for bars on the ends of each group of four (red) and better for internal bars (blue). The rejection depends on the lower energy cut placed on the data; the energy cut here is that used in the final data analysis, at 7.2 MeVee.

A simulation of the muon background indicated that the geometrical efficiency was very sensitive to the distance between the veto paddle and neutron detector bar as well as the distance between the bars of the neutron detector. The bars

in the neutron detector were moved as close as the mounting screws would allow, within 1 cm. Instead of attaching the veto paddles on top of the retaining bars on the neutron detector, they were taped to the bars and both bar and veto paddle were supported together by the same retaining bar. The separation between the bars of the neutron detector and their veto paddle is \sim 0.5 cm due to stiff foam placed between the two to protect the WLS channels in the veto paddles. The arrangement is shown in detail in Figure 4.11.

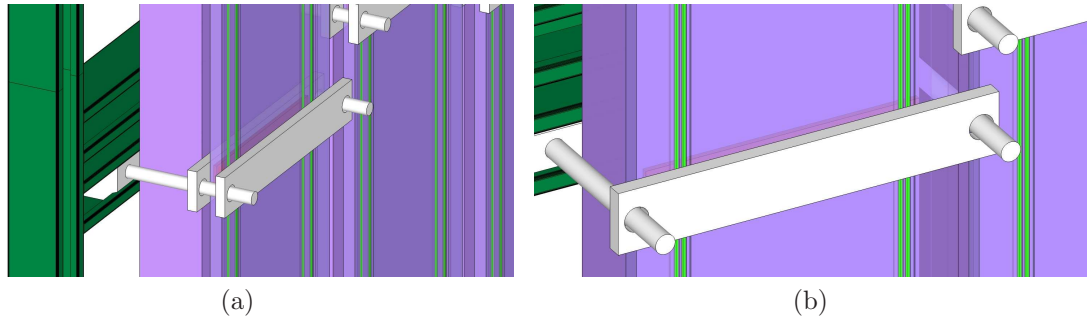


Figure 4.11: (a) The veto paddles are secured to the neutron detector bars with an additional retaining bar. (b) A veto paddle and a neutron bar are secured together with a single aluminum bar to minimize their separation. Stiff rubber (in orange) on either sides of the veto paddle again protects the scintillator from any point pressures that could result from its uneven surface.

Material was also added to the sides of the outermost neutron detectors. The final setup is shown in Figure 4.12. These changes improved both the average and uniformity of the background rejection, as can be seen in Figure 4.13.

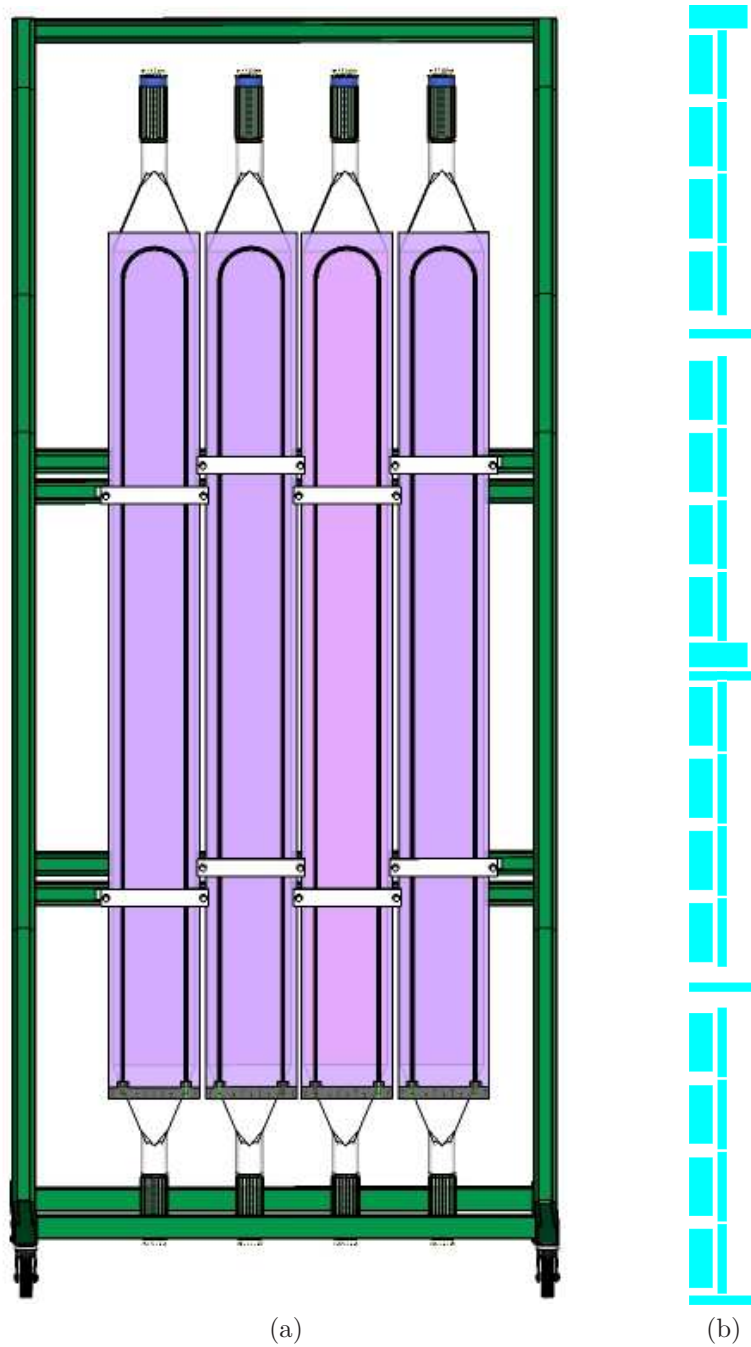


Figure 4.12: (a) The final arrangement of the veto paddles on a segment of the neutron detector. The distance between the veto paddles and the bars of the neutron detector have been minimized. (b) A bird's eye view of the neutron detector and veto paddles. Note the addition of veto material on the sides of the neutron detector sub-units.

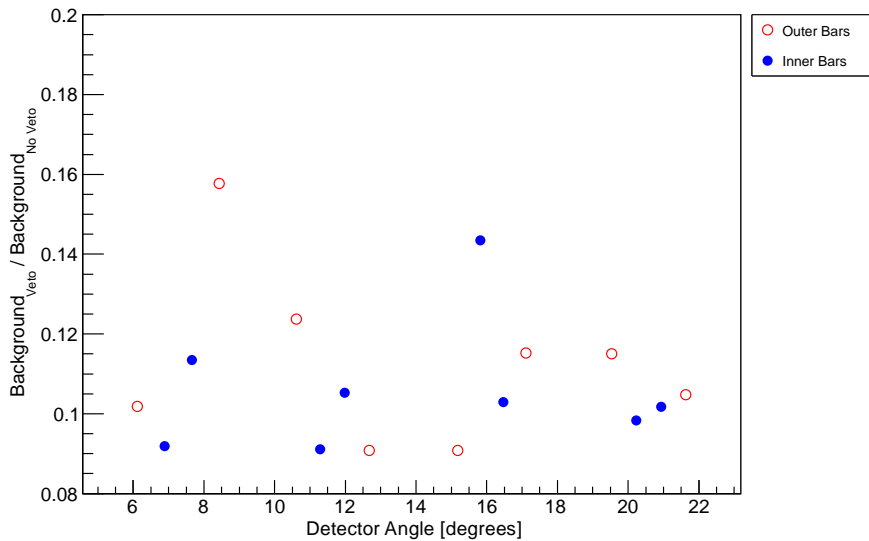


Figure 4.13: Ratio of room background with and without veto rejection in final setup. Note that the rejection ratio for a typical paddle is about a factor of 10. Bars at the ends of the group of four (red) enjoy similar background rejection to internal bars (blue) on average. The errors are accurately represented by the size of the points. The veto rejection is dependent on the lower energy cut applied to the data; the energy cut for the rejection reported here is that used for the final data analysis, 7.2 MeVee.

4.5 Electronics

As mentioned above in Section 4.4, tests on single veto paddles were done using a timing spectrum. Recording complete time information for the full veto was not practical, and bit registers were used instead. A bit register has several inputs, each corresponding to a bit in an integer, and a gate. When the gate is open, the bit register records the pattern at its inputs. Each input is connected to a discriminator which fires when the signal from the given veto bar exceeds a threshold. The result is a unique representation of which bars fired during the time specified by the gate. If the gate used is the event signal from the neutron detector, the bit register will record which veto paddles fired during an event of interest. Two 16-channel LeCroy 4532 bit registers were used to instrument all the veto paddles. The gate signal was a 200 ns-wide logic signal generated from the event trigger.

Recording the integer generated by the bit register instead of the time of the signal relative to the beam bunch results in a loss of information. The maximum time difference between an event in the neutron detector and an event in the veto that will still be recorded in the bit pattern is the width of the gate signal, 200 ns. This compares unfavorably to the timing spectrum where even with a leading edge discriminator, the timing peak has a width of less than 5 ns. The concern is that this loss of precision in timing information will lead to unacceptable vetoing of real events.

Several sources contribute to non-beam-related background radiation, resulting in a beam-off rate in a neutron detector bar of \sim 1000 Hz. While some of these events are due to muons, they have a flux of \sim 5 Hz/m² [9] and are therefore a small part of the beam-off noise rate. The beam-off rate, then, serves as a

suitable rate with which to calculate an upper bound for the rejection of beam-related events. The probability that one or more noise events will occur within the window allowed by the bit register and veto a beam-related event is

$$1 - e^{\tau_{\text{bit reg.}} R_{\text{noise}}} \simeq R_{\text{noise}} \times \tau_{\text{bit reg.}}, \quad (4.1)$$

where R_{noise} is the noise rate and $\tau_{\text{bit reg.}}$ is the time window of the bit register. The neutron detector bars that experience the highest veto noise rate are those that are vetoed by four detectors. Two of these are the veto paddles mounted directly in front of it and the adjacent neutron detector bar, and the other two are the bars on its sides. The two front veto paddles have a combined noise rate of 1000 Hz, while the two side veto paddles could each have a rate of 1000 Hz, giving a maximum noise rate of 3000 Hz. The bit register window was set at 200 ns, so that the maximum probability of vetoing a real, beam-induced event is 6×10^{-4} , or approximately one false veto per 1500 events. This fraction of vetoed events is less than 1% and will not have any statistical significance, even with the timing resolution lost by moving to a bit register. A schematic of the veto electronics is shown in Figure 4.14. Note that no changes to the DAQ other than the addition of the bit register are required.

4.6 Beam Tests

The final veto system reduces the background by approximately a factor of 10 as can be seen in Figure 4.15. The rejection is strongly dependent on energy cuts placed on data, as shown in Figure 4.9. The veto is less effective at lower energy cuts because γ radiation becomes a significant contributor to the random background. Placing energy cuts above the thorium edge, the Compton edge

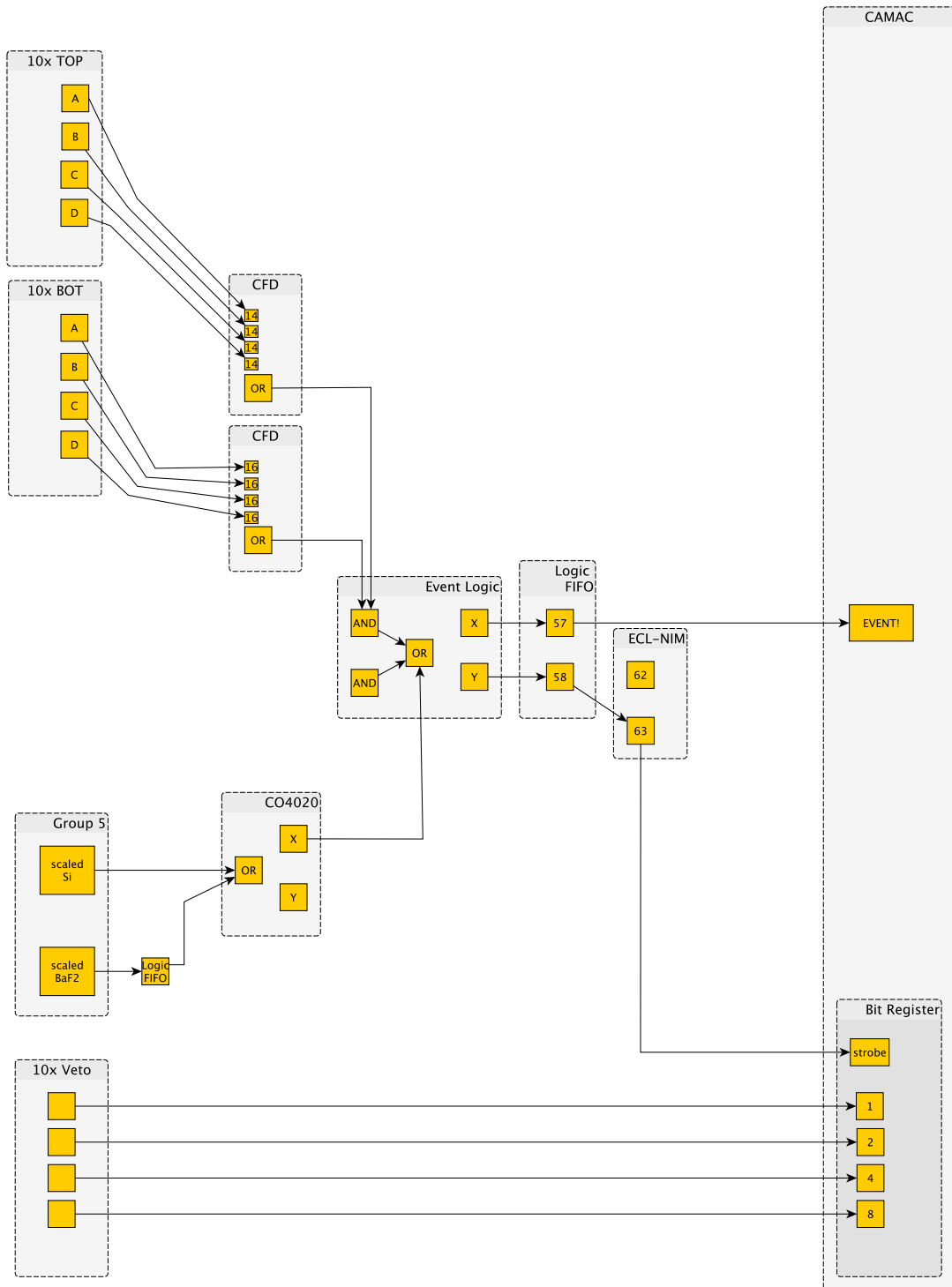


Figure 4.14: The integration of the veto electronics with the existing DAQ. The bit register is used in the data analysis. Scalers are also added for run-time monitoring.

resulting from the maximally scattered 2.6 MeV γ -ray [9] from a natural thorium source, rejects much of the room γ background. Placing a such a high cut on the energy also discards neutron events, so that minimizing the background is in conflict with maximizing the signal. Optimizing the energy cut is discussed in Chapter 5, Section 5.4 and confirms that requiring the signal to be above the thorium edge maximizes the signal/background ratio. Applying the veto to a data set with this low-energy cut reduces the background on $^{26}\text{Mg}(^3\text{He},\text{n})^{28}\text{Si}$ by approximately a factor of 10. The statistical errors on the reaction populating the ground state were reduced from 7% to 3%. See Chapter 5, Section 5.5.1 for a discussion on the calculation of statistical error.

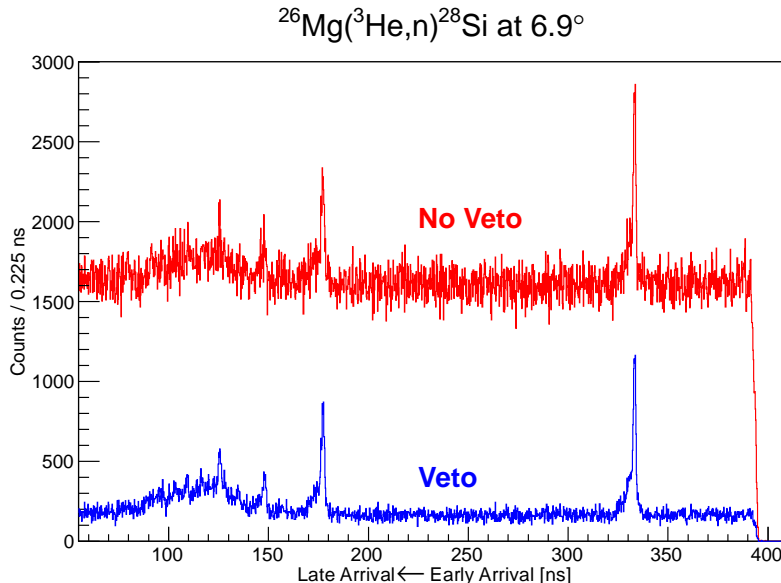


Figure 4.15: The effect of the veto on the $^{26}\text{Mg}(^3\text{He},\text{n})$ data. The light output threshold is set at 7.2 MeVee.

4.6.1 Rejected Signal

While the achieved background rejection is excellent, it is important to consider how often the veto rejects real neutron events. Such a rejection could occur when a neutron interacts in both the veto and the neutron detector, when the neutron detector sees a real signal and the veto triggers from an uncorrelated event such as a background γ -ray, or when a neutron interacting in the detector ejects a proton that triggers the veto. This last case is the primary reason we chose to mount the veto on the front of the detector. In these cases, the vetoing of real events will result in timing peaks on top of the flat, random background of the rejected events, and placing a limit on the neutron peak in the rejection spectrum will give a maximum rate for all these processes together. Cases where the neutron scatters away from the detector in the veto material will not contribute to a timing peak, but because the low rate of scattering from the veto paddle material is also severely limited by solid-angle this is not considered here. Figure 4.16 shows the rejected events for all current ^{26}Mg data; no neutron peak is visible. Given the background, this places a limit on the total rejection of real neutron events of less than 8% at a 95% confidence level.

Testing with $^{26}\text{Mg}(^3\text{He},\text{n})^{28}\text{Si}$ demonstrates that the muon veto reduces background by approximately a factor of 10 and does not veto a significant number of beam-related events. In addition to verifying the proper functioning of the veto system, this reaction also measures the efficiency of the neutron detector because the cross-section is well known. These efficiency calculations, as well as the data from the $^{74,76}\text{Ge}$ experiments, will be discussed in Chapter 5.

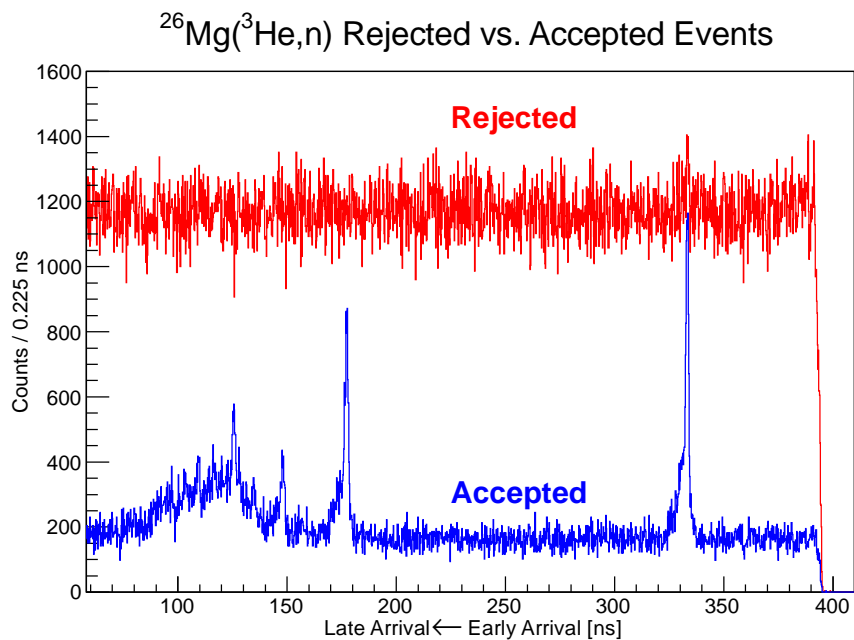


Figure 4.16: A plot of the accepted and rejected events. Peaks in the rejected spectrum are from real, vetoed events. No neutron peak is visible. The light output threshold is set at 7.2 MeVee.

CHAPTER 5

DATA ANALYSIS

The aim of the analysis of the $^{74,76}\text{Ge}(^3\text{He},\text{n})^{76,78}\text{Se}$ data sets is to extract the absolute cross section of the reactions populating the ground states of $^{76,78}\text{Se}$ and also to set a limit on excited 0^+ -state cross sections. Each of these analyses is discussed in its own section, but because the absolute cross section is of interest, the detector efficiency and several other properties of the experiment must be accurately determined. The measured quantities used most frequently in this analysis are the timing relative to the beam bunch and the light signal. “Time” in this chapter always refers to the arithmetic average of a bar’s top and bottom time values. A timing spectrum is shown in Figure 5.1. Another measurement important for analysis is the integrated light output at the top and bottom of a bar. A geometric average of these, $\sqrt{E_t E_b}$, where E_t and E_b are the integrated light signal of the top and bottom PMT, respectively, is considered a measure of the neutron energy and is referred to as “energy” in this chapter. This quantity is discussed further in Section 5.4. The top and bottom PMT signals, taken separately, are not necessarily a measure of the energy of the event and will be referred to as “light signals” when used without averaging.

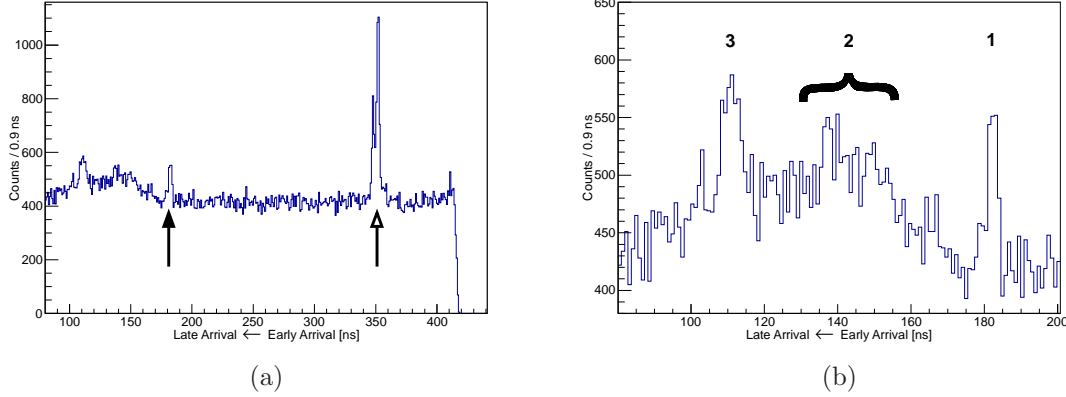


Figure 5.1: (a) A (time of flight) (TOF) spectrum from the forwardmost neutron detector bar (6.1°) in the case of pulse-selected beam. The reaction is $^{74}\text{Ge}(\text{He},\text{n})^{76}\text{Se}$. The ground-state neutron peak is indicated with a solid arrow and the γ peak with a hollow arrow. Note that the γ peak is doubly peaked, from beam hitting the target and then the beamstop. (b) The neutron spectrum. The ground-state neutron peak is indicated with a “1”, the neutron continuum with a “2”. The other prominent peak, labeled “3”, is due to oxygen contamination in the target.

5.1 Detector Efficiency

The number of counts due to neutrons measured by the detector scales linearly with the absolute cross section of $^{74,76}\text{Ge}(\text{He},\text{n})^{76,78}\text{Se}$ but must be corrected for the fact that not all the neutrons leave a signal in the detector. The ratio of the detected neutron flux to the total neutron flux is called the efficiency of the detector and must be carefully determined as its error contributes directly to the systematic uncertainty of the extracted absolute cross sections.

The efficiency of a plastic-scintillator-type neutron detector depends not only on the energy of the neutron, but also on the detector’s size, shape, energy resolution, and detection threshold. A Monte-Carlo code developed by Cecil [85] calculates the efficiency of plastic scintillator detectors for a wide range of neutron energies and detector thresholds to within 10%. The Cecil code was used

to calculate efficiencies of the neutron detector for neutrons with energies of 10-28 MeV. The efficiencies predicted by the Cecil code were verified against $d(d,n)$ and $^{26}\text{Mg}(^3\text{He},n)^{28}\text{Si}$ measurements, both of which have well-known cross sections. Comparing the calculated efficiency to measured efficiency over a range inclusive of the neutron energies produced in $^{74,76}\text{Ge}(^3\text{He},n)^{76,78}\text{Se}$ gives confidence that the code accurately models the detector. The inputs required by the code are the density of the detector, its hydrogen to carbon ratio, the energy threshold applied to the data, and the interval over which the detector averages the light output, i.e., the resolution of the detector. The plastic properties are reported in Table 4.1, and the threshold and resolution of the detector must be determined from the energy spectrum of the selected events from the experiment. The cuts applied to the data are discussed in Section 5.4. An energy spectrum of the ground-state neutrons of any of the reactions studied can be produced by gating on the ground-state peak in the TOF spectrum. The energy spectrum for the ground-state neutrons from $^{26}\text{Mg}(^3\text{He},n)^{28}\text{Si}$ is shown in Figure 5.2. The width of the high-energy falloff gives the resolution of the detector, and the threshold can be determined by assuming the scale has a zero offset. That this is a reasonable assumption is confirmed by the accuracy of the calculation.

The efficiencies calculated using the above method must be checked for absolute accuracy of the prediction as well as accuracy of its predicted dependence on the energy of the detected neutron. The reaction $d(d,n)$, measured at beam energies near 9 MeV [86], produces ground-state neutrons and is particularly useful because the neutron energy changes drastically as a function of angle, making it a useful check on the energy dependence of the Cecil prediction. Additionally, empirical fits as described in Reference [86] provide excellent estimates of the ab-

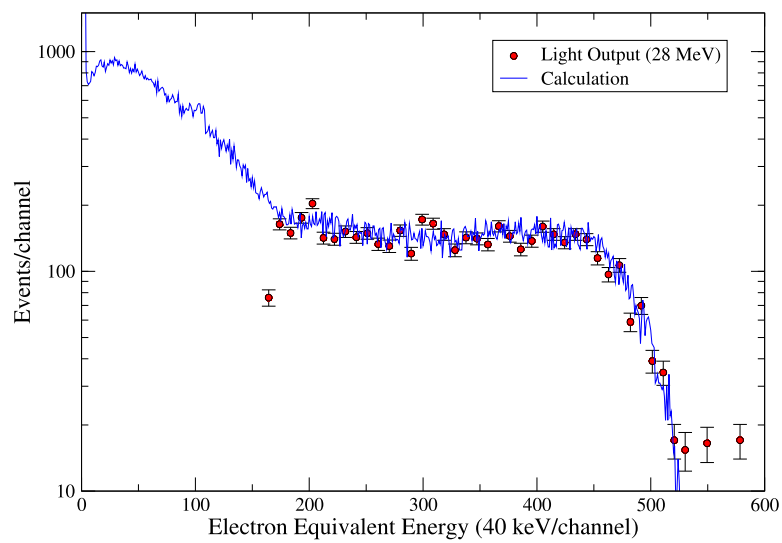


Figure 5.2: The light curve for 28-MeV neutrons from $^{26}\text{Mg}({}^3\text{He},\text{n}){}^{28}\text{Si}$ is obtained by restricting the events to those in the ground-state peak window. The data points shown in red are from the January dataset.

solute cross section in this energy region. The agreement is excellent, as can be seen in Figure 5.3, which shows the prediction with and without correcting for neutron energy. This result suggests that the Cecil code accurately adjusts the detector efficiency for neutron energy.

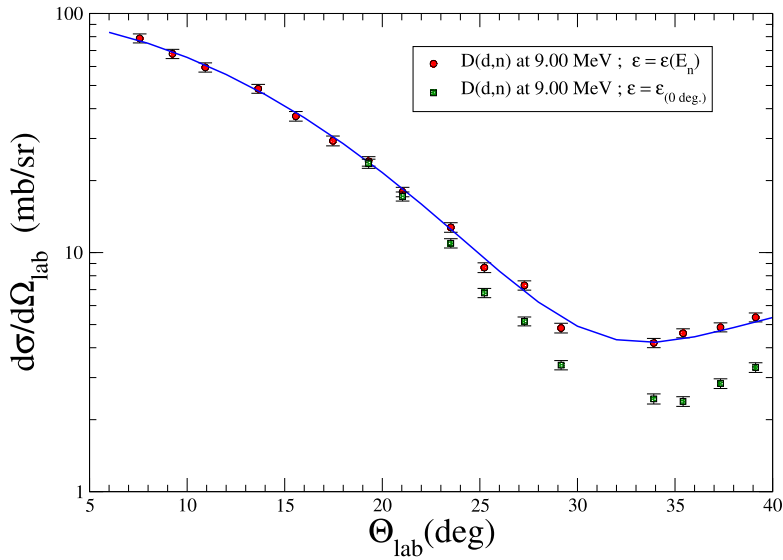


Figure 5.3: The prediction for $d(d,n)$ (solid line) matches the data well when the efficiency is corrected for the neutron energy (red points). The blue points represent the differential cross section where the efficiency is assumed to remain constant despite a changing neutron energy.

That the Cecil code appears to be successful in calculating the efficiency of the neutron detector for 12-MeV neutrons is encouraging, but neutrons from the ground states of $^{74,76}\text{Ge}({}^3\text{He},n)^{76,78}\text{Se}$ will be ~ 26 MeV. A reaction with measurements of cross sections for neutron energies in this range is $^{26}\text{Mg}({}^3\text{He},n)^{28}\text{Si}$.

While this reaction has not been measured at the beam energy of 16 MeV, which would produce a \sim 28-MeV ground-state neutron, it has been measured at lower and higher energies [75, 74] as shown in Figure 5.4. The efficiency measured for the neutrons from this reaction provides a measurement very near the \sim 26-MeV neutrons produced in $^{74,76}\text{Ge}(^3\text{He},n)^{76,78}\text{Se}$ and can be used to verify the absolute efficiency predicted by the Cecil code at neutron energies relevant to $^{74,76}\text{Ge}(^3\text{He},n)^{76,78}\text{Se}$. Figure 5.4 shows the consistency of the measured cross section using that predicted efficiency. While the agreement between measured cross-sections suggests a systematic error due to efficiency of less than 10%, the estimated systematic error of the data from $^{26}\text{Mg}(^3\text{He},n)^{28}\text{Si}$ is \sim 20% [75, 74] and does not provide a better bound than the error associated with the Cecil code.

5.2 Experimental Parameters Related to the Cross Section

The differential cross section is the number of times a reaction occurred ($N_{reaction}$) normalized by the total number of particles incident on the target (N_{beam}), the number density of nuclei in the target (n_{target}), and the efficiency of the detector (ϵ):

$$\frac{d\sigma}{d\Omega} = \frac{N_{reaction}}{N_{beam} \times n_{target} \times \epsilon}. \quad (5.1)$$

The efficiency ϵ of the detector includes the solid angle $d\Omega$. Other quantities in the cross section that relate to the experimental setup are the number of particles incident on the target and the number density of nuclei in the target.

The three targets ($^{74,76}\text{Ge}$ and ^{26}Mg) used in the experiments were provided by John Greene of Argonne National Laboratory (ANL). The $^{74,76}\text{Ge}$ targets were evaporated onto a gold backing, while the ^{26}Mg target is self-supporting. The

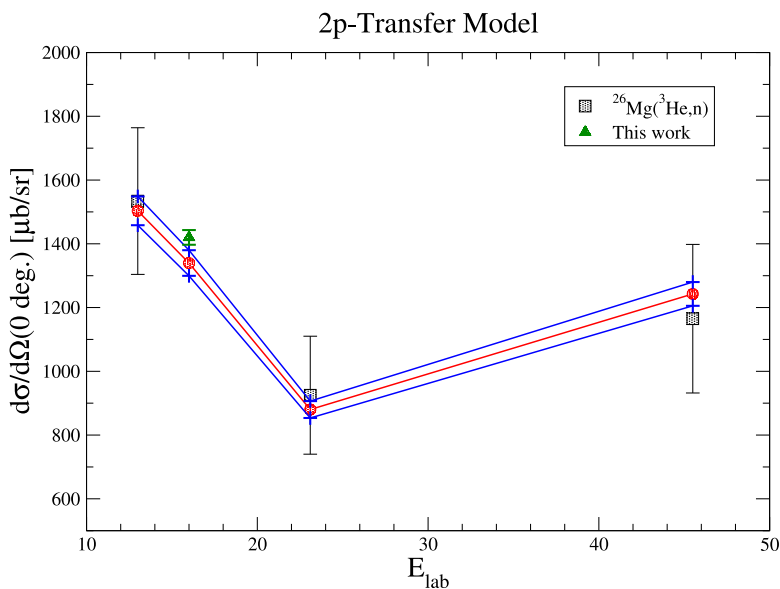


Figure 5.4: Checking consistency of efficiency calculation with $^{26}\text{Mg}(^3\text{He},n)^{28}\text{Si}$. Black squares show previous experimentally-measured values of the cross section. This work (green triangle) is consistent with calculations. The calculations (red circles) are coupled-channel DWBA calculations following the prescription of [75]. The blue lines indicate the estimated systematic error of the calculation.

isotopic abundance and thickness of each target is shown in Table 5.1. The target thicknesses were measured with **an alpha-thickness gauge** when they were made, and again at Hope College using Rutherford back-scattering (RBS). RBS measurements are useful because they give information about the target composition, which must be assumed when calculating target thickness from alpha-thickness-gauge measurements. The reported thicknesses were obtained by analyzing the RBS data with SIMNRA [87], an RBS analysis software. A sample of the fit for each target is shown in Figure 5.5c. Measurements taken at several different positions on each target showed that variations in target thickness were approximately 1%. The predominant features of the RBS spectrum are the plateaus due to the germanium layer and the gold foil. These plateaus overlap, but the features due to beam scattering from the front and back surface of each layer are clearly visible. Figure 5.5a and Figure 5.5b identify these features. This RBS spectrum also shows evidence of small pinholes in the target; they introduce a low-energy aluminum spectrum that is highlighted in red in Figure 5.5a. There are also small areas of the target that are bare gold foil, evidenced by the very small plateau at high energies that is highlighted in green. These features do not alter the estimate of the target thickness, which depends only on the edges of the plateau. Because the edges of the plateau are well defined, the uncertainty in the number of target atoms is less than a percent. A cautious estimate of the uncertainty in the cross section due to the target is 2%. A fit to the data adjusted for the pinholes is shown in Figure 5.5c.

To determine the absolute cross section, it is also necessary to know the total number of ${}^3\text{He}$ ions incident on the target for each dataset. One monitor of the beam current is the charge collected by the Faraday cup. A BaF_2 crystal outside

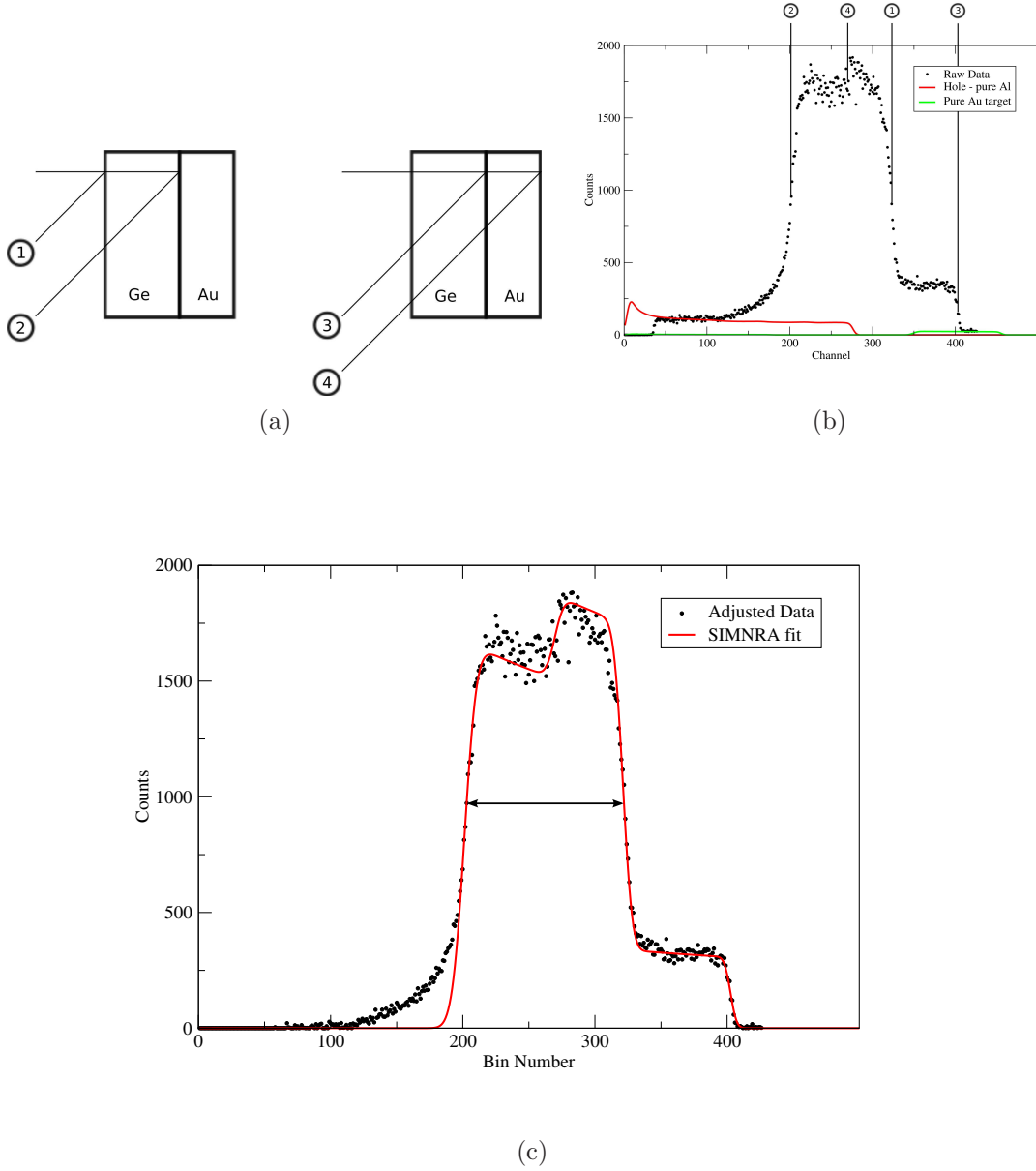


Figure 5.5: (a) Beam scattering from the front and back layer determines the high and low energy plateau edges. The scattering angle is shown as forward to compress the figure but was backward at 168° in the experiment. (b) RBS data for the ^{76}Ge target near the beamspot. The features used to determine the thicknesses of the gold and germanium layers are marked. (c) The RBS spectrum, adjusted by subtracting the background due to pinholes, and its fit. Fitting the RBS spectrum with and without adjusting for pinholes did not result in any significant differences to the predicted target composition or thickness.

		α -gauge ($\mu\text{g}/\text{cm}^2$)	RBS ($\mu\text{g}/\text{cm}^2$)
^{74}Ge (98.9%)	Au_{nat}	1011	Au_{nat} 1001
	^{74}Ge	1057	^{74}Ge 1016
	O_{nat}		9
^{76}Ge (92.82%)	Au_{nat}	1069	Au_{nat} 1014
	^{76}Ge	838	^{74}Ge 775
	O_{nat}		4
^{26}Mg (>99.55%)	^{26}Mg	791	^{26}Mg 685
	C_{nat}		10
	N_{nat}		43
	O_{nat}		52

TABLE 5.1: Target composition and thickness. The isotopic abundance of the target is listed in parenthesis. The α -gauge measurements were performed at ANL and the RBS measurements at Hope College.

the target chamber and a silicon detector inside the target chamber detect γ radiation from beam incident on the target and scattered ^3He beam, respectively. Both these detectors monitor the product of the target thickness and the beam current. Data from the silicon detector show that the ratio of $^{74,76}\text{Ge}$ to gold does not change throughout the run, demonstrating that the targets are stable throughout the run. Additionally, the back-scattered peak in the silicon spectrum scaled with the live charge, which is the charge scalar vetoed by the DAQ busy as discussed in Section 3.3.1. The live charge can therefore be used to scale beam current between runs, making it possible to express $^{74,76}\text{Ge}(^3\text{He},\text{n})^{76,78}\text{Se}$ cross sections in terms of the known $^{26}\text{Mg}(^3\text{He},\text{n})^{28}\text{Si}$ cross section.

5.3 Data Sets

Two sets of $^{74,76}\text{Ge}(^3\text{He},\text{n})^{76,78}\text{Se}$ data are available. The first was taken in September 2011. A subset of this data was taken with no pulse selection due to hardware failure. A second run in January 2012 provided additional data, all

taken with pulse selection. During the January run, data were taken with the $^{74,76}\text{Ge}$ as well as ^{26}Mg targets to provide an accurate normalization. The data sets are summarized in Table 5.2. While the non-pulse-selected data was useful in constraining parts of the pulse-selected background (see Section ??), it was not possible to estimate the background well enough to obtain useful cross-section data from these runs. Thus, the non-pulse-selected data appear in this chapter only as a constraint on a fit to the pulse-selected data.

		Live Time (s)	Live Charge (μC)
January	PS ^{26}Mg	46460	1044
	PS ^{76}Ge	78140	2919
	PS ^{74}Ge	163800	5313
September	PS ^{76}Ge	126200	2873
	PS ^{74}Ge	116700	2619
	NPS ^{76}Ge	273700	15320
	NPS ^{74}Ge	113200	10010

TABLE 5.2: Data sets used in the analysis were obtained in two separate runs. Both pulse-selected (PS) and non-pulse-selected (NPS) data were taken during the September run.

5.4 Cuts

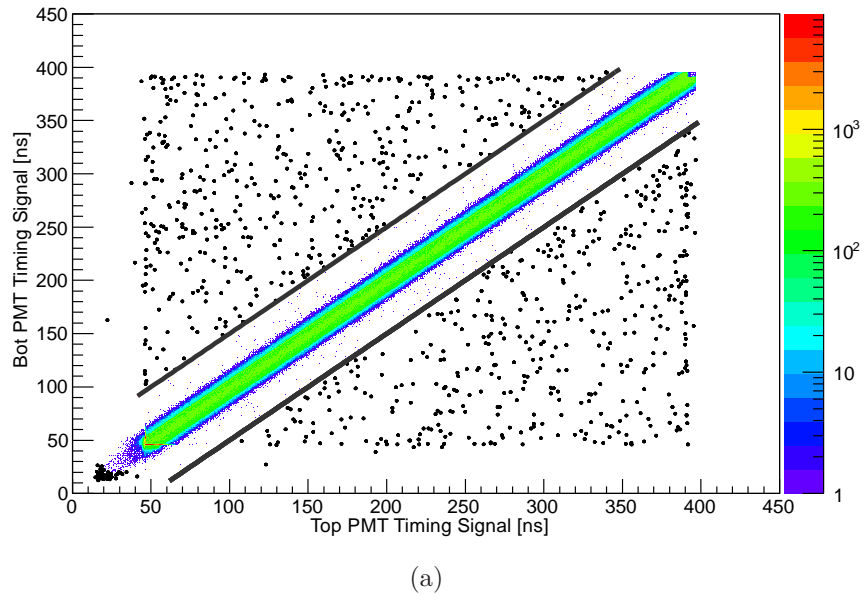
Four sets of cuts were applied to the data to generate a final data set. The first cut verifies that the recorded event represents a real event rather than noise. The next cut discards events with too-low light signals, reducing the background due to γ radiation. Two final cuts reduce the muon background; one cut uses

the veto, and the other eliminates events with light signals too large to be due to neutrons.

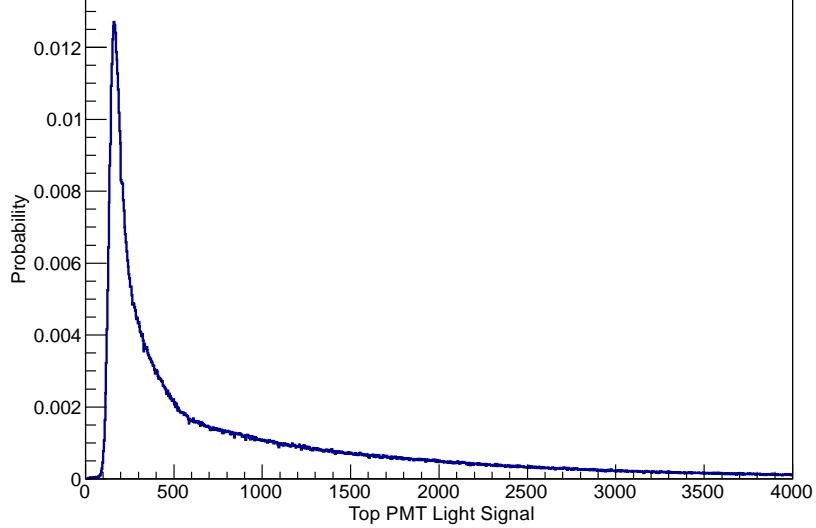
A true event should have energy above the noise level recorded in both top and bottom PMT's. Additionally, the time signals from the top and bottom PMT's should be correlated. A typical scatter plot of timing from the top and bottom PMT are shown in Figure 5.6. Requiring correlated top and bottom timing signals is a cut that is applied to all bars in all final data sets. The other requirement for a valid event is that the light signal be above the noise threshold. An example of a light spectrum for a single bar is shown with the noise threshold already applied Figure 5.6.

Both the veto paddles and the bars of the neutron detector serve as a veto. Veto paddle information is recorded as either “true” or “false” - true if a veto paddle fired during the event, false if it did not. The bars of the neutron detector, in contrast, have more detailed information - time and light output. While accidental coincidences are rare, this additional information is used when a neutron bar is used as veto material. For one bar of the neutron detector to veto another, both must have a valid signal and their average time must be similar.

A first approximation to determining whether or not an event is the result of a muon interaction is to require all but one bar in the neutron detector, as well as the entire veto, to be silent. However, this would veto events that are spatially disconnected and could not possibly be due to a single muon. To eliminate these unnecessary vetoes, we look at events that register signals in detectors with close spatial proximity, a “veto group”. One way to determine the appropriateness of increasing the size of a veto group is by looking at the energy spectrum of vetoed events. Adding detectors to a veto group that primarily eliminates muons results



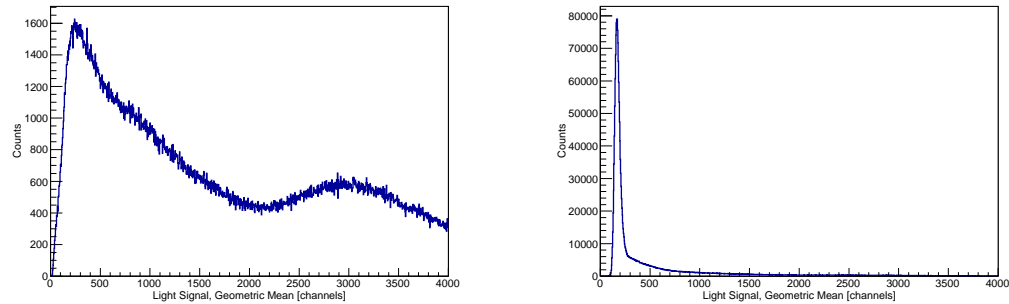
(a)



(b)

Figure 5.6: (a) For a real event, the timing signal from a bar's top and bottom PMT will be similar. Times differing by more than 100 ns are rejected. Events with correlated timing are shown in color and are inside the thick gray lines. The larger, black dots indicate events whose timing is not considered correlated. (b) A low noise threshold placed on the PMT signal discards spurious events.

in an energy spectrum that has roughly equal numbers of high and low energy events, as shown in Figure 5.7a. Material that does not veto primarily muon events will yield an energy spectrum that appears much more like the room background spectrum, heavily weighted towards lower energy events, as in Figure 5.7b. These figures indicate that an appropriate group of material to use in the veto of a detector bar is the immediate, surrounding material. Several samples of veto groups are shown in Figure 5.7c. A separate cut to reject muons discards events that deposit energy above the maximum neutron energy deposition.



(a) Energy spectrum of a neutron detector bar. Entries in this histogram are from events having at least one correlated signal in the neutron detector and are likely to be muons. Notice the high-energy-deposition peak at \sim channel 3000 and its considerable height relative to the low-energy γ background. This low-energy background is dominant in non-muon events as in Figure (b).

(b) Neutron detector bar energy spectrum. These events have no correlation to other signals in the neutron detector and are unlikely to be due to muons. While some high-energy depositions are visible, the spectrum is clearly dominated by the low-energy peak due to γ radiation.



(c) Sample groups of detectors chosen to veto bars in the neutron detector. If the events in a neutron detector bar vetoed by a detector have an energy spectrum dominated by the low-energy γ radiation, that detector is not used as part of the veto for that particular bar.

Figure 5.7

The final cut on the data sets is a lower-energy cut to reduce the random background due to γ radiation. Placing a low-energy cut on the data is difficult because finding an estimator for the energy is not straightforward. It is appealing to argue that light loss due to attenuation must be exponential, and that an accurate estimator of the total deposited energy is the geometric mean of the top and bottom PMT signals:

$$\sqrt{Ae^{-\alpha x} \times Ae^{-\alpha(L-x)}} = \sqrt{A^2 e^{-\alpha L}} = Ae^{-\alpha L/2}, \quad (5.2)$$

where α is a factor determined by the attenuation in the bar and L is its length. If this model of the signal attenuation is correct, the geometric mean should be position-independent. This is not the case, as can be seen in Figure 5.8. Furthermore, the position dependence is not often uniform even between the top and bottom PMT on a single bar, making it difficult to construct an average value. It is necessary to define a low-signal cut that is uniform for all the bars of the detector because the efficiency is sensitive to the low-energy threshold. It is important to set a uniform threshold on the bars of the neutron detector to avoid introducing significant systematic error into the final cross section.

Defining a position-dependent light signal cut on each PMT separately would be an ideal solution to these problems if the position dependence for a given energy were known. While such a characterization of the PMT's for an arbitrary energy is not known, the muon events recorded by the detector do give the light signal as a function of position for one energy. Due to the detector geometry, it is expected that the average path of the muons will be peaked at slightly more than 5 cm. Simulations using the detector bar geometry and an angular distribution of $\cos^{2.4}\theta$ [88] (where θ is the zenith angle) confirm a well-defined peak in the muon path

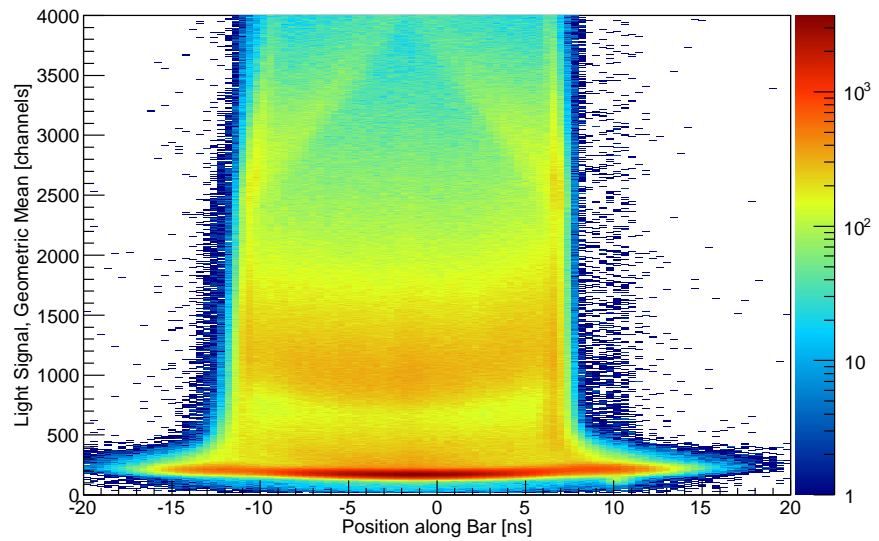


Figure 5.8: Position dependence of the geometric mean of the light signal of rejected events. The band of events with light signals between $\sim 1000\text{-}1500$ channels in particular demonstrates that the signal increases as it approaches the extremes of the neutron detector bar. The events shown here are those that triggered the veto and are likely muons.

length. This most-likely path length manifests as a peak in the energy spectrum that depends only on the thickness of the bars and on the most likely angle of incident muons because they are MIP's. Note that both the bar thickness and the most likely angle of a muon path are the same for every bar in the neutron wall. A simulated energy spectrum is shown next to a real energy spectrum in Figure 5.9. The peak of the light spectrum is assumed to represent the same

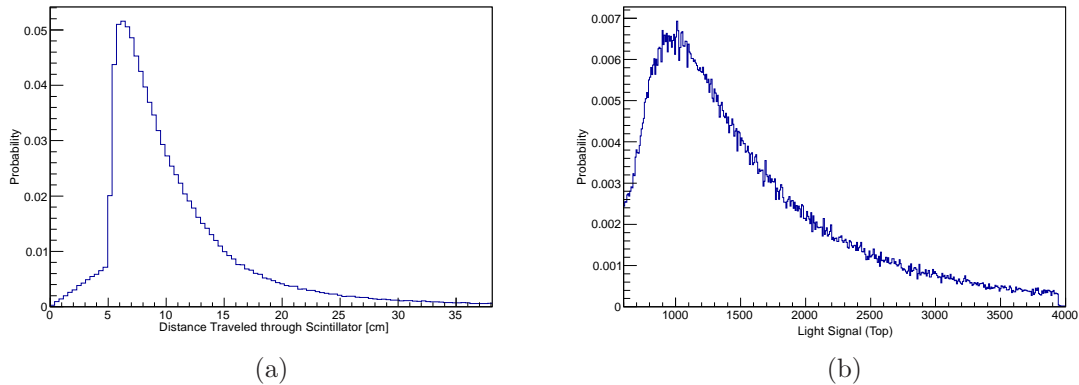
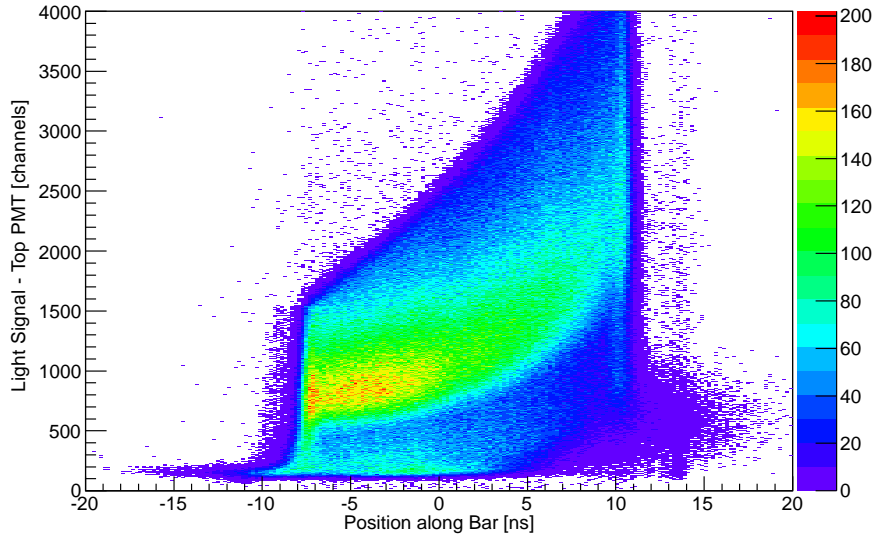
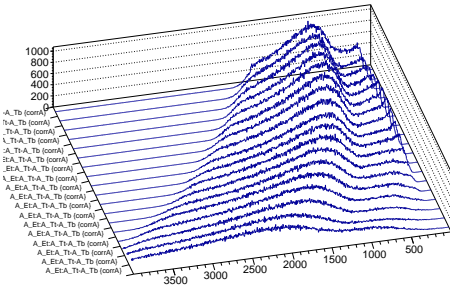


Figure 5.9: (a) A simulation of path length of muons interacting in a detector with dimensions identical to those of the neutron detector bars. Note the distinct peak. (b) Light signal of muon events near the center of the bar. The peak in this distribution is believed to be the peak seen in the simulated spectrum.

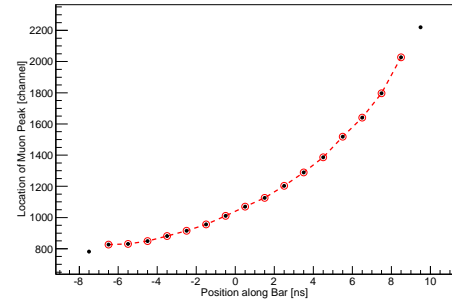
energy and therefore to function as a calibration of the position dependence of the light signal due to the most likely muon energy deposition. Fits to the location of the energy peak as a function of position are shown in Figure 5.10. Using this “constant-energy curve” directly as a lower-energy cut is too high an energy cut as can be seen in Figure 5.11b. Instead, a scaling factor is applied to these curves that maximizes the signal to noise ratio; the scaled curves serve as appropriate



(a) The position dependence of the light signal from a single PMT.



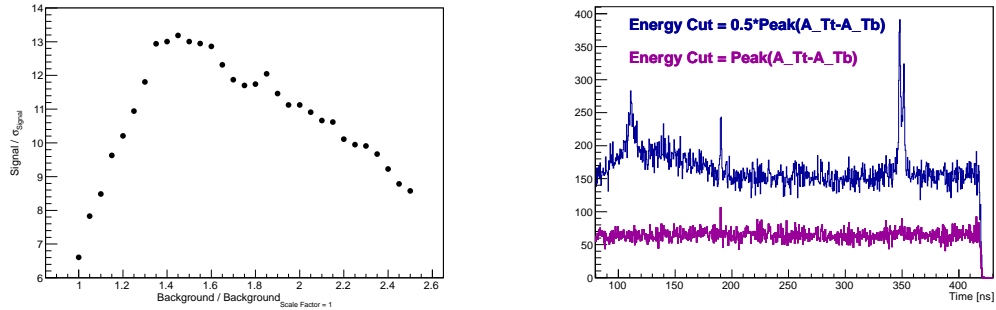
(b) The two-dimensional histogram shown in (a) is projected into a series of one-dimensional histograms. The peaks of these histograms are determined by fitting with a Landau function.



(c) A plot describing the curve which, when scaled, is used as the low-energy cut. The points are determined from the histograms shown in (b). Points at the extremes that do not follow the trend are used to determine the position cut.

Figure 5.10

energy cuts. While high cuts discard more background, they also discard more neutrons of interest, which can deposit a small amount of energy in the detector. The minimum fractional error is achieved with a scaling factor that results in a reduction of the background by a factor of ~ 1.4 (with all other cuts applied). This is the case for every bar in the neutron detector; the fractional error as a function of the energy cut for the forwardmost bar is shown in Figure 5.11a. Scaling ratios are determined by comparing the background to that of the initial cut to obtain uniform scaling from bar to bar. An additional concern is that simply scaling



(a) The ratio of the signal to its statistical error as a function of the energy cut. The energy cut is parametrized as the background reduction to allow uniform scaling between bars.

(b) Without applying a scaling factor to the cut determined as in Figure 5.10, the neutron signals are nearly lost. Scaling the cut by ~ 0.5 results in a reasonable signal to noise ratio.

Figure 5.11

the energy cut may not provide an accurate position dependence. No distinct feature exists at lower energies, making this difficult to check directly. However, the position distribution of rejected events with these scaled energy cuts is flat as seen in Figure 5.12, suggesting that the position dependence at the most-likely

deposited energy for muons is a reasonable approximation for lower-energy events.

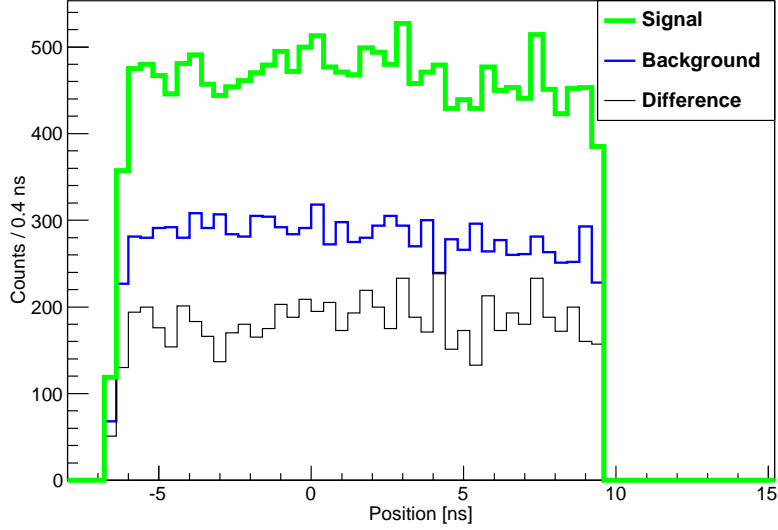


Figure 5.12: A histogram of event position with a lower-energy cut based on position. The data used are the $^{26}\text{Mg}(^{3}\text{He},\text{n})^{28}\text{Si}$ data from January. The difference between the position spectra of the region around the ground state neutron peak (green) and a background region with the same number of bins (blue) is shown in black. That this resulting position spectrum is flat indicates that the position dependence of the cut is appropriate.

The error associated with the lower-energy cut is non-zero due to the uncertainty associated with the fit to the peak. An estimate of the error on the extracted signal is

$$\sigma_S^2 = \left(\frac{dS}{dE} \right)^2 \sigma_E^2, \quad (5.3)$$

where E is a variable denoting the low-energy cut. The uncertainty σ_E is assumed

to be the error on the parameter describing the position of the peak. The change in signal with respect to the energy cut is determined by numerically estimating the derivative in the region of the chosen energy cut. For this energy cut, which is approximately a third of the maximum deposited neutron energy, the error due to the energy cut is <2%.

5.5 Ground State Cross-Section

To extract the counts due to the ground-state neutrons one can sum the counts in the region of the peak and subtract the estimated background:

$$S = P - B, \quad (5.4)$$

where S is the extracted number of signal counts, P is the number of counts in the signal region, and B is the number of estimated background counts. The error associated with S is

$$\sqrt{\sigma_P^2 + \sigma_B^2} \quad (5.5)$$

where both P and B can be understood as a random variable with error \sqrt{P} and \sqrt{B} , respectively.

The primary challenge is finding an accurate way to estimate the background that reduces the error of the extracted counts. As can be seen in Figure 5.13, the background of the pulse-selected data is much simpler than that of the non-pulse-selected data. Without pulse selection, the neutron peak is superimposed on background from previous neutron bunches, making the extracted signal extremely sensitive to poorly-constrained fit parameters. Only signal estimates from the pulse-selected data are used for the data sets discussed in this thesis.

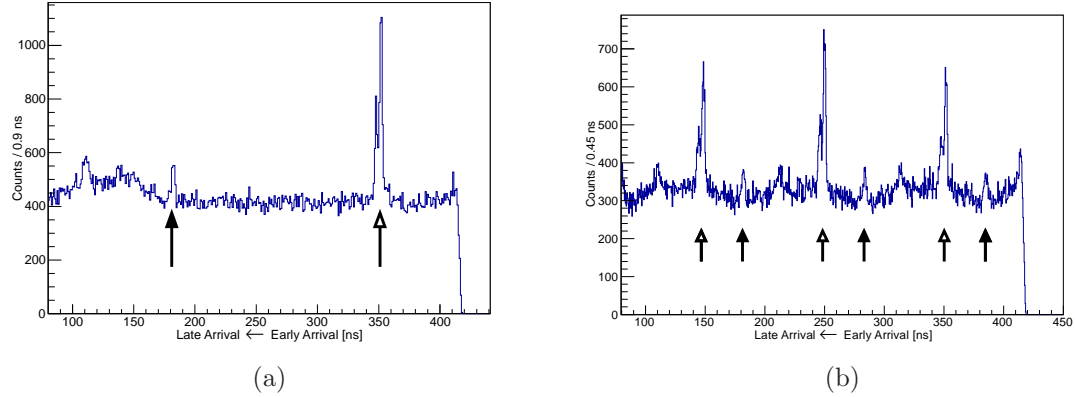


Figure 5.13: (a) The TOF spectrum of the forwardmost neutron detector bar (6.1°) in the case of pulse-selected beam. The data is from the September run. The ground-state neutron peak is indicated with a solid arrow and the γ peak with a hollow arrow. (b) The timing spectrum of the non-pulse-selected beam, also from the September run.

5.5.1 Pulse-Selected Data

In the case of the pulse-selected data, the background in the region of the ground-state peak consists of flat, random background and the high-energy tail of the neutron continuum. The γ -ray peaks are far away from the neutron peak and have no effect. The random background is well-constrained in the region between the ground-state neutron peak and gamma peak. The neutron continuum is due to multiple direct reactions and can only contribute to the background of the ground state neutron peak due to detector resolution. Limits on the contribution of the continuum will be discussed later. For now, we focus on the simplest contribution to the background, the flat distribution due to random radiation.

In the case of the pulse-selected data, estimating the background is done by fitting the flat background. In general, the signal S is calculated by subtracting the estimated background B from the number of counts P in the peak region. If the flat background region is fit to obtain n , the number of counts per bin, the

extracted counts become

$$S = P - B = P - n \times N_b, \quad (5.6)$$

where N_b is the number of bins in the peak region. The error on the extracted counts is then

$$\sqrt{N_{\text{peak}} + \sigma_n^2 \times N_b}. \quad (5.7)$$

The error on the background no longer behaves like that of a random variable because $\sigma_n \sim \sqrt{\frac{n}{N_b}}$. In the $^{74,76}\text{Ge}(^3\text{He},n)^{76,78}\text{Se}$ data sets, the error contribution $\sigma_n^2 \times N_b$ is of order unity and is therefore negligible compared to the statistical error associated with the number of counts in the peak region. Using an estimate of the background based on as many bins as possible, then, results in an error of approximately \sqrt{P} .

Thus far, the sources of uncertainty in the signal counts that have been investigated are the statistical uncertainty, the error associated with the low-energy cut, and the fit uncertainty. The uncertainty introduced by the continuum must also be estimated. A neutron continuum is clearly visible for all reactions. In the ^{28}Si case, the continuum is well-separated from the ground-state neutron peak. The $^{74,76}\text{Ge}(^3\text{He},n)^{76,78}\text{Se}$ data have the potential to be influenced by counts from the continuum because the continuum is much closer to the ground-state neutron peak than for $^{26}\text{Mg}(^3\text{He},n)^{28}\text{Si}$ and also because the integration window must be wide enough to include both the ground and first excited states. To estimate the contribution of the continuum to the peak region, it is fit with a Gamma Distribution, shown in Figure 5.14. This is an appropriate functional model because neutrons populating the continuum cannot have an energy greater than the

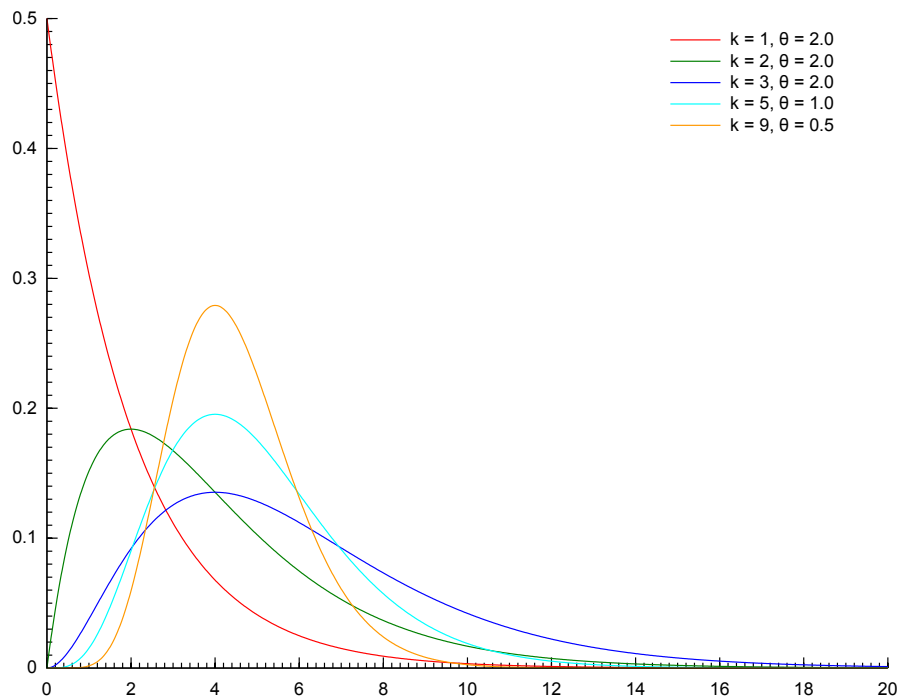


Figure 5.14: The Gamma distribution for various shape parameters [89]. The distribution falls to zero at the origin; it is this property that makes this distribution a candidate model for the neutron continuum.

ground-state neutron, and so its endpoint cannot extend past the center of the ground state neutron distribution; the Gamma Distribution is non-zero only on a semi-infinite range. The pulse-selected data set, however, does not constrain the tails of these functions well because the timing spectrum is not complete. The non-pulse-selected data can help better constrain the fits in this region.

For the same bar, the non-pulse-selected spectrum should have the same features as the pulse-selected spectrum, but shifted and superimposed. Fitting to the pulse-selected and non-pulse-selected histogram simultaneously greatly improves the fit because each bar of the neutron detector should measure the same beam-related spectrum for different runs, making it possible to model the non-pulse-selected spectrum as a shifted, scaled copy of the pulse-selected data. The model used for the pulse-selected data is

$$f_{PS} = B(x; \alpha, \beta) + Gaus_1 + Gaus_2 + Gaus_3 + DoubleGaus + Const_{PS} \quad (5.8)$$

where $B(x; \alpha, \beta)$ is the Beta Distribution; $Gaus_1, Gaus_2, Gaus_3$ are Gaussian distributions describing prominent peaks in the continuum and the ground-state neutron peak; $DoubleGaus$ models the γ peak. These terms are needed to ensure a good overall fit and the contribution of each term is shown in Figure 5.15. The non-pulse-selected data can be modeled by shifting the pulse-selected model by the interval between bunches τ :

$$R \times (f_{PS}(t) + f_{PS}(t + \tau) + f_{PS}(t + 2\tau)) + Const_{NPS}, \quad (5.9)$$

where R is the ratio of total beam on target between the pulse-selected and non-pulse-selected runs. Such a fit converges well and shows that the neutron contin-

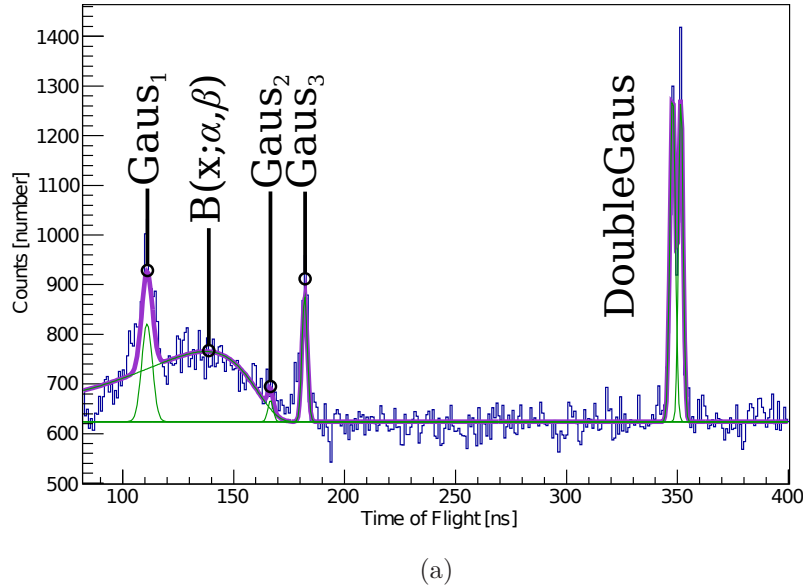
uum contributes less than 1% to the extracted counts in the ground-state neutron peak.

The method used to extract the counts in the ground-state neutron peak is a direct summing of the counts from the peak region followed by subtraction of the estimated flat background from a linear fit. The significant contributions to the estimated error is the statistical error of the sum of the peak region and the error associated with the low-energy cut. Neither the fit to the flat background nor counts from the continuum contributed significant error to the extracted signal. The systematic error contributions consist of the 10% uncertainty in the efficiency and the 2% uncertainty in target thickness. The results are plotted in Figure 5.19. See Appendix A for a table of the values.

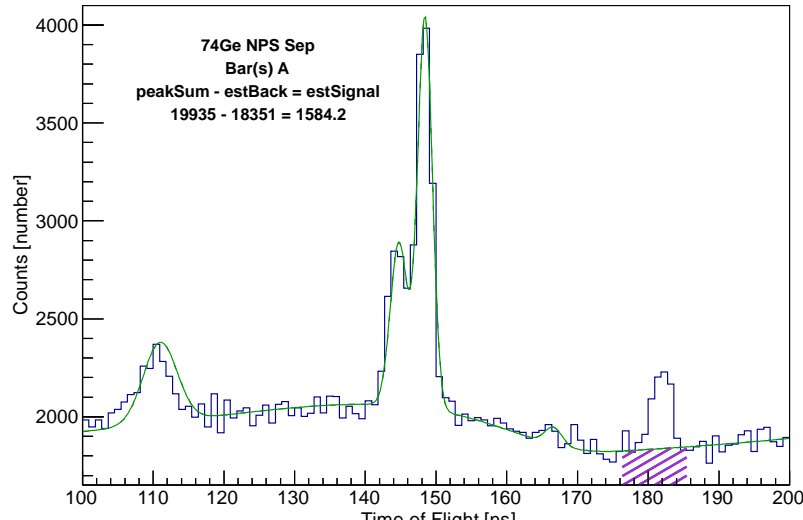
5.6 Placing a Limit on Excited 0^+ States

A primary aim of this experiment is to investigate the distribution of 0^+ strength, making it important to either measure or place a limit on the cross sections of excited 0^+ states. Because the non-pulse-selected data have significant, complicated background, only the pulse-selected data sets were used for this analysis. Because the 0^+ cross section is largest at forward angles, spectra from the three forwardmost detectors was summed to make the TOF spectrum used in this analysis. These three detectors span lab angles 6.1° to 7.7° . The fourth detector, at 8.4° , was not included because the 0^+ cross sections noticeably decline at this angle. Including this detector or any detectors beyond it would have introduced background without contributing significant signal, worsening the sensitivity.

No obvious 0^+ states were observed above the neutron continuum for ${}^{74}\text{Ge}$ or ${}^{76}\text{Ge}$ targets. A limit on the cross section of 0^+ states as a function of energy can



(a)



(b)

Figure 5.15: (a) The fit to the pulse-selected TOF spectrum of the forwardmost neutron detector bar (6.1°). The center and width of each gaussian is constrained for all bars simultaneously while the heights are fit for each bar independently. (b) The timing spectrum of the non-pulse-selected beam is fit together with the pulse-selected spectrum. The region of interest, the ground-state neutron peak, is highlighted but not used in the final data set because of its extreme sensitivity to the fit.

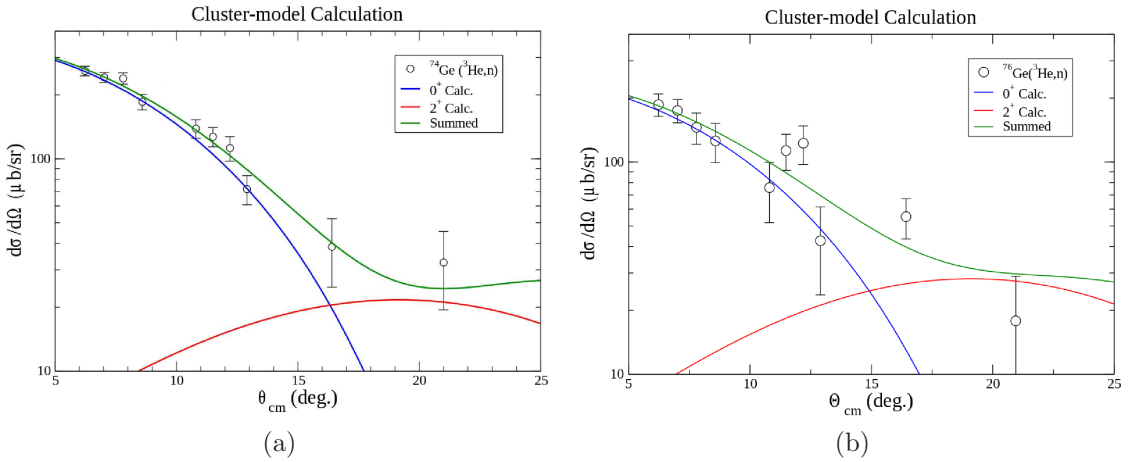


Figure 5.16: (a) The angular distributions of the ground-state first excited state $^{74}\text{Ge}(^3\text{He},n)^{76}\text{Se}$ and (b) $^{76}\text{Ge}(^3\text{He},n)^{78}\text{Se}$. In each graph, the two back-angle measurements are four-bar averages. Because the timing resolution did not allow clear separation of the ground and first excited states, the integration window included both. The DWBA fit to the data is described in Section 5.7.

be determined by solving for the number of counts S necessary to be consistent with zero within i standard deviations σ_S :

$$S = P - B = i\sigma_S, \quad (5.10)$$

where P is the number of counts in the potential signal region and B is an estimate of the counts in that same region. In this case, sideband subtraction is the most appropriate method of determining B because the shape of the continuum is not well-known and attempting to fit it functionally could introduce additional systematic error. The error associated with the signal-induced counts S is then

$$\sigma_S = i\sqrt{P + B} \approx i\sqrt{S + B + B} = i\sqrt{S + 2B}. \quad (5.11)$$

The number of signal counts S can now be written as a function of the background

counts B and the desired level of certainty, i :

$$S = \frac{i^2 \pm \sqrt{i^4 + 8i^2B}}{2}. \quad (5.12)$$

Note that the number of background counts B scales with the chosen integration window. The limits shown were calculated with an integration window of ~ 7 ns, wide enough to include 95% of the peak assuming its resolution is the same as that of the ground-state peak.

The 2σ limit on the cross section for excited 0^+ states in ^{74}Ge and ^{76}Ge is shown in Figure 5.18. The 2σ limit was chosen in order to have 95% confidence in the existence of a peak. A simulation of peaks at the $2\sigma_S$ limit is shown in Figure 5.18. It is important to note that the Q-value dependence of the cross section has a significant impact on the limit. As the excitation energy of the product nucleus increases, the Q-value decreases and the cross section increases. This relationship for $^{74,76}\text{Ge}(^3\text{He},n)^{76,78}\text{Se}$ is calculated with DWBA and is shown in Figure 5.17. The Q-value dependence must be factored out of the count limit obtained directly from the TOF histogram. In general, this is advantageous, as searching for higher excited 0^+ states implies a lower Q value and therefore greater sensitivity. However, at very high excitation energies, the decreasing detector efficiency takes over and the limit begins trending upwards.

5.7 Fitting the 0^+ ground state

The ground-state cross section of $^{74}\text{Ge}(^3\text{He},n)$ is larger than that of $^{76}\text{Ge}(^3\text{He},n)$. One may wonder if this is due to missing 0^+ strength. One way to check whether this could be the case is by calculating the zero-degree cross section with a model that assumes the 0^+ strength to be in the ground state and comparing this to the

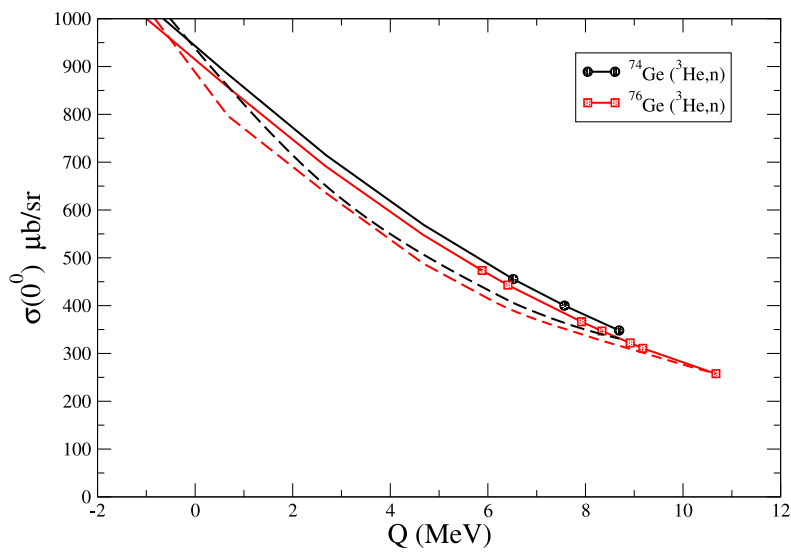
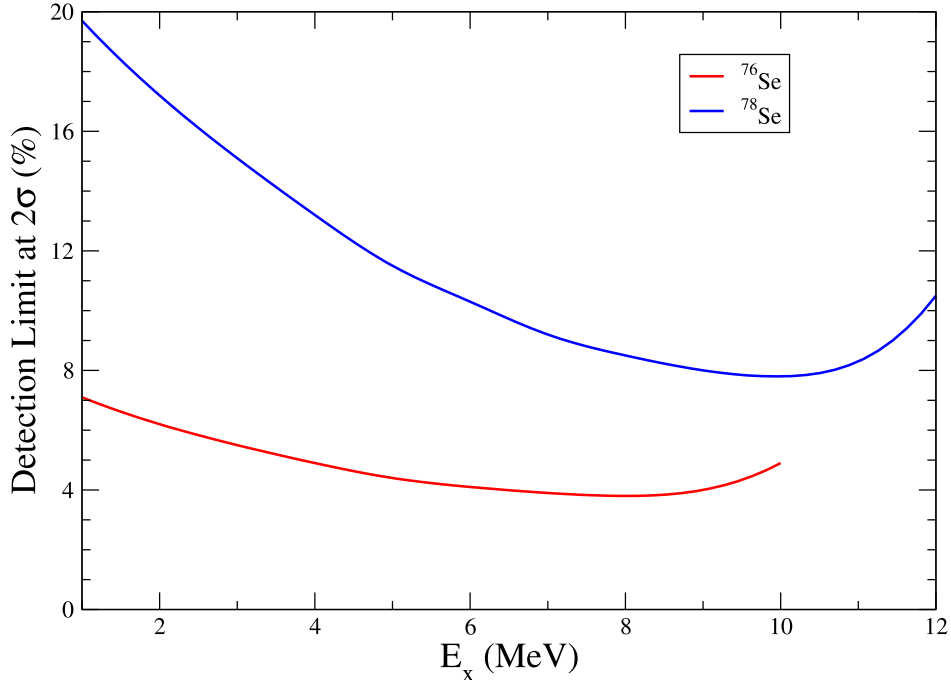
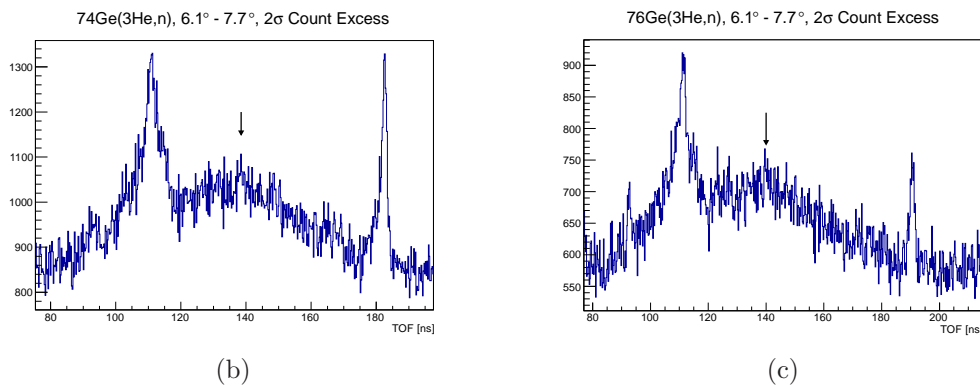


Figure 5.17: The Q -value dependence of the zero-degree cross section of $^{74}\text{Ge}({}^3\text{He},n)$ and $^{76}\text{Ge}({}^3\text{He},n)$. Solid lines indicate the dependence on the Q -value only, while the dashed lines show the dependence moderated by the detector efficiency. Symbols indicate known 0^+ states.



(a)



(b)

(c)

Figure 5.18: (a) Limit on excited 0^+ states as a percentage of the ground-state cross section for ^{74}Ge (lower, in red) and ^{76}Ge (above, in blue). The limit is unreliable for neutrons arriving at times less than 120 ns relative to the γ peak because of the broad neutron peak due to oxygen contamination in the targets as can be seen in (b). The detection limit is therefore cut off at that point. (b) The effect of a signal with 2σ significance is simulated for ^{74}Ge . (c) The effect of a signal with 2σ significance is simulated for ^{76}Ge .

measured values. The zero-degree ground-state cross section can be determined by fitting the experimentally-determined angular distribution of the ground and first excited state together with DWBA and extrapolating the result to zero degrees. The code Fresco [90], used to perform the DWBA calculations, requires the binding potential for the di-proton in the ^3He and ^{74}Ge nuclei as well as the optical-model potentials experienced by the incoming ^3He nucleus and the outgoing neutron. Typical values for the parameters of these potentials are given in Table 5.3, where the optical-model potentials used for the ^3He and neutron are Becchetti-Greenlees [91] and Koning-Delaroche [92], respectively. The results of the fit to the measured angular distributions are shown in Figure 5.19.

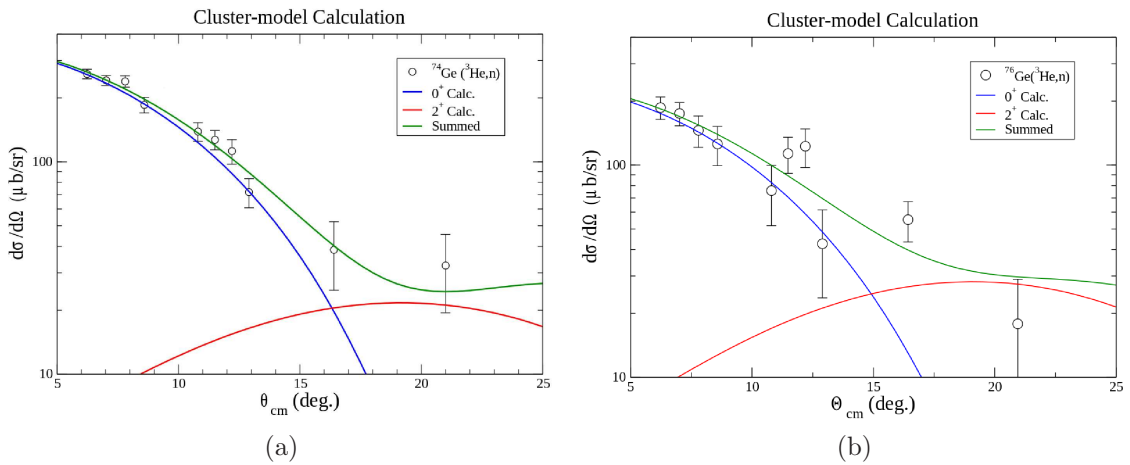


Figure 5.19: (a) The angular distributions of $^{74}\text{Ge}(^3\text{He},n)^{76}\text{Se}$ and (b) $^{76}\text{Ge}(^3\text{He},n)^{78}\text{Se}$. In each graph, the two back-angle measurements are four-bar averages. Because the timing resolution did not allow clear separation of the ground and first excited states, the integration window included both. The sum of the DWBA calculations for the ground and first-excited states has a χ^2 of 0.7 for the ^{74}Ge data and 1.3 for the ^{76}Ge data.

Particle	V_0	r_R	a_R	V_{SO}	r_{SO}	a_{SO}	W	r_W	a_W	W_D	r_{WD}	a_{WD}	W_{SO}	r_{WSO}	a_{WSO}	r_c
^3He (BG)	157.1	1.20	0.72	2.50	1.20	0.72	43.4	1.40	0.88	-	-	-	-	-	-	1.30
^3He (U)	175.4	1.14	0.71	-	-	-	19.9	1.53	0.85	9.13(N-Z)/A	1.53	1.85	-	-	-	1.4
^3He (GDP08)	118.92	4.98	0.82	1.38	3.87	0.13	1.71	5.37	0.84	23.09	5.37	0.84	-	-	-	5.33
n (BG)	45.27	1.21	0.54	5.57	1.03	0.59	1.18	1.21	0.54	6.76	1.34	0.53	-0.07	1.03	0.59	-
n (KD)	45.47	1.21	0.67	5.55	1.03	0.59	1.24	1.21	0.67	6.6	1.28	0.53	-0.076	1.03	0.59	-
^3He bound state	76.6 [†]	1.175	0.65	-	-	-	-	-	-	-	-	-	-	-	-	1.30
Se bound state	100 [†]	1.30	0.65	-	-	-	-	-	-	-	-	-	-	-	-	1.30

TABLE 5.3: Optical and bound-state potentials used in the DWBA analysis, see the text for details of the calculations. Both optical-model potentials vary slowly with N , Z and E ; the values given here are typical. [†] Adjusted to reproduce the experimentally measured binding energy.

The cluster model is sensitive to the parameters used to describe the potentials of the interacting nuclei. The sensitivity of the extracted zero-degree cross section on the bound-state radius parameter, the neutron optical-model potential, and the principal quantum number were all investigated. While changing the bound-state radius strongly affects the normalization, it does not appreciably affect the shape of the angular distribution between 0° and 20° and therefore does not impact the ratio of ground-state to first-excited-state cross section at zero degrees. Using the Becchetti-Greenlees neutron potential rather than the Koning-Delaroche potential does not strongly affect the angular distribution, nor does changing the principal quantum number. The effect of varying these parameters is shown in Figure 5.20. The dependence of the cross section for various ^3He optical-model potentials was also explored and found to result in little difference in the trend in the zero-degree cross sections of ^{74}Ge and ^{76}Ge . See Table 5.3 for the tested parameter ranges and Figure 5.21 for their impact on the relative cross section.

As discussed in Chapter 2, both the cluster and Bayman-Kallio models typically describe the same shape for the $L = 0$ angular distribution, but neither model typically reproduces the absolute cross section. In the case of the $^{58,60,62,64}\text{Ni}$ and ^{88}Sr isotopes, however, the cluster model reproduces the trend as a function of the neutron number rather well. This agreement is shown in Figure 5.22, where all cross sections have been normalized to ^{58}Ni . The cluster model, then, accurately describes the trend when adding protons to f-p-g shell nuclei in this mass region. Cluster model calculations of the $^{74}\text{Ge}(^3\text{He},n)^{76}\text{Se}$ and $^{76}\text{Ge}(^3\text{He},n)^{78}\text{Se}$ reactions show that the smaller cross section of the $^{76}\text{Ge}(^3\text{He},n)^{78}\text{Se}$ reaction is due to the Q-value dependence reproduced by DWBA and not to ground-state loss of 0^+ strength. The cross sections measured for $^{74,76}\text{Ge}(^3\text{He},n)^{76,78}\text{Se}$ are con-

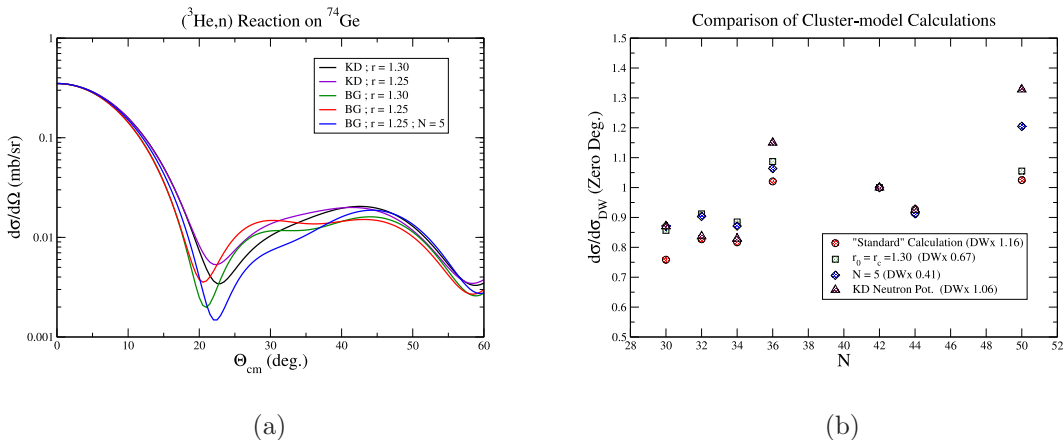


Figure 5.20: (a) Sensitivity of angular distributions on bound-state radius, neutron potential, and principal quantum number. All calculations are normalized to 350 $\mu\text{b}/\text{sr}$ at zero degrees. (b) The effect of varying optical model parameters on the zero-degree cross-section normalization. Sensitivity to the bound-state radius, principle quantum number, and neutron potential were investigated. The “standard” calculation uses Becchetti-Greenlees potentials for the neutron and ^3He , $r_0 = 1.25$ fm and $a = 0.65$ fm, and principle quantum number $N = 4$. The number in parenthesis after each description is the factor needed to normalize the DWBA calculation to the ^{74}Ge cross-section.

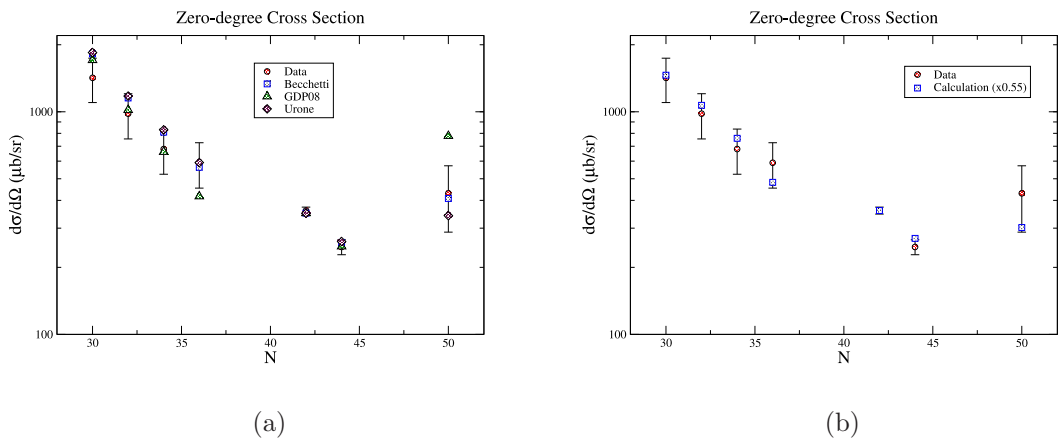


Figure 5.21: (a) **Testing sensitivity to ^3He potentials.** The GDP08 potential differs from the Becchetti and Urone potentials for nickel and strontium isotopes, but all potentials reproduce the measured Q-value dependence of $^{74,76}\text{Ge}$. The calculations are normalized to the ^{74}Ge data. The neutron potential used was the Becchetti-Greenless potential with a bound-state radius of 1.30 fm, a diffuseness of 0.65 fm, and the principle quantum number was 4. (b) The best fit to the data overall. The potential used for ^3He was Becchetti-Greenlees. For the neutron, the KDP potential was used with the parameters as in (a). In both figures, the systematic and statistical errors are shown for all points except ^{74}Ge and ^{76}Ge , where only the statistical errors are shown. Systematic errors were omitted for these nuclei so that the agreement between the trend of the calculation and the data was not obscured.

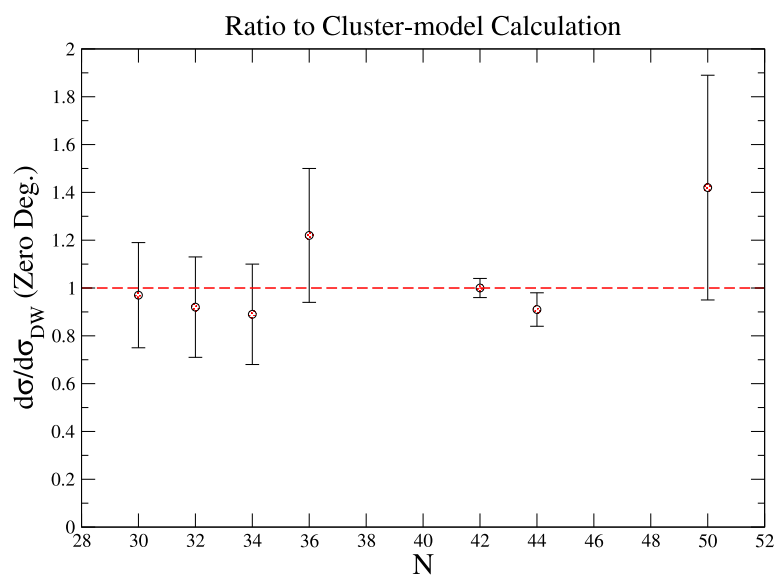


Figure 5.22: The cluster model describes the trend for Ni and Ge isotopes. The cross sections are normalized to ^{74}Ge . Systematic and statistical errors are shown on all data except for ^{74}Ge and ^{76}Ge , where only statistical errors are shown.

sistent with DWBA predictions and the data suggest no significant excited 0^+ states stronger than \sim 4% of the ground-state yield for the critical ^{76}Se nucleus.

CHAPTER 6

CONCLUSION

An observation of $0\nu\beta\beta$ would confirm that neutrinos are Majorana fermions and also allow the calculation of the neutrino mass scale. However, determining the mass scale from the $0\nu\beta\beta$ lifetime requires knowing $M^{0\nu}$, calculations of which can vary by as much as a factor of 5. Single-nucleon transfer experiments can give information on valence shell occupancies and vacancies and have already helped reduce the spread in the $M^{0\nu}$ for ${}^{76}\text{Ge}$. However, the $0\nu\beta\beta$ process would occur primarily on highly-correlated neutron pairs, and single-nucleon transfer is not sensitive to pairing in the nucleus. Two-nucleon transfer experiments can give information on ground-state nucleon pairing, which is particularly important to QRPA, one of the leading methods in $M^{0\nu}$ calculations.

Two-nucleon transfer experiments have been completed or nearly so for several candidate nuclei. The ${}^{130}\text{Te}$ candidate is an interesting case because both two-proton transfer on ${}^{128}\text{Te}$ and two-neutron transfer onto ${}^{130}\text{Te}$ have been studied [62, 61]. While no excited 0^+ states were populated in the neutron-pair transfer, the proton-pair transfer populated an excited 0^+ state with 30% the strength of the ground state. This suggests that the proton-pairing strength is split between the ground state and at least one excited 0^+ state. The work that has been done on ${}^{76}\text{Ge}$ has shown that the neutron-pairing strength is concentrated in the ground state [63], but this offers no constraint on the proton-pairing in ${}^{76}\text{Se}$.

Investigating the proton-pairing in ^{76}Se and, as a check, ^{78}Se is the work of this thesis. The reaction $^{74,76}\text{Ge}(\text{He},\text{n})^{76,78}\text{Se}$ was used to look for excited 0^+ strength. No excited 0^+ states were observed in either nucleus, and limits on such states were determined to be 4-8% of the ground-state cross section for $^{74}\text{Ge}(\text{He},\text{n})^{76}\text{Se}$ and 8-20% of the ground-state cross section for $^{76}\text{Ge}(\text{He},\text{n})^{78}\text{Se}$, depending on excitation energy.

The zero-degree cross sections for both $^{74,76}\text{Ge}$ were determined using a DWBA fit. It was found that the ground-state cross section for ^{74}Ge is (approximately) $360 \pm 30 \mu\text{b}/\text{sr}$ and for ^{76}Ge is (approximately) $252 \pm 25 \mu\text{b}/\text{sr}$, where these errors do not include the 10% systematic error due to uncertainty in the efficiency. While no excited states for ^{76}Ge were observed, the difference in cross section prompted an investigation to determine if the decline was an expected result of kinematics or if excited 0^+ states had been missed in the analysis. All DWBA calculations confirmed that the trend was consistent with the expectations of the reaction model and not due to missing ground-state 0^+ strength.

6.1 Future Work

That no evidence has been found for proton-pair strength in excited 0^+ states of $^{74,76}\text{Ge}$ is encouraging. However, $0\nu\beta\beta$ searches use not just ^{76}Ge as a target, but also ^{48}Ca , ^{82}Se , ^{100}Mo , ^{130}Te , ^{136}Xe , and ^{150}Nd . The Mo and Te isotopes have been studied with both proton-pair and neutron-pair transfer, but proton-pair transfer data is still needed for the candidate Ca, Se, Mo, and Nd isotopes. While the detector used in this experiment may be able to study $^{46}\text{Ca}(\text{He},\text{n})$, isotopes with masses higher than $^{74,76}\text{Ge}$ would be difficult to investigate without increased timing resolution, which is not possible at present. This study does

suggest that DWBA predictions match the measured ground-state cross sections of the $f - p - g$ nuclei. If these cross sections were measured, it may be possible to place a limit on expected excited 0^+ strength based on the deviation from the predicted ground-state cross section.

APPENDIX A

Cross-Section Values

Table of cross-sections for ^{74}Ge and ^{76}Ge .

BIBLIOGRAPHY

- [1] Pauli, W. Pauli letter collection: letter to Lise Meitner (1930). Typed copy.
- [2] Cowan, C. L., Reines, F., Harrison, F. B., Kruse, H. W., and McGuire, A. D. Detection of the free neutrino: a confirmation. *Science* **124**, 103 (1956).
- [3] Davis, R., Harmer, D. S., and Hoffman, K. C. Search for neutrinos from the Sun. *Phys. Rev. Lett.* **20**, 1205 (1968).
- [4] Bahcall, J. N. ^{7}Be solar neutrino line: A reflection of the central temperature distribution of the Sun. *Phys. Rev. D* **49**, 3923 (1994).
- [5] Cleveland, B. T., Daily, T., Raymond Davis, J., Distel, J. R., Lande, K., Lee, C. K., Wildenhain, P. S., and Ullman, J. Measurement of the solar electron neutrino flux with the Homestake chlorine detector. *The Astrophysical Journal* **496**, 505 (1998).
- [6] Danby, G., Gaillard, J.-M., Goulian, K., Lederman, L. M., Mistry, N., Schwartz, M., and Steinberger, J. Observation of high-energy neutrino reactions and the existence of two kinds of neutrinos. *Phys. Rev. Lett.* **9**, 36 (1962).
- [7] Perl, M. L., Abrams, G. S., Boyarski, A. M., Breidenbach, M., Briggs, D. D., Bulos, F., Chinowsky, W., Dakin, J. T., Feldman, G. J., Friedberg, C. E. *et al.* Evidence for anomalous lepton production in $e^+ - e^-$ annihilation. *Phys. Rev. Lett.* **35**, 1489 (1975).
- [8] Kodama, K., Ushida, N., Andreopoulos, C., Saoulidou, N., Tzanakos, G., Yager, P., Baller, B., Boehnlein, D., Freeman, W., Lundberg, B. *et al.* Observation of tau neutrino interactions. *Physics Letters B* **504**, 218 (2001).
- [9] Beringer, J., Arguin, J. F., Barnett, R. M., Copic, K., Dahl, O., Groom, D. E., Lin, C. J., Lys, J., Murayama, H., Wohl, C. G. *et al.* Review of particle physics. *Phys. Rev. D* **86**, 010001 (2012).

- [10] Aharmim, B., Ahmed, S. N., Amsbaugh, J. F., Anaya, J. M., Anthony, A. E., Banar, J., Barros, N., Beier, E. W., Bellerive, A., Beltran, B. *et al.* Measurement of the ν_e and total ^8B solar neutrino fluxes with the Sudbury Neutrino Observatory phase-III data set. *Phys. Rev. C* **87**, 015502 (2013).
- [11] Fukuda, Y., Hayakawa, T., Ichihara, E., Inoue, K., Ishihara, K., Ishino, H., Itow, Y., Kajita, T., Kameda, J., Kasuga, S. *et al.* Measurements of the solar neutrino flux from Super-Kamiokande's first 300 days. *Phys. Rev. Lett.* **81**, 1158 (1998).
- [12] Pontecorvo, B. Neutrino experiments and the problem of conservation of leptonic charge. *Soviet Journal of Experimental and Theoretical Physics* **26**, 984 (1968).
- [13] Cohen, A. G., Glashow, S. L., and Ligeti, Z. Disentangling neutrino oscillations. *Physics Letters B* **678**, 191 (2009).
- [14] Abazajian, K., Calabrese, E., Cooray, A., Bernardis, F. D., Dodelson, S., Friedland, A., Fuller, G., Hannestad, S., Keating, B., Linder, E. *et al.* Cosmological and astrophysical neutrino mass measurements. *Astroparticle Physics* **35**, 177 (2011).
- [15] Lobashev, V. The search for the neutrino mass by direct method in the tritium beta-decay and perspectives of study it in the project KATRIN. *Nuclear Physics A* **719**, C153 (2003).
- [16] Mueller, T. A., Lhuillier, D., Fallot, M., Letourneau, A., Cormon, S., Fechner, M., Giot, L., Lasserre, T., Martino, J., Mention, G. *et al.* Improved predictions of reactor antineutrino spectra. *Phys. Rev. C* **83**, 054615 (2011).
- [17] Murayama, H. The origin of neutrino mass. *Physics World* (2002).
- [18] Fukugita, M. and Yanagida, T. Baryogenesis without grand unification. *Physics Letters B* **174**, 45 (1986).
- [19] Avignone, F. T., Elliott, S. R., and Engel, J. Double beta decay, Majorana neutrinos, and neutrino mass. *Rev. Mod. Phys.* **80**, 481 (2008).
- [20] Aalseth, C. E., Avignone, F. T., Brodzinski, R. L., Cebrian, S., Garcia, E., Gonzalez, D., Hensley, W. K., Irastorza, I. G., Kirpichnikov, I. V., Klimenko, A. A. *et al.* IGEX ^{76}Ge neutrinoless double-beta decay experiment: Prospects for next generation experiments. *Phys. Rev. D* **65**, 092007 (2002).
- [21] Suhonen, J. and Civitarese, O. Weak-interaction and nuclear-structure aspects of nuclear double beta decay. *Physics Reports* **300**, 123 (1998).

- [22] Menendez, J., Poves, A., Caurier, E., and Nowacki, F. Disassembling the nuclear matrix elements of the neutrinoless $\beta\beta$ decay. *Nuclear Physics A* **818**, 139 (2009).
- [23] Faessler, A., Rodin, V., and Simkovic, F. Nuclear matrix elements for neutrinoless double-beta decay and double-electron capture. *J. Phys. G* **39**, 124006 (2012).
- [24] Suhonen, J. and Civitarese, O. Effects of orbital occupancies and spin-orbit partners on decay rates. *Nuclear Physics A* **847**, 207 (2010).
- [25] Rodríguez, T. R. and Martínez-Pinedo, G. Energy density functional study of nuclear matrix elements for neutrinoless $\beta\beta$ decay. *Phys. Rev. Lett.* **105**, 252503 (2010).
- [26] Iachello, F., Barea, J., and Kotila, J. Advances in the theory of $0\nu\beta\beta$ decay. In O. Civitarese, I. Stekl, and J. Suhonen, editors, *American Institute of Physics Conference Series*, volume 1417 of *American Institute of Physics Conference Series*, pages 62–68 (2011).
- [27] Rath, P. K., Chandra, R., Chaturvedi, K., Raina, P. K., and Hirsch, J. G. Uncertainties in nuclear transition matrix elements for neutrinoless $\beta\beta$ decay within the projected-Hartree-Fock-Bogoliubov model. *Phys. Rev. C* **82**, 064310 (2010).
- [28] Schwingenheuer, B. Status and prospects of searches for neutrinoless double beta decay. *Annalen der Physik* (2013).
- [29] Klapdor-Kleingrothaus, H., Krivosheina, I., Dietz, A., and Chkvorets, O. Search for neutrinoless double beta decay with enriched ^{76}Ge in Gran Sasso 1990-2003. *Physics Letters B* **586**, 198 (2004).
- [30] Auger, M., Auty, D. J., Barbeau, P. S., Beauchamp, E., Belov, V., Benitez-Medina, C., Breidenbach, M., Brunner, T., Burenkov, A., Cleveland, B. *et al.* Search for neutrinoless double-beta decay in ^{136}Xe with EXO-200. *Phys. Rev. Lett.* **109**, 032505 (2012).
- [31] Andreotti, E., Arnaboldi, C., III, F. A., Balata, M., Bandac, I., Barucci, M., Beeman, J., Bellini, F., Brofferio, C., Bryant, A. *et al.* ^{130}Te neutrinoless double-beta decay with CUORICINO. *Astroparticle Physics* **34**, 822 (2011).
- [32] Simard, L. and the Nemo-3 collaboration. The NEMO-3 results after completion of data taking. *Journal of Physics: Conference Series* **375**, 042011 (2012).

- [33] Gando, A., Gando, Y., Hanakago, H., Ikeda, H., Inoue, K., Kato, R., Koga, M., Matsuda, S., Mitsui, T., Nakada, T. *et al.* Measurement of the double- β decay half-life of ^{136}Xe with the KamLAND-Zen experiment. *Phys. Rev. C* **85**, 045504 (2012).
- [34] Grabmeyer, P. and the GERDA collaboration. Results from GERDA (2012). The XXV International Conference on Neutrino Physics and Astrophysics.
- [35] Ogawa, I., Kishimoto, T., Umehara, S., Ito, G., Yasuda, K., Kakubata, H., Miyashita, M., Takubo, K., Matsuoka, K., Nomachi, M. *et al.* Study of ^{48}Ca double beta decay by CANDLES. *Journal of Physics: Conference Series* **375**, 042018 (2012).
- [36] lvarez, V., Borges, F. I. G. M., Crcel, S., Carmona, J. M., Castel, J., Catal, J. M., Cebrin, S., Cervera, A., Chan, D., Conde, C. A. N. *et al.* NEXT-100 Technical Design Report (TDR). Executive summary. *Journal of Instrumentation* **7**, T06001 (2012).
- [37] Gorla, P. and the Cuore collaboration. The CUORE experiment: status and prospects. *Journal of Physics: Conference Series* **375**, 042013 (2012).
- [38] Wilkerson, J. F., Aguayo, E., Iii, F. T. A., Back, H. O., Barabash, A. S., Beene, J. R., Bergevin, M., Bertrand, F. E., Boswell, M., Brudanin, V. *et al.* The Majorana demonstrator: A search for neutrinoless double-beta decay of germanium-76. *Journal of Physics: Conference Series* **375**, 042010 (2012).
- [39] Barabash, A. and the SuperNemo Collaboration. SuperNEMO double beta decay experiment. *Journal of Physics: Conference Series* **375**, 042012 (2012).
- [40] Hartnell, J. and the Sno+ collaboration. Neutrinoless double beta decay with SNO+. *Journal of Physics: Conference Series* **375**, 042015 (2012).
- [41] Vogel, P. Nuclear structure and double beta decay. *Journal of Physics G: Nuclear and Particle Physics* **39**, 124002 (2012).
- [42] Borcea, C., Audi, G., Wapstra, A., and Favaron, P. The 1993 atomic mass evaluation: (III) Separation and decay energies. Graphs of systematic trends. *Nuclear Physics A* **565**, 158 (1993).
- [43] Casten, R. *Nuclear Structure from a Simple Perspective* (Oxford University Press, 1990).
- [44] Mayer, M. G. Nuclear configurations in the spin-orbit coupling model. I. empirical evidence. *Phys. Rev.* **78**, 16 (1950).

- [45] Woods, R. D. and Saxon, D. S. Diffuse surface optical model for nucleon-nuclei scattering. *Phys. Rev.* **95**, 577 (1954).
- [46] Liang, H., Shen, S., Zhao, P., and Meng, J. Pseudospin symmetry in supersymmetric quantum mechanics: Schrödinger equations. *Phys. Rev. C* **87**, 014334 (2013).
- [47] Šimkovic, F., Faessler, A., Rodin, V., Vogel, P., and Engel, J. Anatomy of the $0\nu\beta\beta$ nuclear matrix elements. *Phys. Rev. C* **77**, 045503 (2008).
- [48] Caurier, E., Menendez, J., Nowacki, F., and Poves, A. Influence of pairing on the nuclear matrix elements of the neutrinoless $\beta\beta$ decays. *Phys. Rev. Lett.* **100**, 052503 (2008).
- [49] Bender, M., Heenen, P. H., and Reinhard, P. G. Self-consistent mean-field models for nuclear structure. *Rev. Mod. Phys.* **75**, 121 (2003).
- [50] Bardeen, J., Cooper, L. N., and Schrieffer, J. R. Microscopic theory of superconductivity. *Phys. Rev.* **106**, 162 (1957).
- [51] Bohr, A., Mottelson, B. R., and Pines, D. Possible analogy between the excitation spectra of nuclei and those of the superconducting metallic state. *Phys. Rev.* **110**, 936 (1958).
- [52] Yong, Z., Zhong-Yu, M., Bao-Qiu, C., and Jun-Qing, L. Ground-state properties of $Z = 59$ nuclei in the relativistic mean-field theory. *Chinese Physics Letters* **17**, 185 (2000).
- [53] Nambu, Y. and Mukerjee, M. BCS mechanism and the interacting boson model. *Physics Letters B* **209**, 1 (1988).
- [54] Yoshida, S. Note on the two-nucleon stripping reaction. *Nuclear Physics* **33**, 685 (1962).
- [55] Macfarlane, M. H. and French, J. B. Stripping reactions and the structure of light and intermediate nuclei. *Rev. Mod. Phys.* **32**, 567 (1960).
- [56] Schiffer, J. P., Hoffman, C. R., Kay, B. P., Clark, J. A., Deibel, C. M., Freeman, S. J., Howard, A. M., Mitchell, A. J., Parker, P. D., Sharp, D. K. *et al.* Test of sum rules in nucleon transfer reactions. *Phys. Rev. Lett.* **108**, 022501 (2012).
- [57] Freeman, S. J. and Schiffer, J. P. Constraining the $0\nu2\beta$ matrix elements by nuclear structure observables. *Journal of Physics G: Nuclear and Particle Physics* **39**, 124004 (2012).

- [58] Schiffer, J. P., Freeman, S. J., Clark, J. A., Deibel, C., Fitzpatrick, C. R., Gros, S., Heinz, A., Hirata, D., Jiang, C. L., Kay, B. P. *et al.* Nuclear structure relevant to neutrinoless double β decay: ^{76}Ge and ^{76}Se . *Phys. Rev. Lett.* **100**, 112501 (2008).
- [59] Kay, B. P., Schiffer, J. P., Freeman, S. J., Adachi, T., Clark, J. A., Deibel, C. M., Fujita, H., Fujita, Y., Grabmayr, P., Hatanaka, K. *et al.* Nuclear structure relevant to neutrinoless double β decay: The valence protons in ^{76}Ge and ^{76}Se . *Phys. Rev. C* **79**, 021301 (2009).
- [60] Suhonen, J. and Civitarese, O. Effects of orbital occupancies on the neutrinoless $\beta\beta$ matrix element of ^{76}Ge . *Physics Letters B* **668**, 277 (2008).
- [61] Bloxham, T., Kay, B. P., Schiffer, J. P., Clark, J. A., Deibel, C. M., Freeman, S. J., Freedman, S. J., Howard, A. M., McAllister, S. A., Parker, P. D. *et al.* Pair correlations in the neutrinoless double- β decay candidate ^{130}Te . *Phys. Rev. C* **82**, 027308 (2010).
- [62] Alford, W., Anderson, R., Batay-Csorba, P., Emigh, R., Lind, D., Smith, P., and Zafiratos, C. The ($^3\text{He},\text{n}$) reaction on tellurium isotopes. *Nuclear Physics A* **323**, 339 (1979).
- [63] Freeman, S. J., Schiffer, J. P., Villari, A. C. C., Clark, J. A., Deibel, C., Gros, S., Heinz, A., Hirata, D., Jiang, C. L., Kay, B. P. *et al.* Pair correlations in nuclei involved in neutrinoless double β decay: ^{76}Ge and ^{76}Se . *Phys. Rev. C* **75**, 051301 (2007).
- [64] Perey, C. and Perey, F. Compilation of phenomenological optical-model parameters 1969-1972. *Atomic Data and Nuclear Data Tables* **13**, 293 (1974).
- [65] Becchetti, F. D. and Greenlees, G. W. Nucleon-nucleus optical-model parameters, $A > 40$, $E < 50$ MeV. *Phys. Rev.* **182**, 1190 (1969).
- [66] Bayman, B. F. and Kallio, A. Relative-angular-momentum-zero part of two-nucleon wave functions. *Phys. Rev.* **156**, 1121 (1967).
- [67] Schiffer, J. P. Private Communication.
- [68] Singh, B. Nuclear Data Sheets page 63 (1995).
- [69] Reiser, M. *Theory and design of charged particle beam* (Weinheim, DE, 2008), 2nd edition.
- [70] Becchetti, F., Lee, M., O'Donnell, T., Roberts, D., Kolata, J., Lamm, L., Rogachev, G., Guimares, V., DeYoung, P., and Vincent, S. The TwinSol low-energy radioactive nuclear beam apparatus: status and recent results.

Nuclear Instruments and Methods in Physics Research Section A: Accelerators, Spectrometers, Detectors and Associated Equipment **505**, 377 (2003). Proceedings of the tenth Symposium on Radiation Measurements and Applications.

- [71] Lynch, F., Lewis, R., Bollinger, L., Henning, W., and Despe, O. Beam buncher for heavy ions. Nuclear Instruments and Methods **159**, 245 (1979).
- [72] Kolata, J., Amro, H., Cloughesy, M., DeYoung, P., Rieth, J., Bychowski, J., and Peaslee, G. A large segmented neutron detector for reaction studies with radioactive beams near the coulomb barrier. Nuclear Instruments and Methods in Physics Research Section A: Accelerators, Spectrometers, Detectors and Associated Equipment **557**, 594 (2006).
- [73] Premium plastic scintillators. Technical report, Saint-Gobain Crystals, Hiram, OH, USA (2005). http://www.detectors.saint-gobain.com/uploadedFiles/SGdetectors/Documents/Product_Data_Sheets/BC400-404-408-412-416-Data-Sheet.pdf.
- [74] Bohne, W., Bachs, K., Fuchs, H., Grabisch, K., Hilscher, D., Jahnke, U., Kluge, H., Masterson, T., Morgenstern, H., and Wildenthal, B. Study of the reactions $^{24,26}\text{Mg}(\text{He},\text{n})^{26,28}\text{Si}$ and $^{28}\text{Si}(\text{He},\text{n})^{30}\text{S}$. Nuclear Physics A **378**, 525 (1982).
- [75] Abe, K., Maeda, K., Ishimatsu, T., Kawamura, T., Furukawa, K., Orihara, H., and Zafiratos, C. D. The $^{26}\text{Mg}(\text{He},\text{n})^{28}\text{Si}$ reaction at 23.1 and 45.5 MeV. Journal of the Physical Society of Japan **54**, 3660 (1985).
- [76] Scintillating optical fibers. Technical report, Saint-Gobain Crystals, Hiram, OH, USA. <http://www.detectors.saint-gobain.com/fibers.aspx>.
- [77] Kuraray clear fibers. Technical report, kuraray. <http://kuraraypsf.jp/psf/cf.html>.
- [78] Knoll, G. F. *Radiation Detection and Measurement* (Wiley, 2010), 4th edition.
- [79] Aguillion, G., Anderson, B., Attree, D., Ball, A., Bard, R., Bentvelsen, S., Betts, S., Boutemeur, M., Caron, B., Charalambous, A. *et al.* Thin scintillating tiles with high light yield for the OPAL endcaps. Nuclear Instruments and Methods in Physics Research Section A: Accelerators, Spectrometers, Detectors and Associated Equipment **417**, 266 (1998).
- [80] de Barbaro, P., Bodek, A., Budd, R., Fan, Q., Sakumoto, W., Winer, B., Proudfoot, J., Underwood, D., Foster, G., Freeman, J. *et al.* R&D results

on scintillating tile/fiber calorimetry for the CDF and SDC detectors. Nuclear Instruments and Methods in Physics Research Section A: Accelerators, Spectrometers, Detectors and Associated Equipment **315**, 317 (1992).

- [81] Moiseev, A., Hartman, R., Ormes, J., Thompson, D., Amato, M., Johnson, T., Segal, K., and Sheppard, D. The anti-coincidence detector for the GLAST large area telescope. Astroparticle Physics **27**, 339 (2007).
- [82] Ayotte, G., Archambault, L., Gingras, L., Lacroix, F., Beddar, A. S., and Beaulieu, L. Surface preparation and coupling in plastic scintillator dosimetry. Medical Physics **33**, 3519 (2006).
- [83] Saraiva, J., Wemans, A., Maneira, M., Maio, A., and Patriarca, J. The aluminization of 600 k WLS fibers for the TileCal/ATLAS/LHC. In *Nuclear Science Symposium Conference Record, 2003 IEEE*, volume 5, pages 3468 – 3472 (2003).
- [84] Dong, Y., Li, Y., Wu, B., Zhang, Y., and Zhang, S. Light collection of the polar detector. SCIENCE CHINA Physics, Mechanics & Astronomy **53**, 43 (2010).
- [85] Cecil, R., Anderson, B., and Madey, R. Improved predictions of neutron detection efficiency for hydrocarbon scintillators from 1 MeV to about 300 MeV. Nuclear Instruments and Methods **161**, 439 (1979).
- [86] Agency, I. A. E. *Handbook on Nuclear Activation Data* (1987). Technical Reports Series 273.
- [87] SIMNRA user's guide. Max-Planck-Institut fur Plasmaphysik, Garching, Germany (1997). Report IPP 9/113.
- [88] Pal, S., Majumder, G., Mondal, N., Samuel, D., and Satyanarayana, B. Angular distribution of cosmic muons using INO-ICAL prototype detector at TIFR. Pramana **79**, 1267 (2012).
- [89] wikipedia. Gamma distribution. http://en.wikipedia.org/wiki/Gamma_distribution (2013).
- [90] Thompson, I. J. Coupled reaction channels calculations in nuclear physics. Computer Physics Reports **7**, 167 (1988).
- [91] Becchetti, F., Makofske, W., and Greenlees, G. A study of the $^{46,48}\text{Ti}(3\text{He},t)$ and $^{58,60}\text{Ni}(3\text{He},t)$ reactions to isobaric analogue states. Nuclear Physics A **190**, 437 (1972).

- [92] Koning, A. and Delaroche, J. Local and global nucleon optical models from 1 keV to 200 MeV. Nuclear Physics A **713**, 231 (2003).

This document was prepared & typeset with L^AT_EX 2_≤, and formatted with NDDiss2_≤ classfile (v3.0[2005/07/27]) provided by Sameer Vijay.